Characterization of Dosimeters for Small Field Applications Including Comparisons to Monte Carlo and Treatment Planning System Computed Doses

by

Elena Timakova
B.Sc., McMaster University, 2020
A Thesis Submitted in Partial Fulfillment of the
Requirements for the Degree of

MASTER OF SCIENCE

in the Department of Physics and Astronomy

Characterization of Dosimeters for Small Field Applications Including Comparisons to Monte Carlo and Treatment Planning System Computed Doses

by

Elena Timakova
B.Sc., McMaster University, 2020

Supervisory Committee

Dr. Sergei Zavgorodni, Co-Supervisor
(Department of Physics and Astronomy)

Dr. Magdalena Bazalova-Carter, Co-Supervisor
(Department of Physics and Astronomy)

Dr. Wayne Beckham, Departmental Member
(Department of Physics and Astronomy)

ABSTRACT

In radiation therapy, accurately determining the dose to a patient is extremely important for optimal patient outcomes and efficient clinical flow. Under small field conditions, experimental dosimetry is difficult due to fluence perturbation effects and computational dosimetry poses challenges related to limits on computation time. In this work, two novel dosimeters were characterized for important properties of a small field dosimeter. Then, the dosimeters' performance was compared to treatment planning system dose algorithms and Monte Carlo methods. The new dosimeters showed promising results with relatively little effort put towards set-up and measurement acquisition for normal clinical conditions. Good agreement was seen for isocentric clinical SRT plan delivery with targets around 2 cm in diameter and modulation scores of around 5 MU/cGy. As field sizes fall below 1 x 1 cm^2, fields move off axis, and/or plans increase in modulation score beyond 5 MU/cGy, disagreements begin to emerge.

Contents

List of Tables

List of Figures

ACKNOWLEDGEMENTS

The author would like to acknowledge Alex Hart, Benjamin Côté, and François Therriault-Proulx for providing training pertaining to the use of HYPERSCINT RP-200. The author also acknowledges Dr. Magdalena Bazalova-Carter and the Excite lab for lending the HYPERSCINT RP-200 for study. Author is grateful for the insightful comments, discussion, and suggestions by Dr. Eyad Alhakeem and Dr. Sergei Zavgorodni. I acknowledge Dr. Wolfgang Lechner for providing their measurement data. The author would also like to thank the Canada Research Chairs program for NSERC Discovery Grant for funding the acquisition of HYPERSCINT RP-200 system.

Chapter 1

Introduction

Cancer is a disease that affects a large proportion of the Canadian population. In fact, 2 in 5 Canadians will be diagnosed with cancer at some point throughout their lives and 25% of those people will die because of it [93]. Luckily, there are several treatment options. About half of all cancer patients receive some form of radiation therapy as part of their treatment. Radiation therapy involves damaging the DNA of cancerous cells through the use of highly ionizing particles. Although radiation treatment is designed to preferentially affects cancerous cells, it does affect normal tissue cells as well, thus the goal is to maximize the damage to tumour cells while sparing healthy tissues. In order to achieve this goal, it is essential to accurately know the radiation dose delivered to the patient.

Recent developments in radiation therapy include more advanced delivery techniques and equipment. Intensity modulated radiotherapy (IMRT), volumetric modulated radiotherapy (VMAT), stereotactic radiosurgery (SRS), and stereotactic radiotherapy (SRT) are well-established techniques for more accurate dose delivery. These techniques can be delivered with the use of conventional linear accelerators equipped with standard and high resolution multi-leaf collimators. The most pronounced feature of these techniques is the increased use of small and irregular photon beam apertures, which can better conform to the tumour, minimizing unnecessary dose to healthy tissues. However, larger numbers of such beams is a challenge for accurate dose calculation and its dosimetric validation. If dosimetry is uncertain, underdosing of the tumour or overdosing of the healthy tissues can occur resulting in poor treatment outcomes for the patients.

Experimental dosimetry under small field conditions has been challenging for several reasons. Finite source size, lack of electronic equilibrium, and detector size

limitations all cause changes in the energy spectrum and detector response resulting in unreliable measurements. Additionally, institutional variability in terms of procedures, standards, and detector availability contribute to lack of well documented and correctly understood information in this field. For example, SRS dosimetry has been uncertain up to 14% between institutions and detectors [32]. The International Commission on Radiation Units and Measurements (ICRU) recommends an overall uncertainty on the accuracy of dose delivered to the tumour of 5%, thus the 14% discrepancy is unacceptable. Modeling of radiation interactions and transport within the linear accelerator, detector, and patient has led to development of Monte Carlo simulations of dose deposition. These computational methods can be quite accurate, however, they are extremely time consuming and clinical implementation has proven to be challenging. To make these models compatible with fast-paced clinical workflow, many approximations are implemented to estimate the dose, which might not represent the true dose distribution. Thus, much research is needed to characterize currently available detectors suitable for small field conditions and to compare results against Monte Carlo methods.

Recently, two new dosimeters have been released—SRS MapCHECK and HYPERSCINT. One is a diode array with a resolution of 2.5 mm and the other is a scintillation based point dosimeter with a resolution of 1.0 mm. In the work presented in this thesis, these dosimetry systems have been meticulously characterized focusing on characteristics particularly relevant for dosimetry in small fields. Furthermore, SRS MapCHECK, which is currently being used clinically, has been compared against computational dosimetry methods to shed light on its limitations under extreme clinically challenging conditions.

Chapter 2 lays the foundation of the physics principles underlying small field conditions, dosimetry, suitable detectors, and computational dosimetry methods. The focus of chapter 3 is dosimetric characterization of HYPERSCINT. This study characterizes the detector as a dosimeter for small fields. Chapter 4 describes and characterizes SRS MapCHECK with applications to small fields. Since, SRS MapCHECK in already in clinical circulation, this chapter focuses on establishing a baseline performance and begins to push the boundaries on clinical field conditions where the performance may breakdown. Chapter 5 further address extreme clinical conditions under which SRS MapCHECK measurements show considerable differences in comparison with computationally calculated dose distributions. Main areas addressed include small fields, fields with high degree of modulation, and off-axis measurements. The main results

are summarized in chapter 6.

Chapter 2

Background

2.1 Linear Accelerator

External beam radiation therapy can be delivered with the use of a linear accelerator (linac). X-ray beams, which are used to treat patients, are generated by bombarding a high atomic number target with high energy electrons. The primary collimator absorbs scatter from the target which is not directed at the beam opening. The x-ray beam profile is Gaussian shaped, thus a flattening filter (thicker in the center, and is optional) can be used to flatten the profile. Secondary collimators, also known as the jaws, are made up of highly attenuating material used to shape the beam into a rectangular shape. Multi-leaf collimators, also highly attenuating, are used to further shape the beam [67]. For SRT applications, the typical multi-leaf collimator leaf width ranges from 2.5 to 5 mm [95]. These components are shown in Figure 2.1.

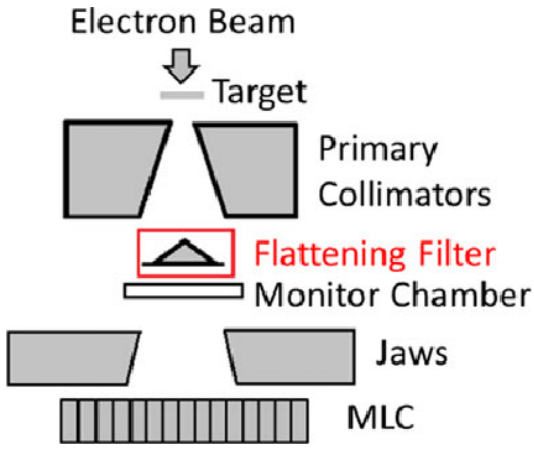

Figure 2.1: Common configuration of linac head components. [67].

2.2 Photon and Electron Interactions

External radiation therapy is typically delivered via photon beams produced by a linear accelerator. The ICRU and IAEA recommend energy ranges up to and including 10 MV for treatments involving small fields such as IMRT and VMAT delivery modes. This is mainly due to better modulation for lower energy beams (characterized by narrower penumbra due to lower MLC transmission, less electron lateral disequilibrium at lower energies) and much lower neutron production cross sections. Hence, this thesis focuses on 6 MV and 10 MV energy beams. [100]

Photon beams are a form of indirectly ionizing radiation. Photons can interact with matter through several processes, the photon interaction processes of interest are photoelectric effect, Compton scatter, and pair production. Through these interactions electrons are produced depositing energy into the interaction medium contributing to absorbed dose.

2.2.1 Photoelectric Effect

In the photoelectric effect, the incident photon interacts with a tightly bound electron of an atom. If the photon's energy is greater than the binding energy of the electron, that electron is ejected with energy equal to the incident photon's energy minus the electron's binding energy. The vacancy left by the ejected electron can be filled by a higher shell electron and that transition energy is released as either an Auger electron or as a characteristic x-ray. The interaction cross section or probability of interaction for photoelectric effect is proportional to Z^3/E^3, where Z is the atomic number of the medium and E is the energy of the incident photon. As such, photoelectric effect dominates in high Z media at low energies. This effect is demonstrated in Figure 2.2.

2.2.2 Compton Scattering

Compton scattering, also known as incoherent scattering, is defined by an incident photon interacting with a loosely bound atomic electron thereby producing a scattered photon and a recoil electron. The energies of the scattered photon and the recoil electron are governed by the incident photon energy and the angle of scatter, given by equations below. Atomic cross section for Compton scatter depends on the electron density of the medium and is proportional to Z. Compton scattering dominates in low to medium energies [86], [47], [48]. The effect is illustrated in Figure 2.3.

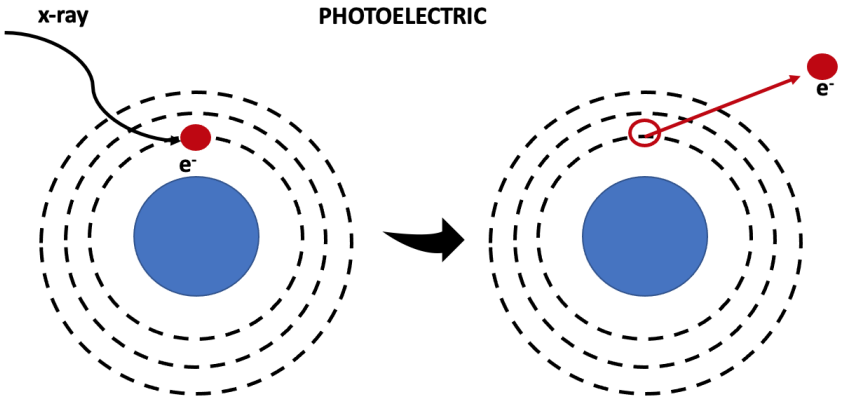

Figure 2.2: Visual representation of photoelectric effect.

Energy of scattered photon is given by

$$h\nu^{'} = h\nu \frac{1}{1 + \epsilon(1 - cos\theta)} \tag{2.1}$$

where hν is the incident photon energy, θ is the photon scatter angle, and ϵ is the normalized incident photon energy given by $\epsilon = \frac{h\nu}{m_e c}$ (m_e is mass of electron and c is speed of light).

Energy of recoil electron is given by

$$E_e(h\nu, \theta) = h\nu \frac{(1 - cos\theta)}{1 + \epsilon(1 - cos\theta)} \tag{2.2}$$

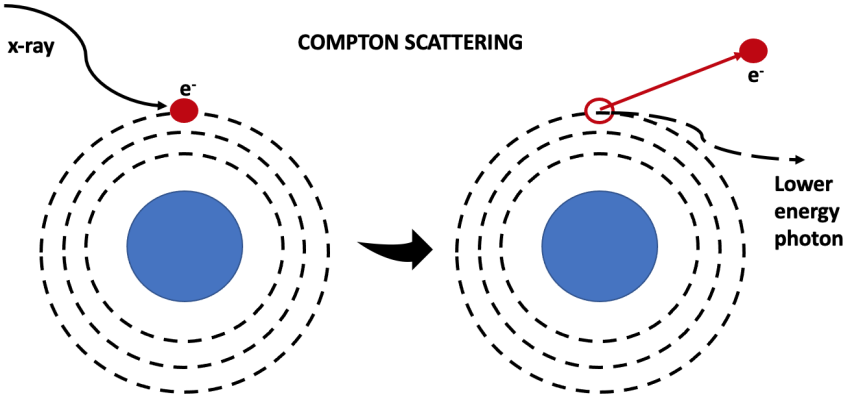

Figure 2.3: Visual representation of Compton scatter.

2.2.3 Pair Production

In a pair production interaction, the incident photon interacts with the Coulomb field of an atomic nucleus to produce an electron-positron pair. The incident photon must have energy greater than 1.022 MeV (combined rest mass energy of electron and positron) and completely disappears following the interaction. The electron and positron are emitted in opposite directions with their combined energy equal to the energy of incident photon energy minus 1.022MeV. The cross section of pair production is proportional to Z^2 and rapidly increases with incident photon energy. Pair production dominates at high energies. [86], [47], [48]. This effect can be seen in Figure 2.4.

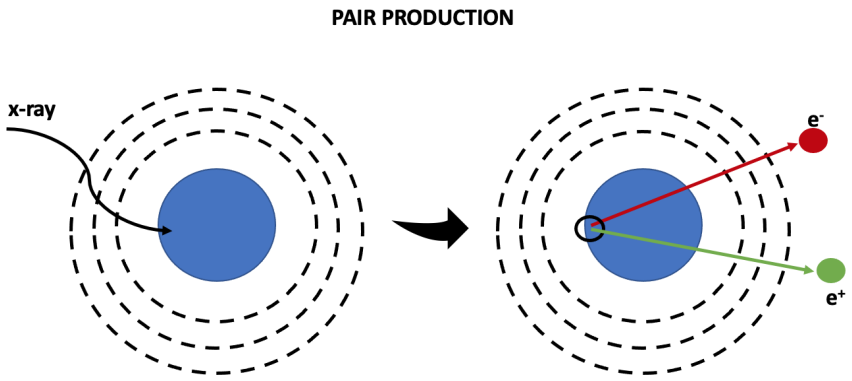

Figure 2.4: Visual representation of pair production.

2.2.4 Electron Interactions

Electrons have several energy loss mechanisms including radiative losses through Bremsstrahlung radiation and collisional losses through ionization and excitation of atoms (shown in Figure 2.5). When an electron is deflected through an interaction with the Coulomb field of a nucleus, it slows down releasing some of its kinetic energy by emitting photon radiation called Bremsstrahlung [85], [53], [100]. The probability of Bremsstrahlung radiation is very low for low Z materials and for low energy electrons. To provide more context, the contribution of radiative energy losses by electrons in water becomes relevant at energies around 30 MeV and higher [100]. See Figure 2.6 for electron stopping powers in water. These energies are not encountered in external radiation therapy delivered with a conventional linear accelerator, thus radiative components can be safely ignored as the mechanisms for patient dose

deposition. Collisional losses occur through inelastic collisions of free electrons and atomic electrons, leading to either excitation or ionization in the case where incident electron energy is larger than the binding energy of the atomic electron. Electrons will undergo thousands of interactions before losing all of their energy in the absorber medium and have varying track lengths until full energy deposition [85], [100], [53].

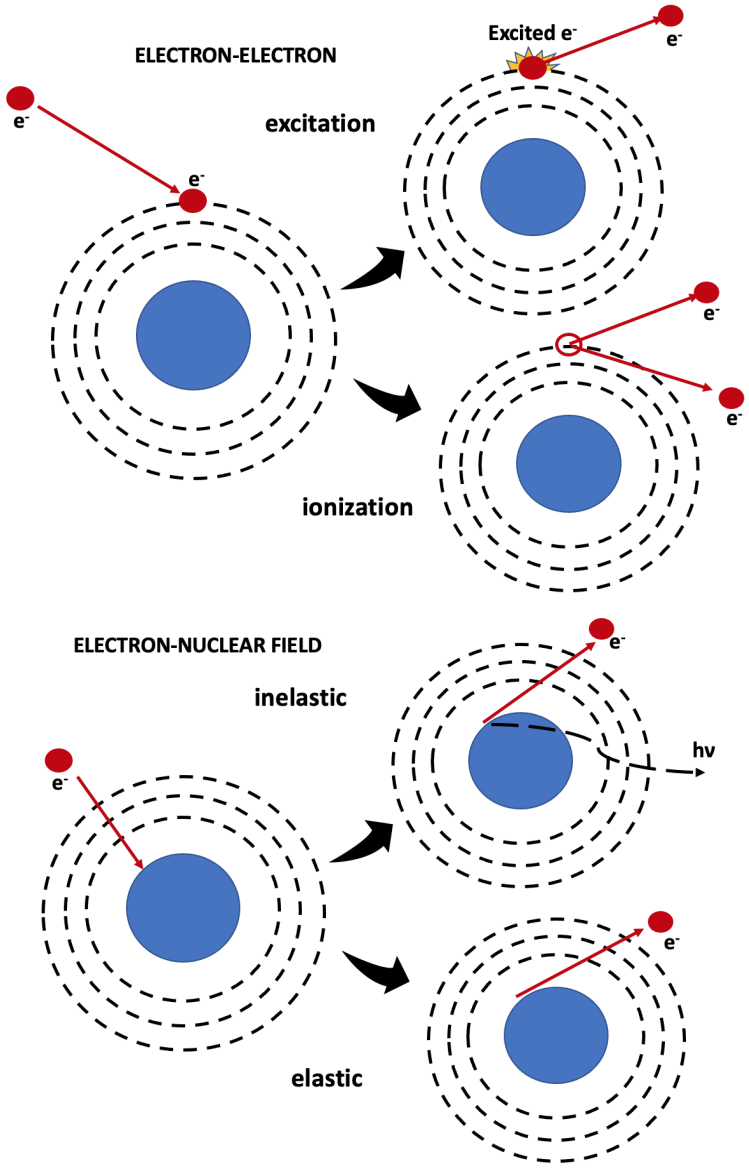

Figure 2.5: Visual representation of electron interactions.

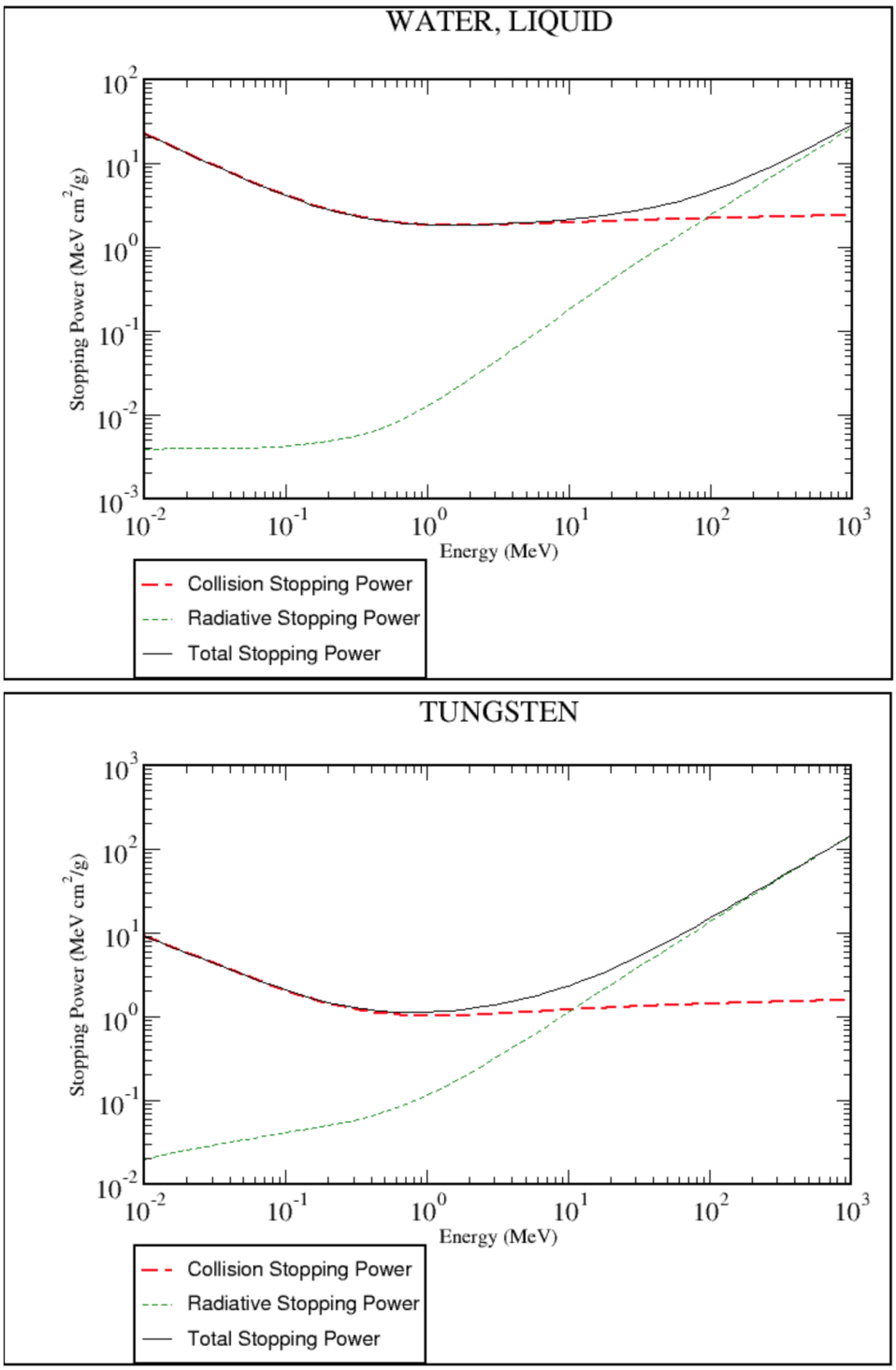

Figure 2.6: Electron stopping powers in water (top) and tungsten (bottom). Included are radiative, collisional, and total stopping power. [18]

2.3 Dosimetry

2.3.1 KERMA and Absorbed Dose

Kerma, K_{med}, is defined as mean energy transferred from the incident photon to the liberated electrons in the medium per unit mass. For photons, it consists of two components, collision kerma and radiative kerma. Radiative kerma is often very small and considered to be negligible. Collision kerma is equivalent to absorbed dose to the medium if charged particle equilibrium (CPE) conditions are met [53].

CPE is maintained when any charged particle with energy E leaving a volume is replaced by another charged particle with the same energy E, expending that energy within the volume. This effectively means that any energy carried outside of a volume is replaced with the same amount of energy, thus maintaining electronic equilibrium. Therefore, absorbed dose is only equal to collision kerma for that volume under CPE conditions. Absorbed dose is measured in Grays (Gy) and is the most important quantity for radiation dosimetry as it directly represents the total amount of energy imparted to a medium [53].

2.4 Physics of Small Field Dosimetry

2.4.1 Small Field Conditions

In external beam radiation therapy, small fields are created with the use of collimation devices, such as jaws, MLCs, and cones, located downstream of the photon beam. As fields decrease in size, eventually their penumbra begin to overlap and the active volume of common detectors becomes too large relative to the field size. This leads to dosimetric challenges, which will be further described in this section.

There are three conditions which define small fields for an external photon beam, of which at least one must be met for a field to be considered small: i) loss of charged particle equilibrium on beam axis, ii) partial primary source occlusion on the beam axis by collimating device, iii) detector size is similar or large relative to beam dimensions. These conditions are related to either the beam or the detector, but all result in overlap of field penumbra and detector volume being too large compared to the field size.

Beam Related Conditions: Loss of lateral charged particle equilibrium on the beam axis

When the range of the secondary electrons contributing to absorbed dose is larger than the radius of the photon beam (ie. distance from field edge to central axis), there is a loss of lateral charged particle equilibrium (LCPE) [11].

A practical parameter for defining when field size is considered small is the lateral charged particle equilibrium range r_{LCPE}; the minimum radius of a circular photon beam for which collision kerma in water and absorbed dose to water are related by a constant factor at the center of the field. The secondary electron range can be defined by the equation from IAEA TRS-483 [1] as

$$r_{LCPE} = 8.369 * TRP_{20,10}(10) - 4.382 \tag{2.3}$$

Where r_{LCPE} is given in cm and $TPR_{20,10}(10)$ is the photon beam quality index tissue phantom ratio at depths of 20 and 10 g/cm^2 for field size of 10 x 10 cm^2 at SSD of 100 cm.

Crudely estimating r_{LCPE} for a 6 MV beam.. we know that the mean beam energy is roughly 1/3-1/2 of the maximum. Knowing that electron range in water is 0.5 cm/MV, we can estimate that the r_{LCPE} is 1-2 cm. So fields with radius in this range or smaller are considered to be small fields.

The dosimetric problem arises from fluence perturbation by the presence of a detector, specifically the exaggerated fluence perturbation under LCPE.

2.4.2 Beam Related Conditions: Partial primary photon source occlusions by collimating device on axis

The primary photon source size is defined as the full width half maximum (FWHM) of the bremsstrahlung photon fluence distribution. When the collimating device shields part of that primary photon source, the beam output is lowered on the central axis, effect shown in Figure 2.7. Essentially, linear accelerator (linac) output becomes dependent on the collimator position. This is an important condition when the field size is comparable to or smaller than the source size, in modern linacs this is about 5 mm. Partial source occlusion affects the energy spectrum and is a source for steep local absorbed dose gradients, which can affect the detector response. The main concern is reduction in beam output with decreasing field size due to both source

occlusion and loss of LCPE. The output drop is more pronounced with increasing beam energies or decreasing density of the medium, as the r_{LCPE} increases under these conditions [1].

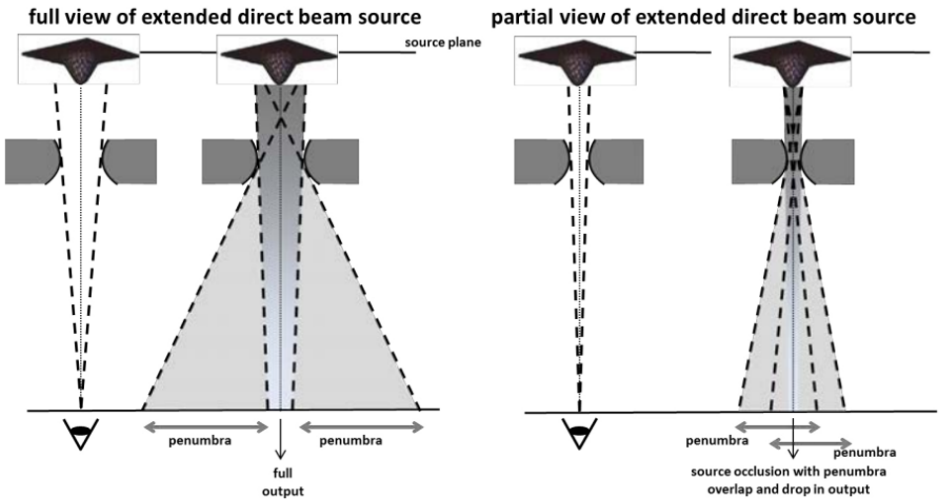

Figure 2.7: Visual representation of source occlusion effect. [1].

2.4.3 Detector Related Conditions: Size of detector is similar or larger than the beam dimensions

When the detector size is comparable to the field size dimensions, two problems arise: i) volume averaging and ii) perturbation of charged particle fluence.

A detector averages the dose over its active volume. When dose inhomogeneity is present across this volume, the detector's response will under-estimate the dose to the center, overestimate the dose to the periphery, and spread out the penumbra. These effects are shown in Figure 2.8. Volume averaging has detrimental effects on measuring output factors, reference dosimetry, and profile measurements—all important parameters for treatment planning, commissioning, and quality assurance measurements [1], [113].

2.4.4 Detector Related conditions: Detector material

The detector's presence can cause perturbation of charged particle fluence. Especially evident when the detector material is quite different from the interaction medium as the way radiation interacts with the detector material could be different from

the way it interacts with the medium. Particularly the number of interactions, the energy losses, and directional changes of charged particles could be different [33], [11]. Fluence perturbations become large at steep dose gradients and with the loss of lateral charged particle equilibrium, to the point they are difficult to model [1].

IAEA TRS-483 suggests the detector volume is too large when its diameter is equal to or larger than the field FWHM – 2*r_{LCPE}.

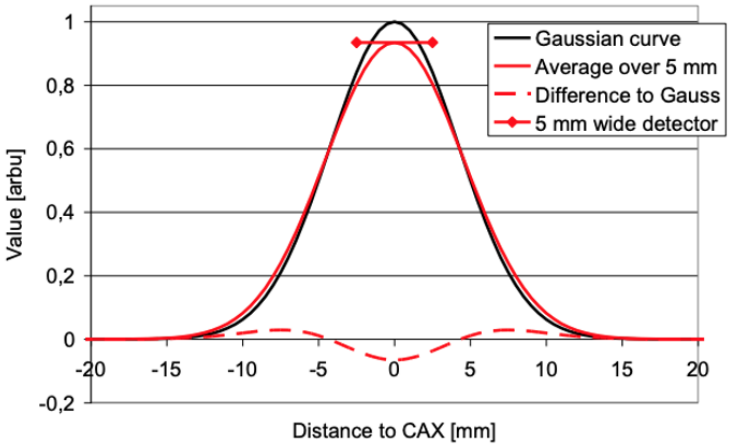

Figure 2.8: Gaussian curve represents the true dose profile. The detector is approximately equal to the FWHM of the dose profile. The detector response is under estimating the dose at the center, over estimating the dose at the periphery of the profile, and broadening the penumbra. Dashed line shows percent difference between true profile and the detector measured profile. [113].

2.5 Defining Field Size

There are two ways to define the field size in external beam radiotherapy—geometric and irradiation field size. Geometric field size is equivalent to the dimensions of the light field projection of the collimator setting on a plane perpendicular to the beam axis. The irradiation field size is the FWHM of in-plane and cross-plane (lateral) profiles measured at a plane perpendicular to the beam axis. This can also be thought of as measuring the field size at the 50% isodose line [51]. In broad beams, the geometric field size is equivalent to the irradiation field size at isocenter, but this is not the case for small fields. Due to the reduced beam output caused by partial source occlusion and loss of lateral charged particle equilibrium, described in the previous

section, the 50% isodose line is now found lower along the penumbra resulting in a wider field. This is termed apparent field widening or penumbral broadening. This effect can be seen in Figure 2.9. Penumbral broadening is also dependent on the source-to-collimator distance, hence the effect can be different on different machines [1].

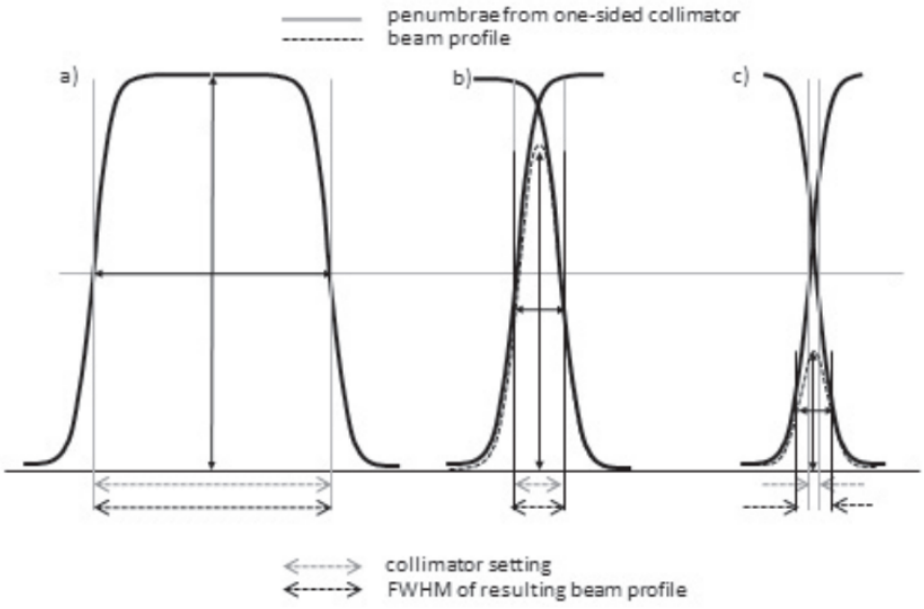

Figure 2.9: Apparent field widening due to overlapping penumbra. [1]

There has been data published showing that detector response and perturbation is dependent on the field size specified by the 50% isodose line rather than the collimator setting, and large errors occur if correction factors are chosen based on the incorrect field size [29]. Thus, the IAEA TRS-483 concludes that the irradiation field size is the most representative parameter for accurate small field dosimetry. It is advised to report both, the geometric and the irradiation field sizes.

2.6 Formalism for Small Field Dosimetry-Field Output Factors

An important factor in dosimetry is the field output factor given by the ratio of absorbed dose to water in a clinical field to absorbed dose to water in a reference field at a specified depth, described by the following equations. Typically, the reference

field, also called machine specific reference (msr) field, is 10 x 10 cm^2 and a clinical field is a field other than the reference field. For conventional broad beams, the field output factor is simply the ratio of detector readings taken at the reference and the clinical fields. For small fields, a correction factor needs to be applied to the ratio of readings mainly to account for perturbation effects of the detector. When the detector is not perfectly equivalent to water, the ratio of readings compared to the ratio of absorbed dose to water, under the same conditions, is not equivalent [5]. Written mathematically, the field output factor equation becomes

Field output factor:

$$\Omega_{Q_{clin},Q_{msr}}^{f_{clin},f_{msr}} = D_{W,Q_{clin}}^{f_{clin}} / D_{W,Q_{msr}}^{f_{msr}} \tag{2.4}$$

Field output factors from detector readings with correction:

$$\Omega_{Q_{clin},Q_{msr}}^{f_{clin},f_{msr}} = \frac{M_{W,Q_{clin}}^{f_{clin}}}{M_{W,Q_{msr}}^{f_{msr}}} * k_{Q_{clin},Q_{msr}}^{f_{clin},f_{msr}} \tag{2.5}$$

The output correction factor can be determined as an experimental generic value or a Monte Carlo calculated generic value (this simply means that the correction factor is not machine specific). The correction factor is mathematically expressed as

$$k_{Q_{clin},Q_{msr}}^{f_{clin},f_{msr}} = \frac{D_{W,Q_{clin}}^{f_{clin}} / \bar{D}_{det,Q_{clin}}^{f_{clin}}}{D_{W,Q_{msr}}^{f_{msr}} / \bar{D}_{det,Q_{msr}}^{f_{msr}}} \tag{2.6}$$

Where D_w is mean absorbed dose to water over a small volume around the measurement point, and D_{det} is the mean absorbed dose to detector volume [1]. TRS-483 recommends that detector specific output correction factors fall within 5% for a particular machine.

2.7 Detectors

As described in the previous sections, there are some challenges for small field dosimetry such as steep dose gradients, volume averaging, lack of LCPE, and partial source occlusion. As a result, a detector suitable for use in small field dosimetry has more stringent criteria for its properties and characteristics.

Generally, the detector's response is stable over time, linear with dose, independent of energy, dose rate, and direction. The detector itself is small enough in size as

to avoid volume averaging and provide high spatial resolution. Finally, the measurements are not affected by environmental conditions such as temperature, humidity, atmospheric pressure, and any background signal is minimal [9]. The objective of this thesis is to evaluate the properties, characteristics, and performance of two novel dosimetry systems targeted towards small field dosimetry (or least offer potential applications in small field dosimetry). One of these systems is scintillation based and the other is a diode array, both are described in the following sections. Additionally, PTW60019 microdiamond detector, which was used for verification, and Gafchromic RTQA2 film, which was used for profile measurements, are described.

2.7.1 Plastic Scintillator

A plastic scintillator detector (PSD) is based on light production during irradiation. Typically, the detecting element is composed of a bulk medium, such as polyvinyltoluene, and an organic fluor molecule, such as an aromatic or cyclical hydrocarbon chain. The orbital electrons of the organic molecule have a ground electronic state and several excited electronic states (solid lines in Figure 2.10). Within these electronic states, there are several vibrational states (dashed lines in Figure 2.8) due to vibration of the molecule's atoms. The spacing between electronic states is on the order of 1 eV, while the spacing of the vibrational states is about 0.1 eV [62].

When a charged particle passes near an organic scintillator (fluor) molecule, some of its kinetic energy is transferred to the organic molecule. This process elevates the molecule's orbital electrons into combinations of excited electronic and vibrational states, which all de-excite to the first excited electronic state through radiationless internal conversion within picoseconds. This leaves a group of electrons in the first excited state to de-excite to the ground state via a photon emission on the order of a few nanoseconds. This is called prompt fluorescence and is the light typically associated with a scintillation detector [62]. Due to the energy level structure, emitted light has a lower frequency than the light an organic molecule can absorb, hence PSDs are transparent to their own emissions [19]. Finally, the emitted light is collected through an optical fiber and readout using a photosensor such as a photodiode.

In terms of their characteristics, PSDs are the closest to the ideal small field dosimeter. They can be almost water equivalent based on electron density and atomic composition. As such, their mass energy absorption coefficient, mass collision stopping power, and mass angular scattering power match those of water within 2% in

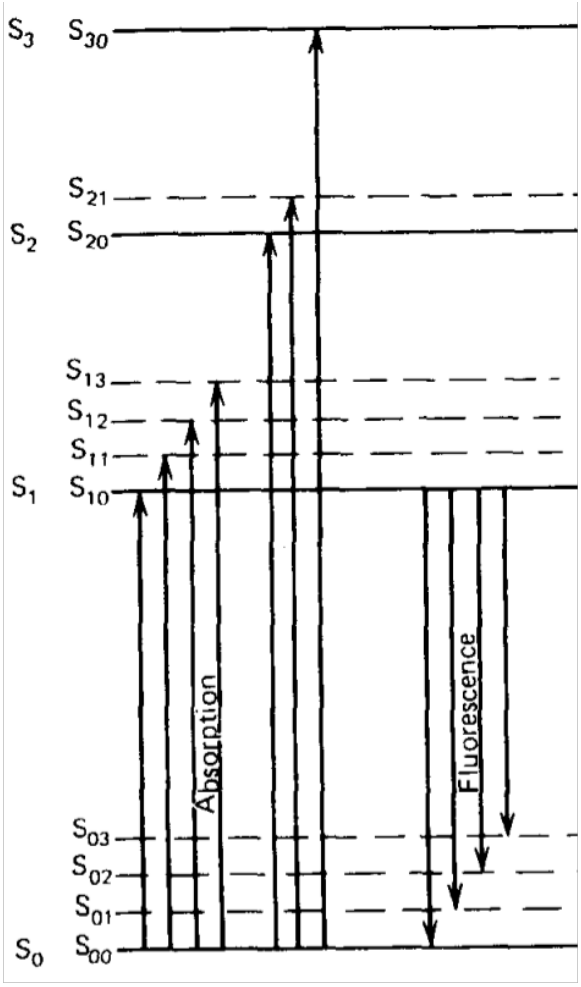

Figure 2.10: Visual representation of energy band structure of organic scintillators. [19]

the therapeutic energy range [1], [13], [14]. The perturbation correction factors for scintillators are close to unity [1]. Their emitted light is directly proportional to the energy deposited by electrons, which makes them energy independent and gives them a linear response with dose [1], [13], [14]. Beddar et al.[13], also demonstrated that the response of PSDs is independent of dose rate, angle of irradiation, and the total dose. Additionally, PSDs can be manufactured with sizes less than a 1 mm^3 providing high spatial resolution.

The main concern with PSDs is the Cherenkov light production in non-fluor components like the optical fiber and housing, which distorts the fluorescence signal. There are numerous methods for Cherenkov correction including subtraction of the Cherenkov signal. It has been shown that the PSDs can lose about 3% of their output

after irradiation to 10 kGy and that they can have a slight temperature dependence. An increase in response of about 0.2% with temperature from 30°C to 50°C [13] or a decrease in response of about 0.09-0.7% per °C as temperature is increased from 15 to 40°C [112], [23]. However, this slight change in output with temperature introduces less than 0.5% of error into the measured dose, so it can be considered inconsequential.

2.7.2 Solid-state Detectors-Diodes

Diodes are made of semiconductors which embody the properties of materials which conduct electricity and materials which do not. Their properties can best be explained in terms of the band structure of solids. Crystalline materials form a lattice containing energy bands where electrons can exist, seen in Figure 2.11. The valence band contains the outer bound electrons of atoms fixed to specific lattice positions, while the conduction band contains free electrons contributing to the conductivity of the material. These two bands are separated by the band gap energy, on the order of 1 eV for a semiconductor. In a semiconductor, under no thermal excitation, the valence band is occupied fully with bound electrons and the conduction band is completely empty of electrons, and thus behaves as an insulator. When an electron in the valence band gains enough energy (for example, an interaction with a secondary electron), its elevated to the conduction band, where it can drift under an applied electric field. The typical drift velocity is approximately 10^7 cm/s, so it would take 10 ns for electrons to drift 10 mm, making semiconductors some of the fastest responding detectors available.[62].

Semiconductors are often doped with impurities to change their properties. These dopants are either electron donors or electron acceptors, classing the semiconductor as either n-type or p-type, respectively. Net effect in either type is simply increased mobility of charge carriers due to lower binding affinity of electrons. These two types can be adjacent to each other forming a p-n junction. N-type side has a higher concentration of electrons compared to the p-type side, creating a charge discontinuity which causes a net diffusion of electrons to the p-side—forming a negative space charge on the p side and a positive space charge on the n side. This space charge distribution is called the depletion region. As a result, an electric potential difference and an electric field are established (see Figure 2.12). This means that any electron-hole pairs created in the depletion region, such as a result of radiation interactions, will be swept to the appropriate side creating an electric current. This process can

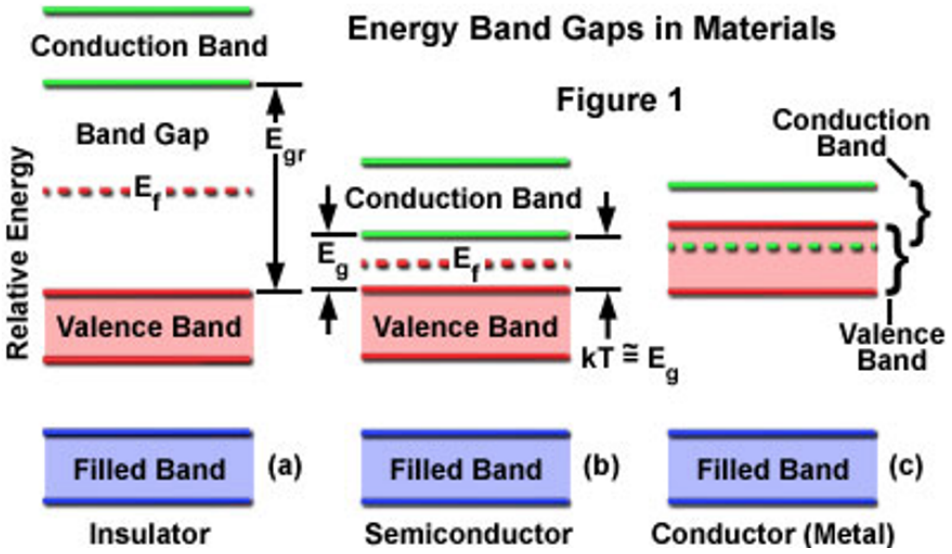

Figure 2.11: Visual representation of energy band structure of solids. Taken from https://warwick.ac.uk/fac/sci/physics/current/postgraduate/regs /mpagswarwick/ex5/bandstructure/

be amplified through reverse biasing—which effectively forms a diode by allowing current flow in one direction. [62].

As a charged particle passes through a semiconductor, it ionizes valence electrons creating many conduction electron-hole pairs within picoseconds. Electrical contacts on either side of the crystal apply an electric field allowing charge collection. The number of electron-holes pairs can be directly traced back to the energy deposited by the incident radiation. Semiconductors have much lower ionization energy compared to other detector types such an ionization chamber (ex. Silicon 3 eV, gas-filled detector 30 eV), thus many more electrons are created per energy spared allowing higher energy resolution and high signal to noise ratio. [62].

Silicon Diode

Silicon diodes can be manufactured to very small sizes with sensitive volumes less than 0.2 mm^3 [111] minimizing effects of volume averaging. Due to mass energy absorption coefficient differences between silicon and water, diodes over-respond to low energy photons (in the keV range). Recalling that in small fields scattered radiation is reduced, thus the contribution of low energy photons is also reduced, this effect is minimal [1]. Output correction factors need to be applied for fields smaller than 1 cm [31]. The diode sensitivity depends on lifetime accumulated dose, which limits their

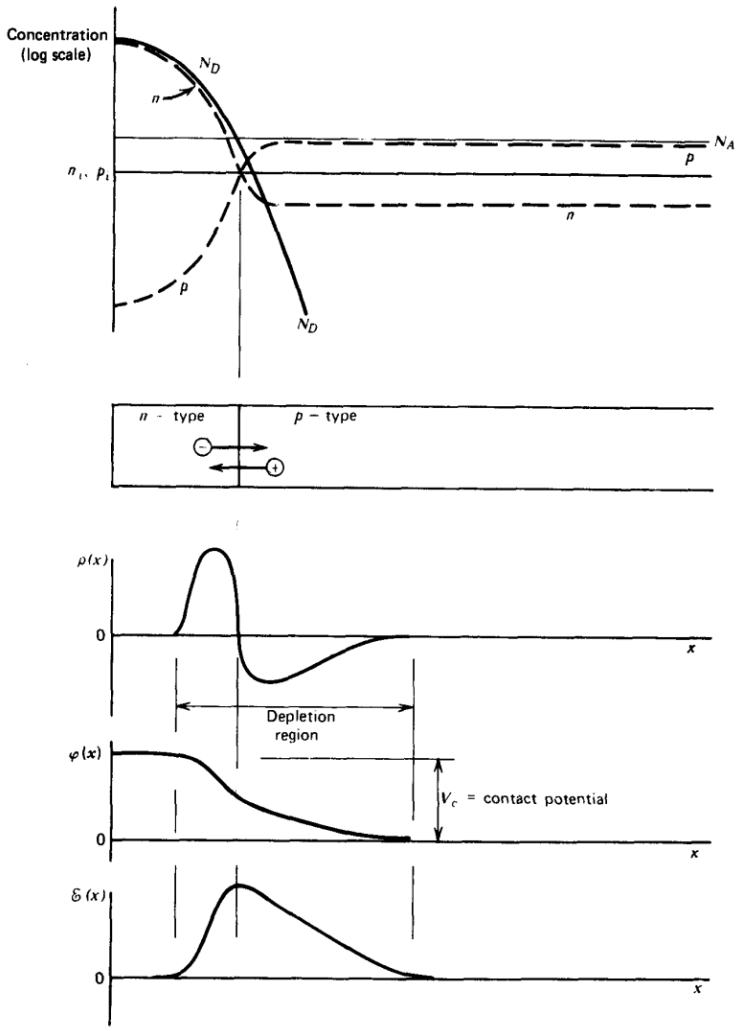

Figure 2.12: Depletion region, formed as a result of Coulombic interactions at a P-N junction, has an electric potential and electric field causing any charges generated in this region due to radiation interactions to generate a current proportional to the dose deposited. [62].

lifespan [1]. Silicon diodes have a directional dependence/angular dependence [111].

MicroDiamond

Due to nearly identical stopping-power and mass energy absorption coefficients of diamond and water, MicroDiamond detectors have a response almost independent of energy. They offer high sensitivity and can be manufactured to really small sizes (less than 0.5 mm). However, they do require substantial pre-irradiation and corrections for absorbed dose rate variance [34]. Output factor corrections need to be applied for fields smaller than 1 cm [91]. They offer a uniform response independent of direction of irradiation [**?**].

2.7.3 GafChromic Film

Radiochromic film functions based on the premise of a radiation sensitive monomer changing colour as a result of polymerization caused by radiation exposure. The measured property is the light absorption, which is directly related to the absorbed dose. More absorbed dose means a darker film, hence less light transmission.

For the work in this thesis, RTQA2 Gafchromic film (Ashland, Covington, KY, USA) was used to measure dose profile width to determine the field size. This film comes in a four layer laminated configuration, shown in Figure 2.13, with the active layer laminated between two polyester layers. The polyester layers physically protect the active layer from wear and light effects, and allows water immersion. Substrate 1 is an opaque white polyester with barium sulfate whitening agent. The higher atomic number due to presence of barium sulfate boosts photoelectric absorption and increases the film's sensitivity [37]. The active layer consists of microcrystals of lithium salt of Pentacosa-10,-12-diynoic acid (Li-PCDA) dispersed in a water soluble polymer matrix [80]. Li-PCDA belongs to the class of diacetylene hydrocarbons which undergo a chain polymerization reaction due to radiation exposure [87]. This polymerization results in a blue coloured polymer. The adhesive layer uses a pressure sensitive acrylic adhesive to bond substrate 2 to the active layer [80], [37]. Substrate 2 is a yellow polyester that absorbs blue and ultraviolet light reducing light exposure to which the active layer is most sensitive. The colour yellow is also complimentary to the colour blue (the colour of the polymer) allowing enhanced visualization of the colour change [36].

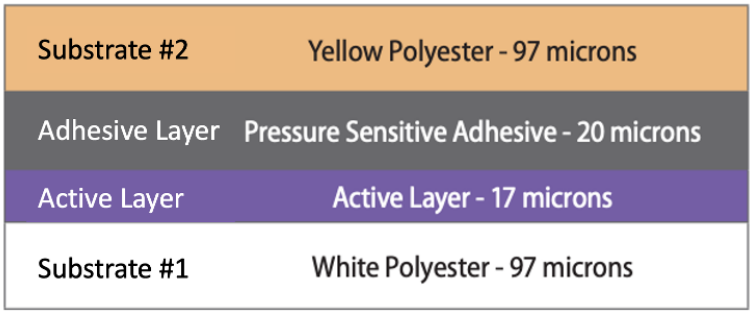

Figure 2.13: Gafchromic RTQA2 film four layer laminated composition. Figure adapted from Ashland RTQA2 Gafchromic film information sheet.

Radiochromic films exhibit water and soft tissue equivalence, thus are considered to be nearly energy independent [16], [36]. Some studies report energy independence to within 1-5% in the 40 keV to MV energy range [16]. They also show no dose rate dependence [1]. Li-PCDA changes purely based on the net dose absorbed, not the rate of delivery or the number of fractions. RTQA2 gafchromic films offer high spatial resolution (5 um), a wide dynamic dose range (0.02-8 Gy), low sensitivity to light [80], and are considered waterproof, so they can be used for water tank measurements. Although, the polymerization reaction occurs immediately, it can take up to 24h to fully complete. The films can darken with ambient light exposure over 1h long. The film's transmission properties can change with temperature (over 60^o)[63] and relative humidity changes (over 60% relative humidity), thus require a level of environmental control. Though, the humidity effects can be mediated by adding alumina to the active layer [80]. TRS 483 recommends use of radiochromic film for measurement of small beam profiles.

2.8 Dose Calculation Algorithms

During radiation treatment planning, it is very important to accurately calculate the dose to the tumour and surrounding tissues to ensure that prescribed dose is delivered to the tumour, while minimizing excess dose to normal tissues. In a clinical setting, the treatment planning system (TPS) performs these calculations based on selected parameters in a timely manner to cope with clinical load. Modern TPS algorithms fall into the category of model-based dose calculation algorithms utilizing primary particle fluence and a dose kernel to predict the dose distribution [61]. Another category is principle based, or Monte Carlo, dose calculation algorithms focusing on the physical

processes of particle transport through matter to calculate the dose distribution [61]. Monte Carlo calculations are considered to be the most accurate method available and are seen as the gold standard [61], [73], [43]. The following sections describe the basic principles of operation of TPS and Monte Carlo dose calculation algorithms relevant to the research presented in this thesis.

2.8.1 Treatment Planning system

Today, there are two main classes of TPS dose calculation algorithms including superposition/convolution and linear Boltzman transport equations (LBTE) numerical solvers. This section describes how each one works.

Superposition/convolution algorithms

Superposition/convolution algorithms can be summarized in four steps. First, the primary energy fluence of the linac is modelled. This represents the radiation output of the machine and serves as the input for fluence transport and energy absorption and transport in the next steps. Radiation output is a mixture of primary photons, scattered photons, and electrons each with an energy spectrum, velocity spectrum, and lateral distribution in a defined plane perpendicular to the central axis. This defines the phase space, which can be calculated with Monte Carlo techniques (Monte Carlo described in the next section). The creation of photons from an electron beam incident on the target, and subsequent attenuation and scatter of these photons through all linac head components, is modelled in order to create the phase space [81].

Next, the phase space is used to calculate the absorption of primary photons through total energy released per unit mass (TERMA). TERMA is effectively described by the rate of photon interactions in a medium of density ρ, estimated from CT number values [73]. The rate at a given point $\vec{r}$ is written as

$$T(\vec{r}) = \mu/\rho * (\vec{r}) * \Psi(\vec{r}) \tag{2.7}$$

$$\Psi(\vec{r}) = \Phi(\vec{r}, 0) * E * e^{-\mu(E)} \tag{2.8}$$

Where μ/ρ is the linear photon absorption coefficient and Φ is the primary energy fluence [81], [61]. This is the locally released energy which can be further transported away from the interaction point $\vec{r}$, and this transport is described via dose kernels.

Two of the most common dose kernels are point spread kernel [77], [69], [4] and pencil beam kernel [77], [20] (Figure 2.14). The point spread kernel describes the absorbed energy distribution in water at a fixed point due to the interactions of monoenergetic photons from a pencil photon beam, including all subsequent interactions. This simply provides the average energy fraction of the incident photons deposited in each small volume element around the interaction point. The dose kernel for water can be scaled by electron density of another medium in a processes called ray tracing [77] to calculate dose to various materials. The pencil beam kernel integrates all of the point spread kernels along the direction of the pencil beam resulting in a much faster calculation speed, but coarser resolution thus less accuracy. One adaptation of the pencil beam kernel is anisotropic analytical algorithm (AAA) where lateral and depth components of the beam are separated allowing improved modelling of lateral energy spread and allows accounting for inhomogenieties in the medium [101], [98], [73].

Finally, the TERMA and dose kernel of choice are convolved to calculate the absorbed dose. Since dose kernels are calculated for monoenergetic photon beams, to account for the spectrum of the primary incident photon beam many dose kernels are modelled, and all the dose contributions to a fixed point are superimposed as follows

$$D(\vec{r}) = \int dE^{'} \int d^3r^{'} T(\vec{r}^{'}, E^{'}) k(\vec{r}, \vec{r}^{'}, E^{'}) \tag{2.9}$$

This method is computationally expensive, so a convolution approach was proposed where the dose kernel is assumed to be a function of distance between the interaction point and the point where dose is measured becoming

$$D(\vec{r}) = \int dE^{'} \int d^3r^{'} T(\vec{r}^{'}, E^{'}) k(|\vec{r} - \vec{r}^{'}|, E^{'}) \tag{2.10}$$

AAA

Analytical anisotropic algorithm (AAA) for photon dose calculations consists of a configuration module, which characterizes the phase space for a given linear accelerator beam, and a dose calculation module, which calculates the total dose through superposition of dose deposited by primary photons (radiation from the target), extrafocal photons (scatter photons from linac head components) and contamination electrons (mainly Compton generated electrons in the linac head). These three com-

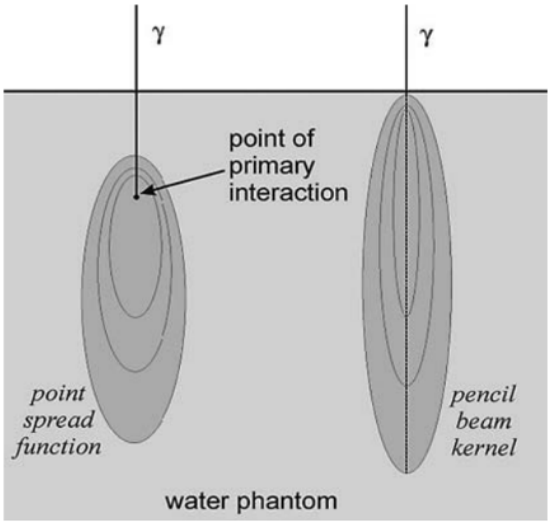

Figure 2.14: Left is point dose kernel describing energy spread about a single point by a primary interaction photon. Right is pencil beam kernel, which is an integration of point kernels along an infinitely thin ray. [81], [61].

ponents are part of the multiple source model and are optimized during algorithm commissioning through comparisons of measured dose to water to form the configuration module. To calculate dose to a volume, the beam is subdivided into beamlets and the volume is subdivided into voxels who's electron density is pre-determined based on computed tomography data of the volume. For each voxel, a polyenergetic beam kernel is constructed by superposition of pre-calculated monoenergetic beam kernels. Energy deposition is separated into lateral and depth components. The depth component describes total energy deposited per depth layer or plane, while the lateral component describes the lateral scatter of the dose in said plane. The energy deposited by a single beamlet into a point in the volume is given by the convolution of total energy for the plane where the point is located and the lateral scatter kernel. Thus, the total energy deposited in that voxel is given by the superposition of energy depositions from every beamlet. This is performed for every voxel in the volume to obtain an energy distribution, which is converted to dose by dividing by the local electron density. Dose by electron contamination is modelled via convolution of a lateral scatter kernel (usually a Guassian derived from the multiple source model commissioning) with the contamination electron fluence and multiplied by electron energy deposition with depth. Each scatter kernel, energy deposition function, photon and particle fluence is described independently and solved analytically. The convolutions

and final superposition are also solved analytically. [41], [103].

LBTE numerical solver

Boltzmann transport equations describe the behaviour of radiation, including photons, electrons, neutrons, and protons, as they travel and interact in a medium. When assuming that radiation interacts only with the medium and not itself, which is valid in absence of magnetic fields, then the behaviour is described by linear Boltzmann transport equations (LBTE). Vassiliev et al. [104] described a time-independent system of equations for LBTE as follows

$$\hat{\Omega} * \vec{\bigtriangledown}\Phi^{\gamma} + \sigma_t^{\gamma}\Phi^{\gamma} = q^{\gamma\gamma} + q^{\gamma} \tag{2.11}$$

$$\hat{\Omega} * \vec{\bigtriangledown}\Phi^{e} + \sigma_t^{e}\Phi^{e} - \delta/(\delta E) * (S_R\Phi^{e}) = q^{ee} + q^{\gamma e} + q^{e} \tag{2.12}$$

The first equation solves for photons while equation 1b solves for electrons. Φ^{γ} is the photon angular fluence and Φ^{e} is the electron angular fluence – describing the position, energy, and direction. σ^{γ} and σ^{e} are the macroscopic total cross sections for photons and electrons, respectively. In the second equation, the third term on the left-hand side is the restricted collisional and radiative stopping power of electrons representing the continuous slowing down approximation for soft collisions. Effectively, everything on the left-hand side describes the energy leaving a volume. On the right-hand side, the scattering, production, and extraneous sources of photons and electrons are found. Extraneous sources are photons and electrons directly entering the volume from say the linac head (q^{γ} and q^{e}). The scatter and production sources are governed by interactions between photons and photons ($q^{\gamma\gamma}$), photons and electrons ($q^{\gamma e}$), or electrons and electrons (q^{ee}). Effectively, this side of the equations represents the energy entering the volume.
These equation are solved for electron angular fluence, which is then used to obtain the dose for any region as

$$D_i = \int_0^{\infty} dE \int_{4\pi} d\hat{(}\Omega)\frac{\sigma_{ED}^{e}(\vec{(}r), E)}{\rho}\Phi^{e}(\vec{(}r), E, \hat{(}\Omega)) \tag{2.13}$$

σ_{ED}^{e} is the macroscopic energy deposition cross section and ρ is the density of the medium. The dose can be calculated as dose to water or dose to medium.

The LBTE equations are continuous equations applying to all directions, and in-

tegrating over all energies and angles. Practically, to solve the equations, they must be discretized. An algorithm for deterministically solving the LBTE outlined above, is Acuros XB. This algorithm is a grid-based Boltzmann solver, which discretizes the LBTE in space, angle, and energy, then iteratively solves it [104]. In space, Acuros XB discretizes using linear discontinuous finite element method [107] via adaptive mesh refinement (a cartesian mesh with variable sized elements, refining element size near steep photon gradients and medium heterogeneities). This provides a linear solution within elements making up a volume with discontinuities at boundaries between elements. In energy, Acuros XB discretizes using linear discontinuous finite-element method and the standard multigroup method [65]. In angle, Acuros XB discretizes using the discrete ordinates method [15]. Generally, all of these methods transform the continuous variables of space, energy, and angle into discrete intervals transforming the integral into a weighted summation.

AXB

Acuros XB Advanced Dose Calculation algorithm (AXB) for photon dose deposition iteratively solves the Linear Boltzmann Transport Equations (LBTE). This algorithm also consists of two modules. The configuration module is the same as described for AAA. Conceptually, AAA and AXB have the same multiple source model, but through the commissioning process different values are obtained for parameters optimally describing the source. Parameters include, but are not limited to, mean radial energy of primary photons, mean radial energy of extrafocal scatter photons, intensity profiles of primary and scatter photons, and width of Gaussian for contamination electron scatter. The dose per voxel is calculated by solving for the electron angular fluence over the total volume. Effectively, AXB discretizes space, angle, and energy in order to solve for electron angular fluence. Space is discretized using discontinuous linear finite-element method. Energy is discretized using standard multigroup method and linear discontinuous finite-element method. Angle is discretized using standard discrete ordinates method. [104].

2.8.2 Monte Carlo

Monte Carlo (MC) technique is the most accurate technique to solve the LBTE problem, thus has served as the gold standard for validation of dose calculation algorithms for radiotherapy applications [22], [57], [58]. With recent advances in computer hard-

ware and computation methods, the computation time of MC simulations has been greatly reduced allowing their implementation in routine clinical treatment planning as part of plan verification [26], [105]. The dose distribution calculated via MC can be used to determine if plan parameters need to be altered in order to meet requirements prior to plan approval. MC provides a stochastic solution for the LBTE based on random number generators.

Random Number Generators

Computer generated random numbers cannot be truly random as they are produced deterministically, thus, pseudo-random numbers are used. Pseudo-random numbers appear to be random to someone who doesn't know the algorithm used to produce them. Certain criteria must be satisfied for a pseudo-random number generator (PNG) to be considered good. The PNG must produce a distribution of numbers that appears random and does not introduce correlations between successively generated numbers. It must have a long period—the length of a sequence after which the PNG will generate the same sequence of numbers. Also, a PNG should be able to repeat a sequence if required or produce a portion of a sequence. To test the quality and randomness of a PNG, several statistical tests have been employed including equidistribution, gap, run, permutation, serial correlation, spectral, and serial tests. These evaluate the uniformity of distribution, the correlation, and the independence of the sequence [109].

The two most common PNGs are multiplicative linear congruential generator (MLCG), and lagged Fibonacci generator (LFG). MLCG generates successive numbers by taking the first number, multiplying it by a constant, adding another constant, and throwing out the most significant digit. Mathematically, it is written in the form

$$s_i = (as_{i-1} + c) mod m \tag{2.14}$$

Where a and c are constants, s_i is the number generated, and m is the modulus. Typically, m is chosen to be in the form of 2^b, where b is the number of bits representing the number [109]. LFG produces the next number in a sequence by performing an addition or subtraction operation involving two prior numbers in the sequence. It can be written as

$$s_i = (s_{i-p} + s_{i-q}) mod m \tag{2.15}$$

Where s_i is the number generated, s_{i-p} and s_{i-q} are prior numbers in the sequence, and m is the modulus, also in the form 2^b [109]. These more basic PNGs have relatively short periods for an advanced radiotherapy MC calculation. More advanced algorithms with longer periods and better quality of randomness are used in radiotherapy MC these days including RANMAR and RANLAX, both of which are combinations of LFG and another PNG [71], [72].

Sampling methods

The above PNGs generate a uniform distribution of random numbers, however, in order to model a process with a probability density distribution, those random numbers need to be fit to that distribution. One of the methods to accomplish this is inverse transform method, displayed in Figure 2.15. Consider a variable x with a density function of p(x). Its cumulative distribution function is P(x). To determine x, its cumulative distribution function is inverted and sampled to produce x = $P^{-1}(u)$, where u is a random number on the uniform distribution of [0,1] [82], [28].

Alternatively, the acceptance/rejection method can be used. Consider a variable x with a density function p(x) and that there exists a density function q(x) such that m*q(x) $\geq$ p(x), where m is a constant. Obtain a random sample x_i from [x_{min}, x_{max}] and evaluate acceptance probability as $\alpha = p(x_i)/mq(x_i)$. Sample a random number u from uniform distribution of [0,1]. If $\alpha \geq$u, then accept x_i, otherwise, reject [106], [39]. This process is repeated many times to obtain a random numbers following the specified distribution p(x), see Figure 2.16.

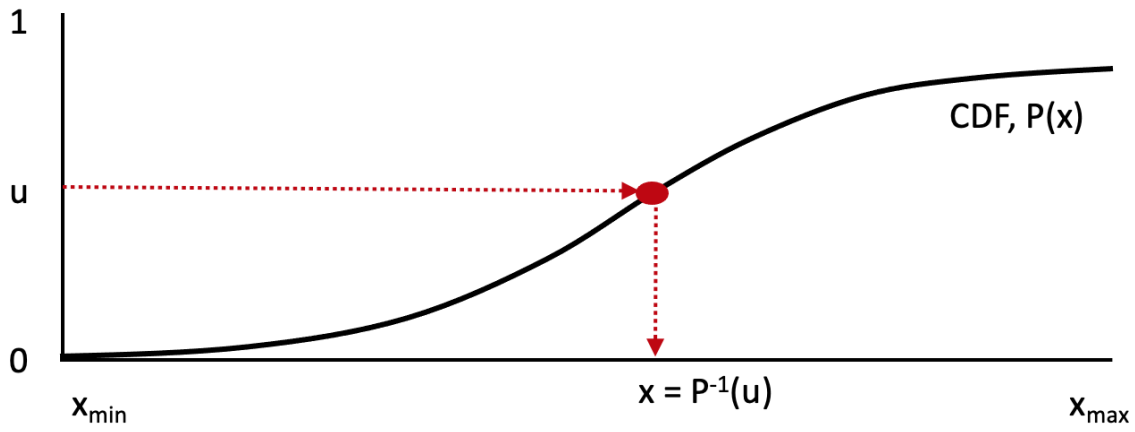

Figure 2.15: Illustration of inverse transform method.

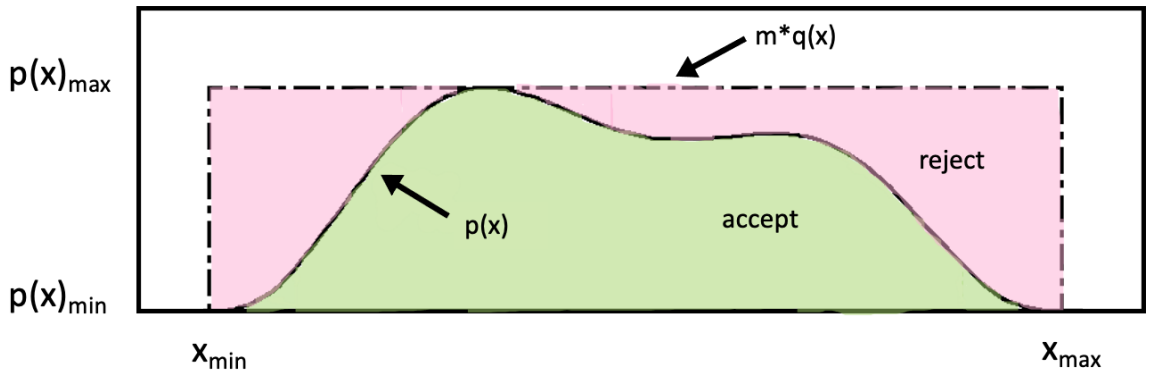

Figure 2.16: Illustration acceptance/rejection method illustration.

In the context of radiation therapy, interactions between primary or secondary photons and charged particles with the medium are governed by cross sections—or probability density distributions of said interactions. At an interaction point, MC randomly samples the probability density functions with the use of PNGs and sampling methods to determine the type of interaction. The energy loss, change in direction, and production of any secondary particles is recorded to be tracked in the next steps of the calculation. This continues until the energy of the particle is below a threshold, at which point its residual kinetic energy is locally deposited. This simulation process is repeated many times with a new starting particle selected from the phase space to be transported through the medium. The dose distribution is calculated by summing all of the energy depositions to individual volume elements.

VMC++

Several Monte Carlo codes have been developed for particle transport, the one used for research presented in this thesis was VMC++ developed by Iwan Kawrakow [59]. Voxel Monte Carlo (VMC) group of codes is specifically targeted towards radiation therapy taking into consideration only particles with energies in the range of 1 – 30 MeV and considers material densities in the range of 1 – 3 g/cm^3 [59].

Particle transport is modelled with condensed histories technique and simultaneous transport of particle sets (STOPS). Condensed histories technique allows the combination of several interactions by the same particle, which on their own wouldn't significantly alter the particle's energy or direction, into a single interaction, or step, with an estimated change in energy and direction of the particle. Interactions which create particles above a threshold energy are treated discretely, while those with en-

ergies below the threshold are treated with continuous slowing down approximation model and grouped into condensed history steps [59], [56]. VMC++ uses boundary crossing algorithm to eliminate the need for an interaction at the boundary between voxels extending the length of condensed history steps. This code selects the length of the step based on the electron-step algorithm taking into account the energy, voxel resolution, beam quality, cut-off energies, and materials. As a result, it is able to transport particles 5 to 30 times faster than other MC algorithms such as EGS4 or PRESTA [58]. STOPS is a variant of histories repetition technique where particles with the same energy are grouped to be transported simultaneously despite having different directions, positions, and weights. The interaction type is sampled for individual particles at each step. However, due to similarities of cross sections in materials relevant for radiotherapy, usually all particles have the same interaction type. When particles have differing interactions, the set is split into multiple sub-sets. STOPS allows to sample material independent variables like interpolated indexes, azimuthal angles, and mean free path once for the entire set instead of sampling these values for every particle reducing the calculation time by a factor of 2 [55].

Photon transport is broken down by interaction types. Creation of Bremsstrahlung photons are modelled with Bethe-Heitler cross sections. Compton scattering is modelled with Klein-Nishina cross sections. Pair production and photoelectric absorption is modelled based on cross sections from Evaluated Photo Data Library reported by Lawrence Livermore National Laboratory. Several methods are employed to reduce the computation time, mainly photon splitting, Russian roulette, and use of quasi random numbers, resulting in reduction of computation time by a factor of 5-10 [57]. Photon splitting is when all incident photons are split into n sub-photons each with a weight of 1/n creating a photon set. The mean free paths of these photons are sampled using quasi random numbers and subsequent interaction sites are sampled based on these paths to the entire set of incident photons. Additionally, assuming that differential cross sections are independent of the medium/energy of interest in radiotherapy, the same cross sections are used for all interaction sites instead of sampling cross sections per site, thus allowing the transport of photon sets similar to the STOPS technique for electron transport. Russian roulette reduces the number of scattered photons transported by eliminating photons based on weighting. Quasi random numbers based on well-known sequences, such as Sobel's sequence, are used in place of pseudo random numbers to increase integration efficiency of calculation. All of these techniques reduce statistical noise of MC, thereby reducing computation

time as fewer particle histories are needed. This is called variance reduction [57].

Particle interactions are determined based on cross sections, where each interaction is treated as a separate object. Each object calculates the total cross section and moments of the cross section (stopping power, energy absorption coefficients), and samples the change in energy and direction [58].

In order to calculate dose to a medium other than water, a ramp function of CT numbers from 16 materials commonly found in the body is used. The ramp function is binned such that linear mass attenuation coefficients and mass stopping power of all materials differ by less than 1% [58].

In summary, VMC++ is a MC simulation of coupled photon-electron transport optimized for treatment planning dose calculation for radiotherapy applications. Due to all of the variance reduction techniques employed, VMC++ is one of the fastest and most accurate MC codes for particle transport and dose calculation currently available.

VIMC software and models

Monte Carlo calculations that are presented in this work were performed using Vancouver Island Monte Carlo (VIMC) system [24]. VIMC allows calculations of patient dose using VMC++ codes to transport particles through a phantom. As a radiation source, it used phase spaces provided by Varian for TrueBeam linacs, and it allows selection of jaw and MLC models (rigorous vs fast models). This work used a combination of fast dose calculation code (VMC++) as well as fast jaw and MLC models. MLC model was developed by Keall [60] and Siebers [92], and jaw model was developed and reported by Townson [99]. The reason for using combination of fast codes was to save time, as a large number of plans had to be calculated in the course of this project, and this work also provided extra benchmarking for the MC calculations that are in clinical use at Vancouver Island Centre.

Jaws are modelled as flat perfectly absorbing planes. If a particle passes through the opening, it goes on to further steps of the simulation. If a particle interacts with the jaws, it gets removed from the simulation. This fast jaw model is coupled to the MLC model to allow the motion of the secondary collimator to be linked to the MLCs through control points which contain positional information for the jaws and MLC leaves, and the fractional delivered monitor units. For each particle read from the phase space file, the fractional delivered monitor units are randomly sampled via

MC methods to determine the geometry of jaws and MLC through which the particle will be transported [99]. The geometry of MLC is modelled with more detail [92]. The basic premise is that particle weighting is modified based on probability of transmission (from the initial phase space file stored after transport through the linac head components to the phase space file stored after passage through the jaws and MLC). This model accounts for charged particle interactions by randomly generating Compton electrons. The main interaction type with tungsten in the 0.5-5 MeV region is Compton. The thickness of material a particle passes through is determined by tracking its X,Y coordinates as it enters and exits the MLC leaf regions (MLC thickness is split into several regions). The weighting of the particle is altered at that point based on exponential attenuation. The Compton interaction probabilities are evaluated based on Compton attenuation coefficient over the total attenuation coefficient. The location of interaction is randomly sampled from 0 to t, where t is the thickness of material a particle traverses. The energy and polar angle (relative to the primary particle) of the scattered photon are determined using the method described in the EGS4 Manual [78]. The azimuthal angle of the scattered photon is randomly sampled from 0 to 2π. The pathlength and attenuation coefficient of the scattered photon are determined using the above information and a weighting is assigned.

2.9 Gamma Analysis Techniques

The gamma index (γ), as first introduced by Low et al. [66], provides a single metric for comparison of dose distributions, particularly useful for the verification of complex radiotherapy delivery techniques such as VMAT. γ takes into account dose difference and distance to agreement criteria based on pass-fail rates to compare two dose distributions—reference dose distribution (usually measured) and evaluated dose distribution (usually TPS predicted).

Van Dyk et al. [102] proposed directly comparing dose distributions in low and high dose gradient regions. Low dose gradient regions have an acceptance tolerance placed on the difference between measured and calculated doses, and a dose-difference distribution is displayed highlighting areas of disagreement. Dose differences in high dose gradient regions are subject to large disagreement due to small spatial errors, thus distance to agreement is used instead. Distance to agreement is the distance between a point in the reference dose distribution and the nearest point in the evaluated dose distribution which has the same dose.

Low et al. [66], simultaneously consider both criteria by forming an ellipsoid around the point of interest in the reference dose distribution with surface dimensions governed by the selected acceptance criteria (see Figure 2.17). The 'width' of the ellipsoid represents the distance to agreement criteria, $\triangle d_M^2$, and the 'height' of the ellipsoid represents the dose agreement criteria, $\triangle D_M^2$. The mathematical representation of the surface is then given by

$$1 = \sqrt{\frac{r^2(r_m, r)}{\triangle d_M^2} + \frac{\delta^2(r_m, r)}{\triangle D_M^2}} \tag{2.16}$$

where

$$r(r_m, r) = |r - r_m| \tag{2.17}$$

$$\delta(r_m, r) = D(r) - D_m(r_m) \tag{2.18}$$

Points in the evaluated dose distribution plane are compared against the surface of the ellipsoid, if any intersect the surface, then the calculated dose passes at r_m. The equation describing the ellipsoid surface can be used to calculate γ as follows

$$\gamma(r_m) = min\Gamma(r_m, r_c)\forall r_c \tag{2.19}$$

where

$$\Gamma(r_m, r_c) = \sqrt{\frac{r^2(r_m, r)}{\triangle d_M^2} + \frac{\delta^2(r_m, r)}{\triangle D_M^2}} \tag{2.20}$$

$$r(r_m, r_c) = |r_c - r_m| \tag{2.21}$$

$$\gamma(r_m, r_c) = D_c(r_c) - D_m r_m \tag{2.22}$$

$\gamma(r_m, r_c)$ is the difference between the calculated and measured dose distributions. Gamma pass/fail criteria is as follows

$$\gamma(r_m) \leq 1, pass \tag{2.23}$$

$$\gamma(r_m) > 1, fail \tag{2.24}$$

and an overall gamma pass rate can be assigned to the whole dose distribution.

Commonly, a lower dose threshold is set for which gamma results are ignored in order to avoid high noise regions or out-of-field regions which can skew γ results. This threshold is usually set at 10% of the maximum dose [2].

One main point of confusion in literature regarding reported γ index values is lack of clarity as to whether local or global γ values are reported. The difference being in the way dose difference is calculated. Local γ calculates the percent differences relative to the dose at each point as defined by the above equations, and tends to exaggerate differences in low dose regions and high dose gradient regions. Global γ calculates the percent difference relative to the maximum dose, typically the prescription dose. In order to accomplish this, the dose difference equation needs to be modified to include normalization—usually to the maximum dose, but any dose value can be chosen [66]. It can now be written as

$$\delta(r_m, r_c) = \frac{D_c(r_c) - D_m(r_m)}{D_{norm}} \tag{2.25}$$

Global γ highlights the dose differences in high dose regions [49], which is most useful in the scope of this thesis. Additionally, We need to know whether the dose to the tumour is within acceptable tolerance for a plan to be considered successfully planned and delivered, while low dose regions hold much less significance. As such, the threshold dose, ie. the lowest dose considered for the analysis, was chosen at 80% to evaluate clinically relevant dose regions. Threshold of 10% (to eliminate the noise floor) was also evaluated for sake of completeness as many publications report 10% threshold for gamma analysis.

Currently, there are no clear guidelines or standards for gamma analysis parameters for detecting errors in clinical VMAT plans. Heilemann et al. [46] demonstrated that 2%/2mm gamma passing rates over 90% are sufficient to pin point VMAT plans with deliberately introduced MLC errors. Here, at BC Cancer Victoria, the current practice is 3%/1.25mm, 5%/1mm, or 3%/1mm for patient quality assurance of SRT/SRS treatment plans. Since this thesis focuses on SRS/SRT applications, the distance tolerance was chosen at 1 mm following clinical protocol, and the dose percent difference was chosen as 3%.

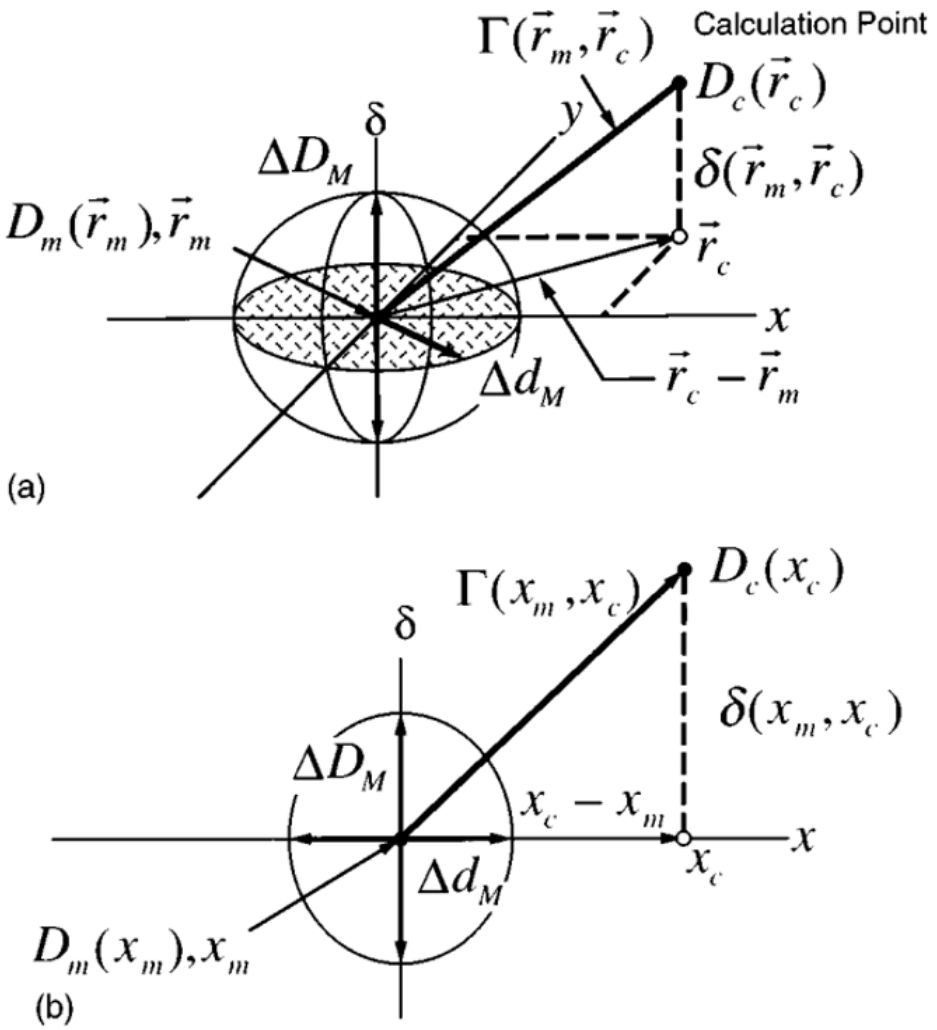

Figure 2.17: Visual representation of combined dose difference and distance to agreement criteria in 1D (bottom) and 2D (top). [66].

Chapter 3

Characterization of a 0.8 mm^3 Medscint plastic scintillator detector system for small field dosimetry

3.1 Introduction

Modern radiation therapy sees increased use of small fields for treatment of tumours through advances in highly specialized techniques such as intensity modulated radiotherapy (IMRT), volumetric-modulated arc therapy (VMAT), stereotactic radiosurgery (SRS), stereotactic radiotherapy (SRT), and stereotactic ablative radiotherapy (SABR). These treatments can be delivered using a linear accelerator equipped with mini-, micro-, or high definition (HD) multi-leaf collimators (MLCs). Most treatments are performed in 6-10 MV energy range, for example SABR for lung cancer uses 6 MV beams and 10 MV in 96% and 3% of all cases, respectively [83]. Since small fields are more and more common, small field dosimetry becomes increasingly important.

The main detector-related challenges in small field dosimetry are fluence perturbation effects, principally caused by material and density differences between detector material and water [21], as well as volume averaging effects and detector positioning difficulties. To overcome these challenges, the ideal small field detector samples fluence at a point (to reduce volume averaging effects and provide high spatial res-

olution), is water equivalent (to remove fluence perturbation effects), offers linear response with dose, is independent of dose rate, energy, and direction of irradiation (to eliminate correction factors) [50]. Additionally, water resistance and direct-real-time readout are beneficial for ease of use.

Beddar et al. [13], [14], showed that plastic scintillators are water equivalent, are independent of energy, dose and dose rate, boast a fast response time, can be manufactured to small sizes (sub-mm), and exhibit less radiation damage effects than other detectors such as diodes. Continued research and development efforts over the last 30 years have led to further developments in scintillator detectors such as an ability to subtract Cherenkov light produced in optical transmission fibers [40], [44], improved cladding for enhanced internal total reflection that minimizes loss of signal [7], and multipoint readouts [97] allowing dosimetry in diverse and challenging conditions, including small fields.

The novel HYPERSCINT RP-200 (HS RP-200) plastic scintillator detector (PSD) dosimetry system, developed by Medscint Inc. (Quebec, QC., Canada), optimizes light collected from PSDs and optical fibers for the purpose of scintillation dosimetry, offering accurate and non-perturbating measurements for small field dosimetry applications. Additionally, this system automatically separates the stem effects via chromatic removal through the implementation of a hyperspectral approach [97]. The stem effect removal accounts for fluorescence and Cherenkov signal generation in the optical cable as well as the fiber spectral attenuation, which have a different spectral signature compared to the scintillator signal. Furthermore, Medscint Inc. offers customizable PSD probe designs in sub-millimetric sizes.

Previously, the HS RP-100 dosimetry system—another system by Medscint Inc., with a 3-point PSD probe was evaluated by Jean et al. [52] for dosimetric performance. Through their work, a linear response was established in the range of doses from 1 cGy to 600 cGy. It was shown that depth dose to 200 mm and full-width-half-max of lateral dose profiles can be measured within 1.1% and 2.3% accuracy, respectively. Also, output factors were measured for field sizes from 15 x 15 cm^2 down to 2 x 2 cm^2 with a maximum difference of 1.78% compared to ion chamber output factor measurements. In 2022, Shoepper et al. [90] used the same dosimetry system, but with a 1 mm x 3 mm PSD probe to show response linearity with dose (1 to 1000 MU), as well as dose rate (100 to 600 cGy/min) and field size (30 x30 cm^2 to 3 x 3 cm^2) independence. They measured depth dose down to 15 cm within 1.14% accuracy and demonstrated minimal angular dependence.

The most comparable detector out on the market is the Exradin W2 (Standard Imaging Inc., Middleton, WI). It is a 1 mm x 1 mm PSD probe featuring water equivalency, independence from temperature, dose rate, and energy, and it comes with Cherenkov correction as well, through the SuperMAX electrometer. This detector has been well documented, and has been shown to be dosimetrically similar to Exradin W1, another PSD by Standard Imaging Inc (3 mm length by 1 mm diameter) [42].

Although PSDs and scintillator signal acquisition systems, similar to HYPERSCINT RP-200, have been reported in literature [42], [52], [90] , to our knowledge, there are no publications showing the characteristics of the HS RP-200 dosimetry system coupled to a small 0.8 mm^3 PSD probe. In this study, a full characterization, in the clinical setting, of this dosimetry system was performed. The system was evaluated with respect to fundamental dosimetric properties including leakage, short-term repeatability, dose-response linearity, dose rate dependence, field size dependence, and angular dependence. Additionally, relative output factors were measured down to field sizes of 0.25 x 0.25 cm^2, and small field output correction factors were evaluated for 6 MV and 10 MV-FFF beams.

3.2 Methods

3.2.1 Dosimetry System Description

The HYPERSCINT RP-200 (HS RP-200) dosimetry system consists of three parts i) plastic scintillator detector probe, ii) acquisition system, and iii) software. The probe investigated in this work is a single-point, polyvinyltoluene detector, which has a sensitive volume of 0.8 mm^3 given by it diameter of 1 mm and length of 1 mm. This probe is housed in a black nylon envelop and is optically coupled to a 20-m long 1-mm diameter PMMA optical fiber core clad in a polyethylene jacket. The fiber optical cable is attached to the HS RP-200 acquisition system with a proprietary connector. The signal is read out using Medscint's proprietary software. For the remainder of this thesis, this particular set up consisting of the above mentioned probe, acquisition system, and software will be referred to as HS RP-200-1x1.

3.2.2 Measurements

First, using a Varian TrueBeam STx linac, a four-component calibration procedure specified by Medscint, including scintillation, fluorescence, Cherenkov, and optical fiber spectral attenuation was performed. The scintillation and flourescence components were obtained by performing a high intensity kV beam irradiation of only the probe end, followed by irradiation of only the optical fiber, for 60 seconds and 120 seconds respectively. The Cherenkov calibration and fiber spectral attenuation consisted of four components, and included irradiating two sections of optical fiber laying perpendicularly to the beam at isocenter with gantry angles of 45 and 315 degrees. Finally the dose calibration was performed by irradiating the probe to a known dose. An integration time of 1 second was used for all measurements.

Most irradiations were performed with a Varian TrueBeam STx linear accelerator (Varian Medical Systems, Palo Alto, CA) equipped with an HD-MLC with 2.5 mm leaves under a 6 MV beam with a dose rate 600 MU/min or 10 MV-FFF beam with a dose rate 2400 MU/min. Some irradiations were performed with Varian TrueBeam equipped with mellenium MLC. In dose rate dependence measurements, the dose rate was varied. Excluding angular dependence measurements, the PSD probe was placed at SSD = 100 cm perpendicularly to the beam at a depth of 10 cm in a solid water phantom (Gammex-RMI Ltd., Nottingham, UK, model 457-320) with 10 cm of solid water as backscatter to provide reference conditions. The probe was connected to the HS RP-200 signal acquisition system, which was placed outside the linac bunker. The measurements were repeated on several separate occasions spanning over eight weeks to account for any potential setup and linac output variations.

Pre/post irradiation leakage

In order to determine leakage, dark current readings were taken prior to and post irradiation. An increased dose reading immediately post irradiation compared to one minute post irradiation would indicate leakage. Under the reference conditions mentioned above, a ten minute measurement was performed pre-irradiation. Next, 500 MUs were delivered to the PSD under a 10 x 10 cm^2 field size, and a five-second measurement was taken immediately afterward. Following a 60 second delay post 500 MUs irradiation, another five-second leakage measurement was taken.

Short term repeatability

Short term repeatability was obtained by irradiating the PSD 10 times in the reference conditions. Each irradiation delivered 200 MUs with a 5 x 5 cm^2 field size. Comparison of individual readings to the average was used to determine the short term repeatability.

Dose-response linearity

The relationship between dose measured by the PSD and the dose delivered was obtained by successively delivering varying dose to the PSD from 5 up to 2000 MUs, in reference conditions with a 5 x 5 cm^2 field size. The dose readings were plotted against monitor units delivered to check for linear relationship. Linac output linearity was checked using Farmer chamber and confirmed to be within 0.3% down to 5 MU and to within 2% down to 1 MU.

Dose rate dependence

The PSD response to dose rate was measured using linac defined dose rates ranging from 100 MU/min to 2400 MU/min. More specifically, the 6 MV beam delivered dose rates of 100-600 MU/min and the 10 MV-FFF beam delivered dose rates of 400-2400 MU/min. Under reference conditions, with a 5 x 5 cm^2 field size, 200 MUs were delivered. The dose measured was normalized to 6 MV 600 MU/min readings and then directly compared against all other dose rate readings.

Field size dependence (Output Factors)

Field Size Specification

Following the IAEA TRS-483 guidelines [50], field size was defined as the full-width-half-max (FWHM) of in-plane and cross-plane profiles of the field at the position of the detector. Then, equivalent square field size S_{clin} was calculated as follows

$$S_{clin} = \sqrt{a * b} \tag{3.1}$$

where a is the length and b is the width of a rectangular field defined by the FWHM in-plane and cross-plane dosimetric profiles. Lateral beam profiles were measured using RTQA2 Gafchromic film (Ashland Advanced Materials, Bridgewater, NJ). The field size was MLC defined with jaws set a few millimeters outside MLC dimensions,

as specified in Table 1, to reduce jaw aperture uncertainties [30]. Setup for fields larger than 1x1 cm^2, inclusive, reproduced setup by Bassinet et al. [12] In that study Bassinet et al., using a Clinac 2100, measured field output factors for active and passive detectors including shielded and unshielded diodes, LiF microcubes, films, ion chambers and microDiamond.

Table 3.1: Field sizes defined via nominal dimensions as given by combination of MLC and jaw positions, and equivalent field size as defined by FWHM of the in-plane and cross-plane profiles obtained from Gafchromic film.

MLC Size (cm^2)	Jaw Size (cm^2)	FWHM Equivalent Square (cm)
0.25x0.25	1x1	0.28
0.5x0.25	1x1	0.33
0.5x0.5	1x1	0.53
0.75x0.75	1x1	0.74
1x1	1.2x1.2	0.96
1.25x1.25	1.4x1.4	1.16
1.5x1.5	1.7x1.7	1.44
1.75x1.75	2x2	1.67
2x2	4.4x4.4	1.98
2.5x2.5	4.4x4.4	2.45
3x3	4.4x4.4	2.99
5x5	5x5	4.99
10x10	10x10	9.99

Field Output Factors

IAEA TRS-483 [50] adopts the formalism by Alfonso et al. [5] and defines field output factors as the absorbed dose for a small field, f_{clin}, relative to the absorbed dose in a machine specific reference field, f_{msr}, as

$$\Omega_{Q_{clin},Q_{msr}}^{f_{clin},f_{msr}} = \frac{M_{Q_{clin}}^{f_{clin}}}{M_{Q_{msr}}^{f_{msr}}} * k_{Q_{clin},Q_{msr}}^{f_{clin},f_{msr}} \tag{3.2}$$

where $M_{Q_{clin}}^{f_{clin}}$ is the detector reading in the small field, $M_{Q_{msr}}^{f_{msr}}$ is the detector reading in the machine specific reference field, and $k_{Q_{clin},Q_{msr}}^{f_{clin},f_{msr}}$ is the small field correction factor. $\frac{M_{Q_{clin}}^{f_{clin}}}{M_{Q_{msr}}^{f_{msr}}}$ is defined as relative output factor.

In this work relative output factors were measured with the HS RP-200-1x1 system and then $k_{Q_{clin},Q_{msr}}^{f_{clin},f_{msr}}$ factors were derived from comparison of these results with

the literature, where field output factors were published for the same fields.

PSD Positioning

The effective point of measurement, as indicated on the probe at 2.5 mm from the tip, was placed at the center of the smallest linac-defined field (0.25 x 0.25 cm^2) by means of in-plane and cross-plane profile measurements. The detector was placed at the position which gave the maximum reading in each direction.

Measuring Output Factors

Under reference conditions, the PSD was irradiated to 100 MU per field size for field sizes of 0.25 x 0.25 cm^2 to 10 x 10 cm^2 as outlined in Table 1. Relative output factors for a specific field size were defined as the ratio of the dose measured at that field size to the dose measured at a field size of 10 x 10 cm^2 (machine specific reference field). These output factors were then compared with measurements performed using a PTW60019 microDiamond (PTW, Freiburg, Germany) corrected with small field correction factor following IAEA TRS-483 under the same irradiation conditions. The measured values were compared to published data.

Angular dependence

Since the PSD is cylindrical, no angular dependence in this direction is expected. To confirm this, the PSD was placed in the center of a plastic-shell 20-cm diameter cylindrical phantom filled with water that was positioned at the isocenter of the linac. Iso-centric position of the water phantom was verified using cone beam CT (CBCT) imaging. The PSD was irradiated with 200 MU and a 5 x 5 cm^2 field size at gantry angles from 0°to 340°in 20°increments. Relative comparison of dose readings for each gantry angle was calculated with respect to the reading at 0°angle.

3.3 Results

3.3.1 Pre/post irradiation leakage and short term repeatability

A 10 minute measurement under no irradiation of the PSD yielded a reading of 1.45 cGy. Post irradiation readings indicated minimal leakage. The 5 second reading immediately post 500 MU irradiation (time = 0 sec post irradiation) was 0.017 cGy and the 5 second reading one minute post irradiation was 0.021 cGy (time = 60 sec post irradiation), both well below the background reading.

The average of 10 readings taken for 200 MUs delivered per measurement with 5 x 5 cm^2 field size was 113.33 cGy with a standard deviation of 0.044 $\pm$ 0.007%.

3.3.2 Dose-response linearity

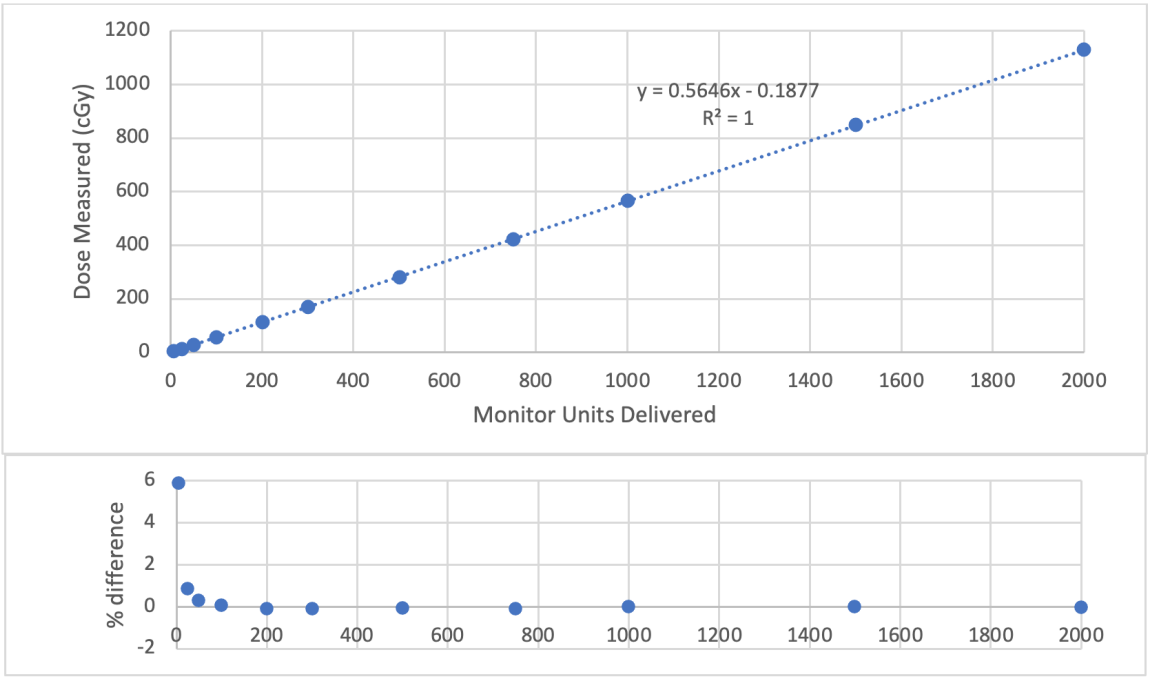

Figure 3.1: Dose linearity of HS RP-200 (including 1 mm x 1 mm cylindrical PSD, HYPERSCINT signal acquisition system, and HYPERDOSE analysis software). Subplot shows the percent deviation of the measured dose from the dose expected from the linear fit.

Dose-response of this dosimetry system showed a linear relationship with an R^2 value of 1 (0.9999996) and standard error of fit 0.26 cGy (Figure 3.1). However, for

the lowest delivered dose of 5 MU, the deviation of the measured from the expected linear dose response was 5.9%. Otherwise, differences fell below ± 1% for doses higher than 25 MU. At the measurement point in this setup 1 MU = 0.574 cGy.

3.3.3 Dose rate response

The HS RP-200-1x1 showed no dose rate dependence between 100 MU/min and 2400 MU/min. The PSD measured constant dose with largest discrepancy of 0.48% at dose rate of 100 MU/min, otherwise discrepancy was within 0.10% (Figure 3.2). For dose rates below 100 MU/min, the discrepancy increased up to 1.56% at the lowest dose rate measured (40 MU/min).

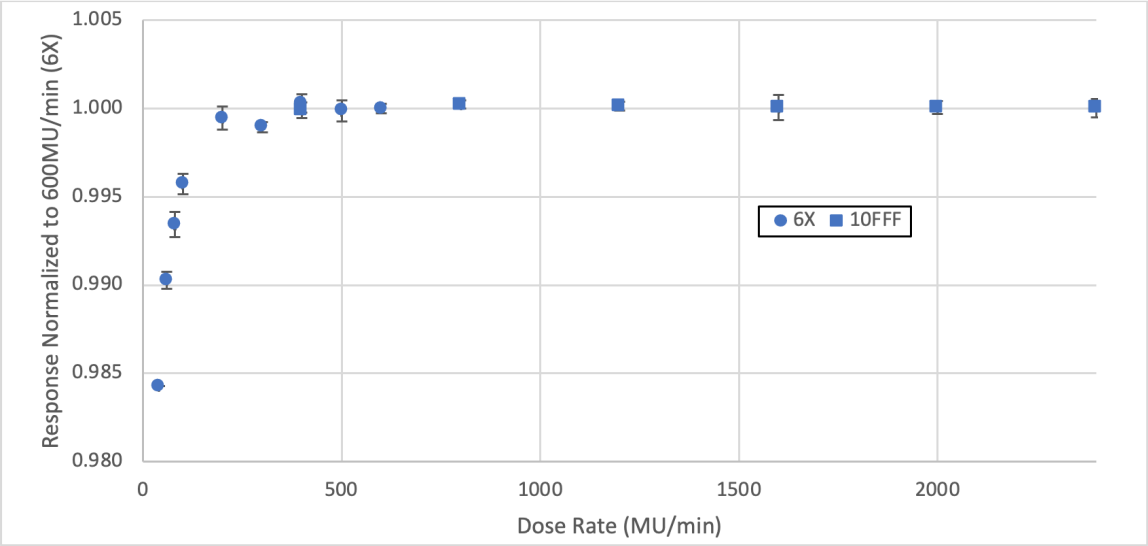

Figure 3.2: Dose rate response of HS RP-200 (including 1 mm x 1 mm cylindrical PSD, HYPERSCINT signal acquisition system, and HYPERDOSE analysis software). The response is normalized to 600 MU/min delivered with 6 MV energy beam. Circles are 6 MV energy beam. Squares are 10 MV-FFF energy beam.

3.3.4 Field size dependence (Relative output factors)

6 MV beams

Figure 3.3 displays relative output factors measured HS RP-200-1x1 for 6 MV energy beams from Varian Truebeam STx and Varian TrueBeam for field sizes of 0.25 x 0.25 cm^2 to 10 x 10 cm^2 and 0.5 x 0.5 cm^2 to 10 x 10 cm^2, respectively. This figure also includes corrected field output factors measured with PTW60019 microDiamond

detector and data from Lechner et al. [64] for field sizes of 0.5 x 0.5 cm^2 to 10 x 10 cm^2. For Varian TrueBeam STx and field sizes above 1 x 1 cm^2, inclusive, the agreement between HS RP-200-1x1 and microDiamond was within 1.5%. For field size of 0.5 x 0.5 cm^2 the relative output factors measured with HS RP-200-1x1 were 3.0% lower than field output factors measured with microDiamond detector. Field output factors for field sizes smaller than 0.5 x 0.5 cm^2 were not measured with microDiamond because published small field correction factors for these field sizes have large reported uncertainties [6]. Relative output factors measured with HS RP-200-1x1 on Varian TrueBeam and Varian TrueBeam STx agreed to within 1.9% for field sizes down to 0.5 x 0.5 cm^2. For the field sizes down to 0.6 x 0.6 cm^2, comparison of these relative output factors to the output factors reported by Lechner et. al. for Varian TrueBeam STx showed agreement within 1.4%. However, comparison to Lechner data for Varian TrueBeam showed a difference of about 45% for the smallest field size of 0.5 x 0.5 cm^2.

In Figure 3.4, the relative output factors measured with HS RP-200-1x1 are compared to field output factors measured by Bassinet et al. [12] using a Clinac 2100. Bassinet et al. measured field output factors for active and passive detectors including shielded and unshielded diodes, LiF microcubes, films, ion chambers and microDiamond. For field sizes above 1 x 1 cm^2 the measured output factors agreed with Bassinet within 0.5%. However, the field output factor for the smallest field size of 0.6 x 0.6 cm^2 reported by Bassinet was 2.1% higher than the HS RP-200-1x1 output factor.

10 MV-FFF beams

Figure 3.5 displays the relative output factors for 10 MV-FFF beams from Varian TrueBeam (field size 0.5 x 0.5 cm^2 to 10 x 10 cm^2) and Varian TrueBeam STx (field size 0.25 x 0.25 cm^2 to 10 x 10 cm^2) that were measured using HS RP-200-1x1. These are compared against corrected field output factors measured with PTW60019 microDiamond detector and against data from Lechner et al. [64] that were obtained with IBA EFD3G and PTW60017 unshielded diodes. Values of field output factors measured with microDiamond were only included down to 0.5 x 0.5 cm^2 because small field correction factors have large uncertainties for smaller field sizes. For Varian TrueBeam STx, the HS RP-200-1x1 relative output factors and microDiamond field output factors for field sizes 2 x 2 cm^2 and larger agreed to within 1.5% where HS RP-200-1x1 measured lower. At 1 x 1 ^{2} a difference of 3.8% was seen, and for field size

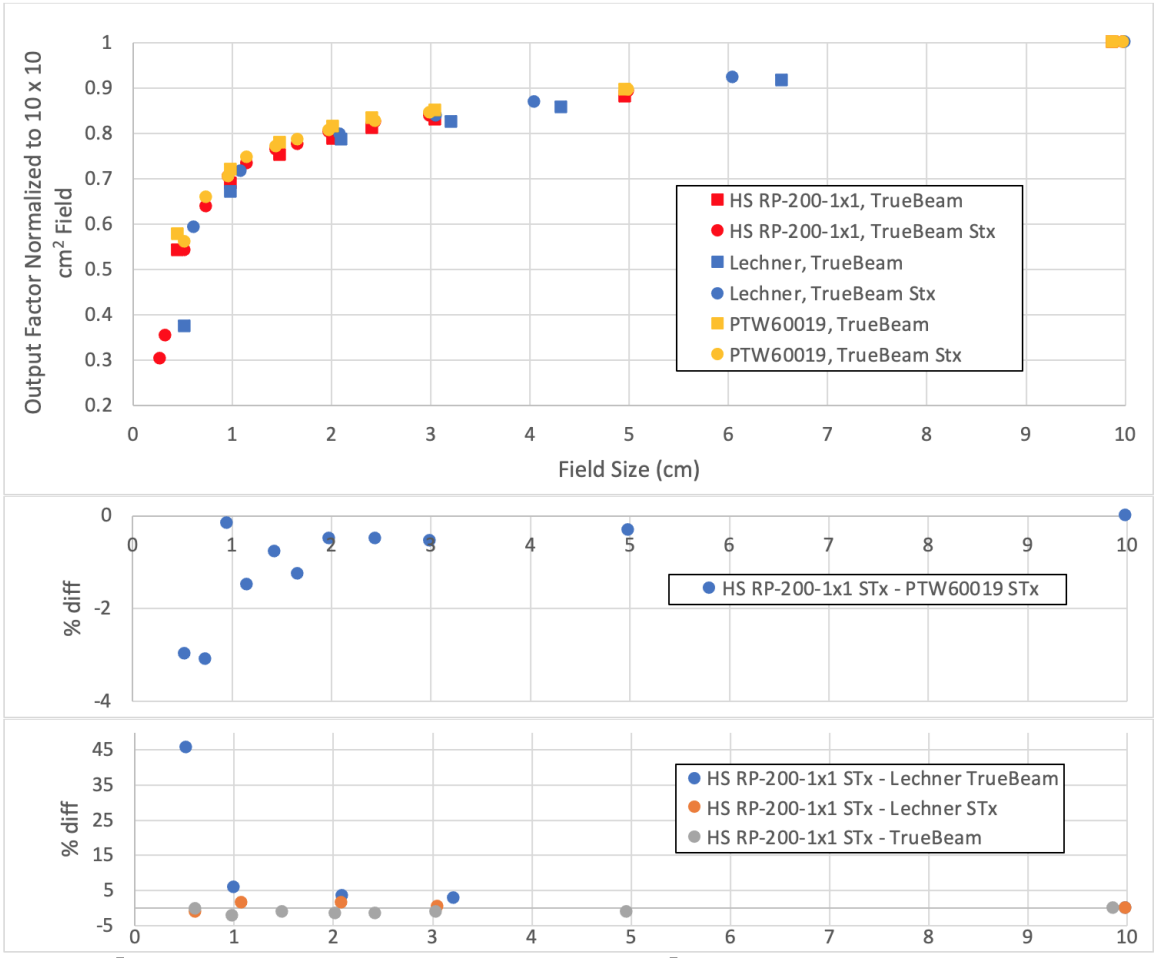

Figure 3.3: Relative output factors for 6 MV energy beam and field sizes ranging from 0.25 x 0.25 ^{2} to 10 x10 ^{2}, measured with HS RP-200-1x1, are compared to output factors for field sizes ranging from 0.5 x 0.5 ^{2} to 10 x10 ^{2} measured with PTW60019 microDiamond detector. Measurements were performed on Varian TrueBeam STx with 2.5 mm HD-MLC leaves as well as on Varian TrueBeam (MLC leaves 5 mm). Also included are output factor data from Lechner et al. [64]. Subplot shows the percent difference between HS RP-200-1x1 measured on Varian TrueBeam and Varian TrueBeam STx as well as the difference to the Lechner datasets.

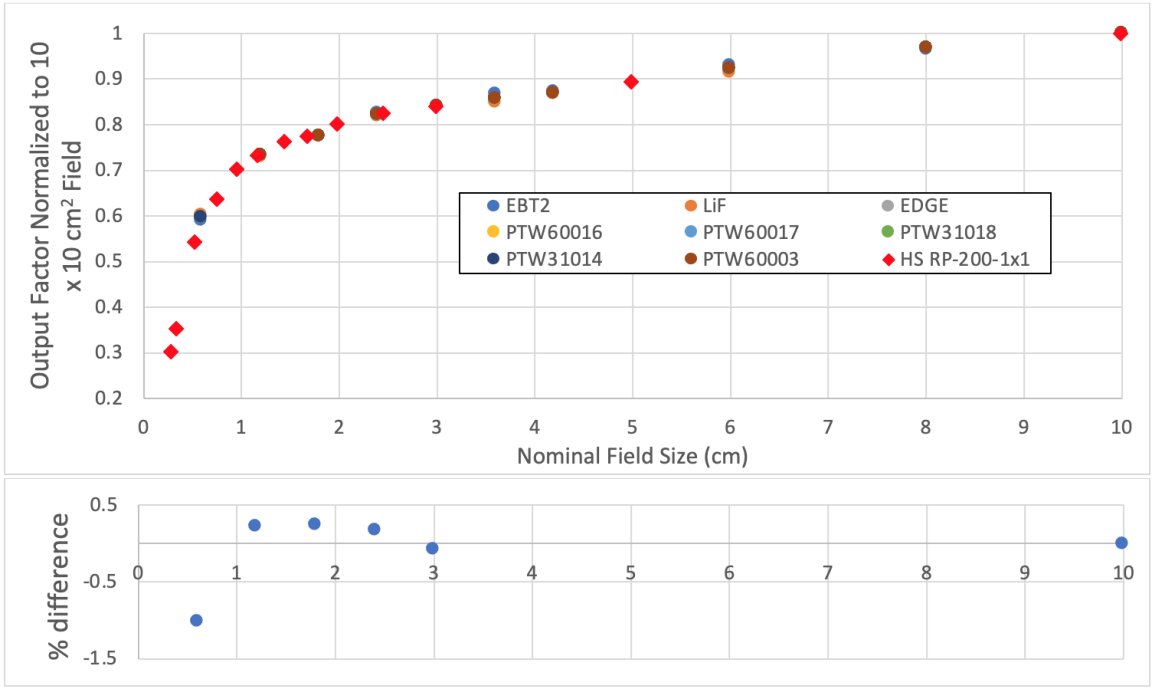

Figure 3.4: Relative output factors for 6 MV energy beam and field sizes ranging from 0.25 x 0.25 cm^2 to 10 x 10 cm^2 measured with HS RP-200-1x1 detector on Varian TrueBeam STx linac equipped with 2.5 mm HD-MLC leaves. Also plotted are field output factors determined by Bassinet et al. [12]. Subplot indicates the percent difference between extrapolated HS RP-200-1x1 relative output factors and the average value of field output factors from Bassinet.

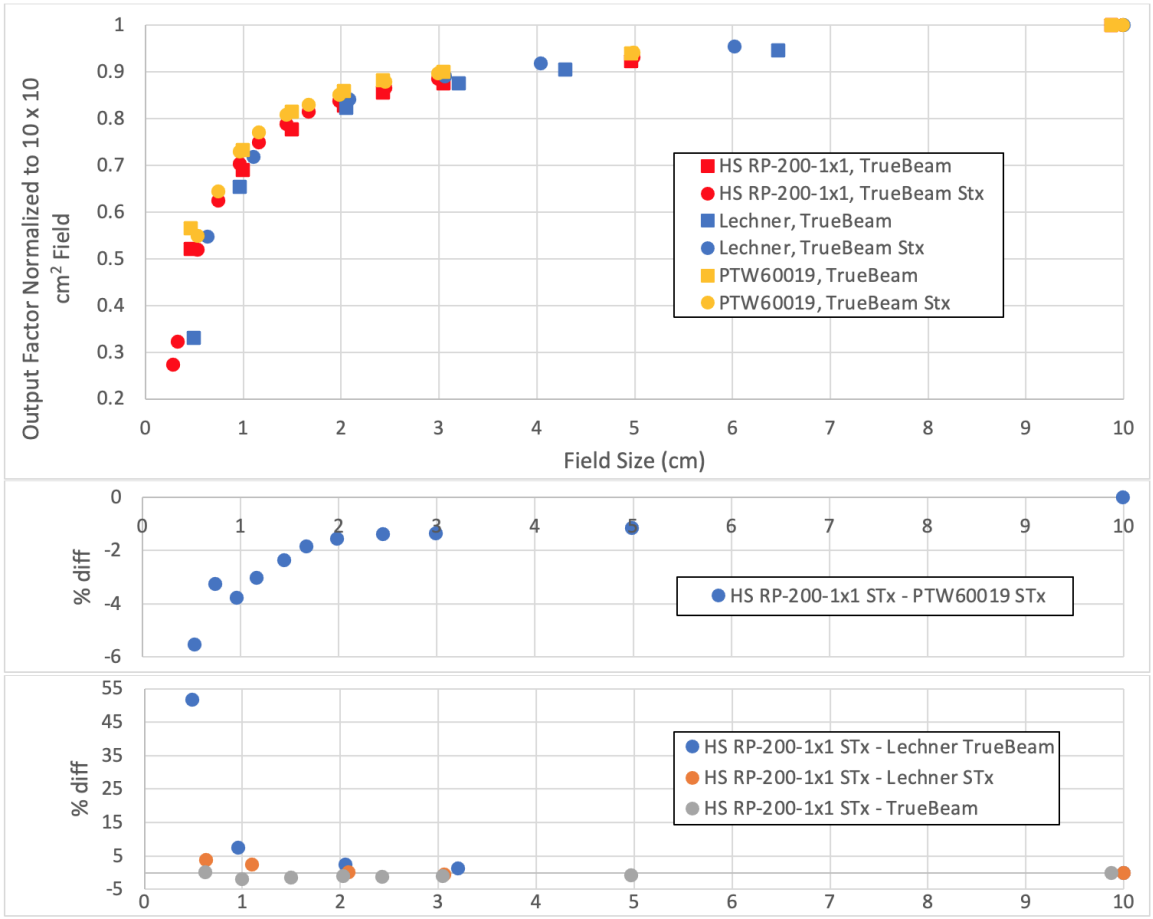

Figure 3.5: Relative output factors for 10 MV-FFF energy beam and field sizes ranging from 0.25 x 0.25 cm^2 to 10 x 10 cm^2, measured with HS RP-200-1x1, are compared to field output factors for field sizes ranging from 0.5 x 0.5 cm^2 to 10 x 10 cm^2 measured with PTW60019 microDiamond detector. Measurements were performed on Varian TrueBeam STx with 2.5 mm HD-MLC leaves as well as on Varian TrueBeam (5 mm MLC leaves). Also included are output factor data from Lechner et al. [64]. Subplot shows the percent difference between HS RP-200-1x1 measured on Varian TrueBeam and Varian TrueBeam STx as well as the difference to the Lechner datasets.

of 0.5 x 0.5 cm^2 a difference of 5.5% was seen, again with HS RP-200-1x1 measuring lower. Comparison to the Varian TrueBeam STx dataset from Lechner et. al. showed that relative output factors measured with HS RP-200-1x1 and field output factors measured with PTW60017 unshielded diode agreed within 0.6% for field sizes 2 x 2 cm^2 and larger. For 1 x 1 ^{2} field size, HS RP-200-1x1 relative output factor was 2.4% higher and for 0.6 x 0.6 cm^2 field size the HS RP-200-1x1 relative output factor was 3.9% higher than output factors reported by Lechner. Comparison to the Varian TrueBeam dataset measured with IBA EFD3G unshielded diode from Lechner showed a difference of up to 51% for the smallest field size of 0.5 x 0.5 cm^2.

3.3.5 Angular dependence

The angular dependence, relative to gantry at 0°, of the investigated PSD is shown in Figure 3.6. The angular dependence was mostly below 0.1%, and the maximum angular dependence was 0.15% ± 0.01% at a gantry angle of 260°.

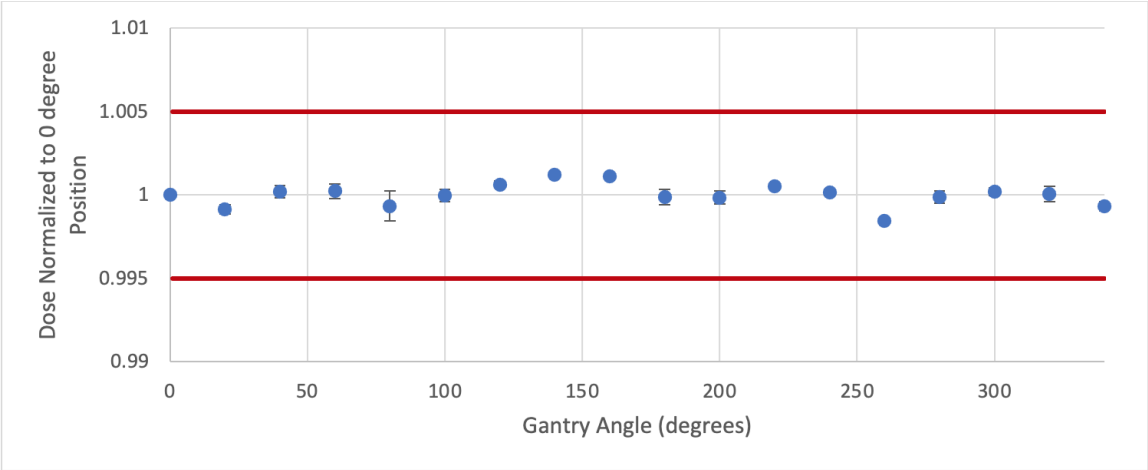

Figure 3.6: Angular dependence, normalized to gantry at 0°, of the 1 mm x 1 mm cylindrical PSD. Red lines indicate 0.5% difference.

3.4 Discussion

3.4.1 Pre/post irradiation leakage and short term repeatability

A dose of 1.45 cGy was recorded over a pre-irradiation measurement spanning 10 minutes. This is quite interesting considering that part of the calibration procedure was to perform a background reading which is be subtracted from future measurements. It is therefore expected that a background reading with a correct calibration should be zero. However, the average length of an SRS/SRT treatment at our institution is well below 10 minutes. Considering an average dose per fraction of 11.7 Gy [1], the 1.45 cGy dark current is about 0.1% of the average dose delivered, and can be considered clinically insignificant. Readings taken immediately prior to and immediately after irradiation indicated no leakage as all values were comparable to expected background levels.

The short term repeatability of HS RP-200-1x1 that was quantified through the standard deviation of 10 readings was 0.044± 0.007%. This is better than repeatability measured by Carrasco et al. [25] for Exradin W1 PSD (0.25 ± 0.05%) for 150 cGy irradiation and better than that obtained by Debnath et al. [35] for an inorganic scintillator detector (0.26%) for 100 MU irradiation.

3.4.2 Dose-response linearity

Irradiation of the PSD by doses in the range of 25 to 2000 MU showed a linear relation between delivered and measured dose with less than 1% deviation. At a delivered irradiation of 5 MU, the measured dose deviated by 5.9% from the expected dose. Considering that 5.9% is only 0.16 cGy under these irradiation conditions, this difference is likely to be clinically inconsequential in many clinical situations. However, during VMAT delivery, majority of the dose is delivered in small portions, therefore, the impact of non-linearity of this PSD on VMAT dosimetry could be worthy of further investigation.

These results are similar to findings by Schoepper et al. [90] for the HS RP-100 readout system coupled to a 1 mm x 3 mm PSD probe. The group reported a difference of 2.93% at 5 MU, and differences lower than 1% for 10 MU and higher.

[1] based on patients from Jan. 2021 – May 2021, inclusive.

Jean et al. [52] demonstrated a similar trend with differences over 2% for 5 MU doses and lower, and differences less than 1% for 10 MU and higher. They used the HS RP-100 acquisition system coupled to three PSDs with dimensions of 1 mm by 7 mm, 1 mm by 6mm and 1 mm by 3.5 mm. The slightly poorer result of HS RP-200-1x1 can be explained by its smaller active volume compared to the probes used by Shoepper et al. and Jean et al. The HS RP-200-1x1 demonstrated noticeably worse linearity at low doses when compared to Exradin W1 and W2, which showed deviations of measured from expected dose of only 0.5% (over 0.15 to 6 Gy) and 0.05% (over 1-1000 MU), respectively [25], [42]. The non-linearity of HS RP-200-1x1 seen at low doses could be related to signal processing. Different relative noise levels at low doses compared to calibration conditions and/or higher doses might be affecting the applied background and Cherenkov corrections.

3.4.3 Dose rate dependence

For dose rates between 100 MU/min and 2400 MU/min, the response was found to be independent of dose rate, given a difference of less than 0.10% other than at 100 MU/min, which had a difference of 0.48%. For lower dose rates, this difference increased upwards 1.56% for 40 MU/min. These findings are consistent with Carrasco et al. [25] who found a dose rate independence for Exradin W1 to within 0.5% for dose rates of 200 – 600 MU/min and within 1% for 100 MU/min. Additionally, comparing to the HS RP-100 platform with 1 mm by 3 mm PSD probe, investigated by Schoepper et al. [90], they found dose rate independence to be within 1.18% for dose rates 200 – 600 MU/min, and up to 3.6% difference for dose rates lower than 200 MU/min. The findings in this report indicate an improved dose rate independence of HS RP-200-1x1 compared to similar PSDs and signal acquisition systems found in literature.

3.4.4 Field size dependence (output factors and small field corrections)

Given the good agreement of measured 6 MV energy beam relative output factors for HS RP-200-1x1 to field output factors found in literature for field sizes 1 x 1 cm^2 and larger, we can make a conclusion that for this energy HS RP-200-1x1 small field correction factor, $k_{Q_{clin},Q_msr}^{f_{clin},f_msr}$, equates to unity $k_{Q_{clin},Q_msr}^{f_{clin},f_msr}$ within uncertainty of 1.5%.

This can be expected considering the similarity of sensitive volume properties between Exradin W1 PSD (density 1.05 g/cm3) and Medscint PSD used in this study. The small field correction factors are reported in TRS-483 for Exradin W1 as 1.000 for field sizes down to 0.4 x 0.4 cm^2 [50]. However, as our measurements showed up to 3.1% disagreement of relative and field output factors at field size of 0.5 x 0.5 cm^2, further investigation is required to determine the values of $k_{Q_c lin, Q_m sr}^{f_c lin, f_m sr}$ for Medscint PSD at that field size and smaller fields. Monte Carlo simulations incorporating an accurate detector model based on manufacturer's specifications could be useful in resolving this discrepancy. It should be noted that the detector sensitive volume dimensions begin to approach the smallest field size of 0.25 x 0.25 cm^2, thus volume averaging effects may be more prominent, resulting in small field correction factors other than unity.

Based on the agreement of measured 10 MV-FFF energy beam relative output factors for HS RP-200-1x1 to field output factors found in literature, we can make a conclusion that for 10 MV-FFF beam small field correction factor, $k_{Q_c lin, Q_m sr}^{f_c lin, f_m sr}$, for HS RP-200-1x1 equates to a unity $k_{Q_c lin, Q_m sr}^{f_c lin, f_m sr}$ for field sizes 2 x 2 cm^2 and larger. For smaller fields, down to 0.5 x 0.5 cm^2, $k_{Q_c lin, Q_m sr}^{f_c lin, f_m sr}$ is expected to be within 4% of unity. Further investigation is required to more accurately determine small field correction factors for 10 MV-FFF energy at field sizes smaller than 2 x 2 cm^2.

Lechner et al. [64] reported small field output factors measured on several linac models at multiple institutions and using several detectors. For field sizes larger than 1 x 1 cm^2 the output factors measured in this study agreed with the data reported by Lechner et al. within 1.4%. However, for fields of 1 x 1 cm^2 and smaller considerable disagreement was found as shown in Figures 3 and 5. Also, results reported by Lechner et al. indicate a differences of over 45% between output factors measured on Varian TrueBeam STx (HD MLC) and Varian TrueBeam (millennium MLC) for the field size of 0.5 x 0.5 cm^2. The relative output factor measurements performed in this study did not show such a large difference between output factors for these models of Varian TrueBeam linacs. Our measurements on these two machines for beam energies of 6 MV and 10 MV-FFF showed output factor differences of up to 2.3% and 3.8% respectively, where the largest difference was measured at the smallest measured fields of 0.5 x 0.5 cm^2. These differences are much smaller than those reported by Lechner et. al., and the reason for the difference between our results and those by Lechner et. al. still needs to be clarified.

3.4.5 Angular dependence

The angular dependence, relative to gantry at 0°, of HS RP-200-1x1 was below 0.15%. This is in agreement with Carrasco et al. [25], who measured a maximum angular dependence of 0.34% for the Exradin W1, and Schoepper et al. [90] who measured a maximum angular dependence of 1.18% for HS RP-100 with 1 mm x 3 mm PSD probe. This finding indicates an isotropic response around the axis of symmetry for HS RP-200-1x1.

3.5 Conclusions

The HYPERSCINT RP-200 acquisition system coupled to a 1-mm diameter 1-mm long cylindrical PSD and HYPERDOSE analysis software presented very good short term repeatability, linear dose response, and independence of dose rate and axial angle. For very small doses of about 2.5 cGy, non-linear response was observed. Thus, user should be apprehensive if using HS RP-200-1x1 for VMAT dosimetry. Relative output factors were measured from 10 x 10 cm^2 down to 0.25 x 0.25 cm^2 for 6 MV and 10 MV-FFF energy beams. Small field output factor correction factors, $k_{Q_c lin, Q_m sr}^{f_c lin, f_m sr}$, were determined to be 1.0 for field sizes 1 x 1 cm^2 and larger for 6 MV beams, and also 1.0 for field sizes 2 x 2 cm^2 and larger for 10 MV-FFF beams. Relative output factors for very small fields (<1 x 1 cm^2) showed differences up to 4% compared to those measured with other detectors, and this requires further investigation. Monte Carlo simulations would be helpful in resolving the discrepancy in small field output factors. Overall, the HS RP-200-1x1 makes for a simple to use dosimeter and has potential uses in SRS QA and beam commissioning.

Chapter 4

Commissioning of SRS MapCHECK diode array for stereotactic dosimetry applications

4.1 Introduction

Stereotactic radiosurgery (SRS) is a technique frequently used in treatment of small tumours, particularly malignant brain lesions [79]. During SRS, tumours are irradiated with high fractions of dose under high dose rates, thus requiring submillimeter accuracy of dose placement [70]. The complex and high precision technique must be accompanied by detailed commissioning and ongoing quality assurance [45]. Typically, SRS treatments are delivered with the use of a linear accelerator. These days, single isocenter multitarget treatment is common [96], [94] featuring plans with many small multileaf collimator apertures. Introduction of many small fields adds further dosimetric complexity requiring very high dosimetric and geometric accuracy during radiation delivery to reduce the occurrence of serious complications from misplacement of dose. Pre-treatment verification focusing on patient end-to-end tests and quality assurance plays a crucial role in ensuring the safe and efficient delivery of SRS [27], [10]. Detectors most suitable for these tests have high spatial resolution. The industry gold-standard has been radiochromic film dosimetry, but this is a time and labour intensive method, which requires meticulous calibration and readout protocols and a skilled user [110], [68], [38]. A planar detector array has been developed by Sun Nuclear to ease the dosimetry process. SRS MapCHECK (Sun Nuclear, Mel-

bourne, USA) is a high resolution diode array accompanied by a dedicated phantom, StereoPHAN, and dedicated measurement and analysis software, SNC Patient Software. This system has been previously evaluated by several groups for dosimetric characteristics and validation of correction factors. These studies reported there has been some disagreement regarding field size and angular corrections. The aim of this chapter was to assess these parameters to potentially clarify the disagreements. Additionally, the aim was to characterize basic dosimetry related performance of the system and all of the calibration and correction factors being applied to the final dose values displayed. This study serves as the foundation for further investigation on the limitations of SRS MapCHECK in clinically challenging conditions (see Chapter 5).

4.2 Methods

4.2.1 Radiation source

All measurements were performed with Varian TrueBeam STx linear accelerator (Varian Medical Systems, Palo Alto, CA) equipped with high definition multi-leaf collimator—leaves are 2.5 mm wide at isocenter. All plans were delivered with beam energy of 6 MV with flattening filter.

4.2.2 Dosimetry system

This dosimetry system consists of three components including the SRS MapCHECK diode detector array (SMC), the StereoPHAN phantom, and the SNC Patient Software, all provided by Sun Nuclear Corp, Melbourne, FL.

Diode Array

SRS MapCHECK is a diode array with 1013 SunPoint 2 diode detectors. Each diode has an active area of 0.48 x 0.48 mm^2 and an active volume of 0.007 mm^3. The diodes are arranged on two printed circuit boards, shifted relative to each other by 1.75 mm in X and Y directions, covering a total area of 77 x 77 mm^2. The spacing between diodes is 2.47 mm at 45°and in-line spacing between diodes is 3.5 mm. The configuration of the diodes can be seen in Figure 4.1 left side. Both, the build-up and the backscatter plates consist of 22 mm thick polymethyl methacrylate (PMMA) plates. The build-up spacers can be seen in Figure 4.1 left side.

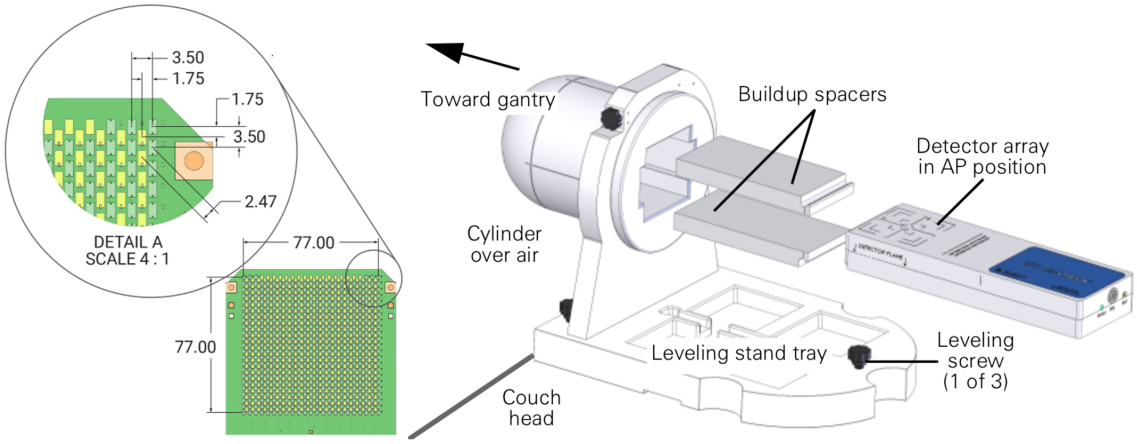

Figure 4.1: Left: Layout of diodes in SMC. Right: How all components necessary for measurements fit within the StereoPHAN. (SMC User Manual).

Phantom

StereoPHAN is designed to house the SMC for end-to-end testing of stereotactic radiosurgery plans. The StereoPHAN is a cylindrical phantom with a hemispherical end to mimic the head (see Figure 4.2 right side). Its diameter is 152 mm, its length is 208 mm, and it is composed of PMMA. The inner cavity, where SMC is accommodated, has L/W/H dimensions of 175 x 105 x 45 mm^3. The phantom offers five fiducial markers to help with alignment. The cylinder can rotate a full 360°. See Figure 4.2 left.

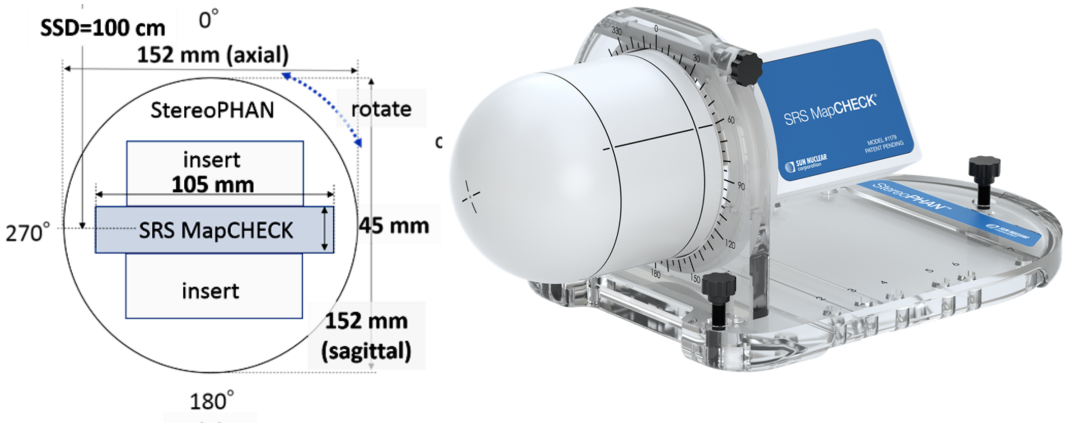

Figure 4.2: Left side: schematic representation of StereoPHAN and where SMC and build-up spacers sit. [114]. Right side: SRS MapCHECK housed within StereoPHAN. (StereoPHAN User Manual).

SNC Patient software

SNC Patient Software is a quality assurance software that works in conjunction with SMC to calibrate the array, to measure dose, and to analyze dose distributions. This software calculates and applies all relevant correction factors to the diodes to convert raw readings to a dose measurement. The software provides comparisons between measured and planned dose distributions or absolute to relative doses via gamma analysis, based on user selected values.

Detector calibration + Correction factors

In order to obtain dose readings, the raw diode response must be converted with the use of calibration and correction factors. All of these factors are obtained during the calibration procedure and applied via the SNC Patient Software (version 8.4).

The StereoPHAN CT files were obtained from Sun Nuclear and used to create a phantom representation in the treatment planning system with homogeneous composition. Dose was calculated to the phantom based on conditions defined in the calibration procedure. The absolute dose calibration, applied to the master (or central) diode, was directly derived from the TPS calculated dose to the central detector. The relative dose calibration was performed by placing SMC in anterior-posterior orientation (facing the beam) into the manufacturer provided calibration phantom initially aligned at isocenter and delivering four wide field irradiations (200 MU with 10 x 10 cm^2 field size) with indicated array shifts and rotations applied per irradiation. This was repeated for SMC in posterior-anterior orientation (facing away from the beam). The relative calibration accounts for differences in diode sensitivity and must be performed in both anterior-posterior and posterior-anterior orientations as SMC contains two detector circuit boards facing in opposite directions. Two measurements for SMC placed in the StereoPHAN were also performed (200MU with 5 x 5 cm^2 field size), one in each orientation.

Correction factors are calculated using the calibration and measurements via the SNC Patient software. Parallel-opposed field measurements during calibration help determine *angular correction factors* as diodes facing the beam have a higher response than those facing away from the beam. The differential response of forward and backward facing diodes is correlated to the incident angle of the beam (smooth, symmetrical, sinusoidal function), thus can be used to calculate the beam angle of incidence. The diode response also varies as a function of couch angle. This *couch*

angle correction factor is calculated by SNC Patient Software through linear interpolation of user input values of start and stop gantry angles for a specified couch angle. Diode response varies with temperature at an average rate of 0.5% increase in response per degree of increase in temperature. SMC contains six temperature sensors which calculate the temperature at each diode location used to scale the response according to the temperature gradient across the array. These values are also compared to the temperature at time of calibration and scaled to account for differences. The *temperature correction factor* is automatically applied without user input. Another factor affecting diode response is dose rate or pulse repetition frequency (MU/min), decreasing with decreasing dose rate. SNC Patient Software employs pulse counting to automatically record the pulse repetition rate and relates this rate to the rate at time of calibration to determine a *dose rate correction factor*. Diodes in SMC exhibit field size dependence in fields smaller than 2 x 2 cm^2, with an overresponse in small fields. The response of a given diode is correlated to the number of diodes in its vicinity, thus field size can be estimated on demand during a measurement. The SNC Patient software calculates a *field size correction factor* using this information.

The absolute dose for a given diode takes into account the background counts, the calibration dose, and correction factors.

4.2.3 Measurements

StereoPHAN, with SMC placed inside, was positioned at the accelerator isocenter using laser guidance, then positioned with improved accuracy using cone beam computed tomography (CBCT) imaging. All irradiations were performed with Varian TrueBeam STx linear accelerator with 6 MV energy beam at a dose rate of 600 MU/min, other than dose rate dependence measurements where dose rate was varied. SMC was connected to a computer placed outside the linear accelerator bunker.

StereoPHAN characterization with Monte Carlo

StereoPHAN was characterized with VMC++ in-house Monte Carlo simulator and compared to TPS AAA algorithm to ensure that AAA was calculating dose correctly. The dose distribution through StereoPHAN was calculated for 100 MU with a field size of 5 x 5 cm^2 delivered with the phantom located at isocenter. Percent depth dose was used as a comparison metric.

Pre/post irradiation leakage

A 10 minute dark current reading was taken prior to irradiation to determine pre-irradiation leakage. Then, 500 MUs were delivered with 10 x 10 cm^2 field size. To determine post-irradiation leakage, two dark current readings were taken—one immediately after the irradiation and one 60 seconds after the irradiation.

Short term repeatability

SMC was irradiated 10 times with 200 MUs with 5 x 5 cm^2 field size. The individual readings were compared to the average with standard deviation to determine short term repeatability.

Dose-response linearity

With field size of 5 x 5 cm^2, varying doses from 5 to 2000 MU were delivered to SMC. The SMC dose reading was graphed against the monitor units delivered to verify a linear relationship between SMC response and dose delivered. The output linearity of the linear accelerator was tested using a farmer chamber and confirmed to be within 0.3% down to 5 MU and to within 2% down to 1 MU.

Field size dependence (Field output factors)

Field output factors were measured as defined in Chapter 3. Briefly, the field output factor is simply the ratio of the measurement at a field size of n x n cm^2 to the measurement at a reference field size (in this experiment, 5 x 5 cm^2). The SMC was irradiated with 100 MU per irradiation for field sizes of 0.5 x 0.5 cm^2 to 5 x 5 ^{2}. These relative output factors were compared to those measured with HYPERSCINT RP-200 scintillator dosimeter placed at the location of the central detector of SMC and to the relative output factors calculated with TPS.

Angular dependence

StereoPHAN offers cylindrical symmetry along its central axis and spherical symmetry around one end. Although, the diodes themselves exhibit angular dependence, the SNC Patient software can automatically apply angular correction factors, thus no differences in dose measurements are expected at the central detector for various

gantry angles. At couch angle of 0°, StereoPHAN with SMC was positioned at isocenter. Then 200 MU was delivered with a field size of 5 x 5 cm^2 at gantry angles of 0°to 340°in 20°increments. This test was repeated with couch at angles of 45°and 90°and gantry angles of 0°to 180°. At each couch angle, dose readings were normalized to dose reading at gantry of 0o to evaluate any differences.

The SMC measurements, when relevant, were compared against TPS AAA algorithm (see Chapter 2) or Medscint HYPERSCINT RP-200 dosimetry system (see Chapter 3).

4.3 Results

4.3.1 StereoPHAN characterization

Percent depth dose profiles were taken through the center of the phantom for doses calculated with TPS algorithm AAA and with in-house VMC++ Monte Carlo modelling simulator. These profiles showed very good agreement. An example of a PDD for 5 x 5 cm^2 field size is given in Figure 4.3. For a field size of 5 x 5 cm^2 at 7.6 cm depth, where the diodes are located, the percent difference between AAA and VMC++ calculated dose was less than 0.01%. The percent difference at depth of d_{max} was 0.01%. At the entrance and exit, the doses do not perfectly match because VMC++ calculates dose to air outside the phantom, while AAA does not calculate this dose, thus VMC++ shows non-zero dose in those regions. Similar results were seen for field sizes of 1 x 1, 2 x 2, 10 x 10 cm^2.

4.3.2 Pre/post irradiation leakage and short term repeatability

The 10 minute dark current acquisition (no irradiation) yielded a dose of 0.06 cGy at the central diode. After delivering 500 MU, the reading immediately following the delivery was 0.008 cGy and the reading 60 seconds after delivery was 0.002 cGy at the central diode.

At the central diode, the average of 10 consecutive irradiations of 200 MU was 146.63 cGy with a standard deviation of 0.07 cGy and percent error of 0.05%.

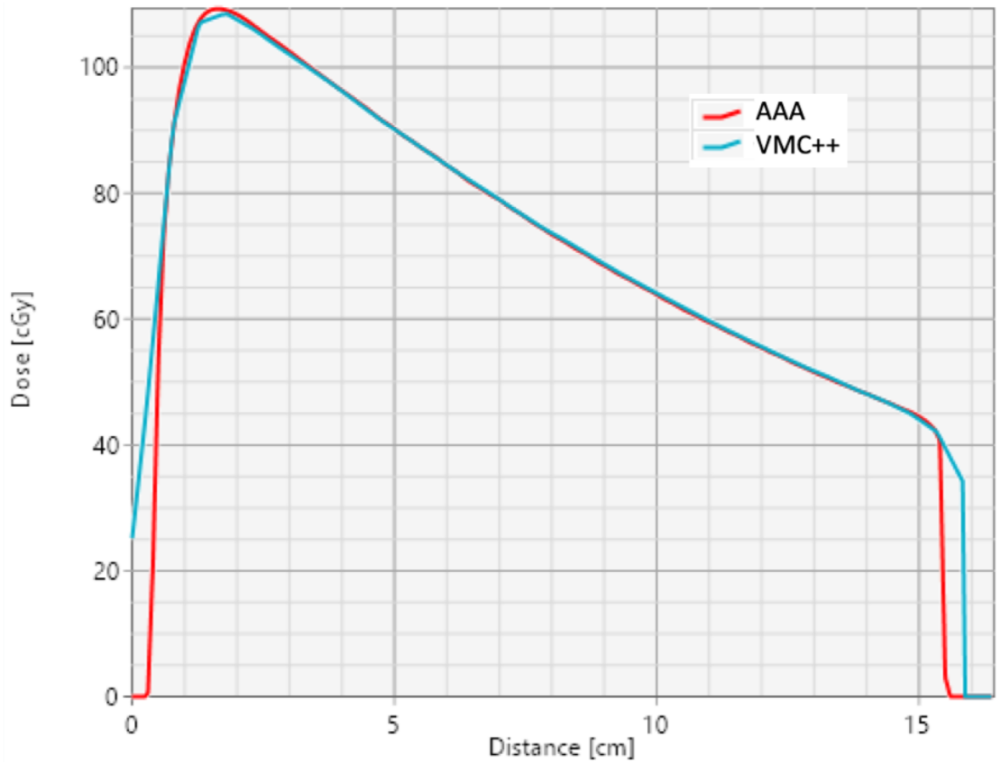

Figure 4.3: Percent depth profile through StereoPHAN at the central axis for 5 x 5 cm^2 field size. Dose calculated with AAA and VMC++.

4.3.3 Dose response linearity

SRS MapCHECK demonstrated a linear relationship between detector response and delivered dose, shown in Figure 4.4. This relationship is defined by Measured Dose (cGy) = 0.7341*Delivered Dose (MU) – 0.0514, with an R2 of 1. Deviations of measured dose from the expected dose defined by the linear equation were 0.5% or less for doses from 5MU to 2000MU. Under the setup conditions, 1 MU = 0.74 cGy at the central detector.

4.3.4 Dose rate dependence

The dose rate dependence of SMC is shown in Figure 4.5. SMC showed no dose rate dependence for dose rates of 100 – 600 MU/min. The average dose reading was 146.3 cGy with standard deviation of 0.3 cGy and percent error of 0.2%. Doses measured at each dose rate were within 0.5% of the average dose.

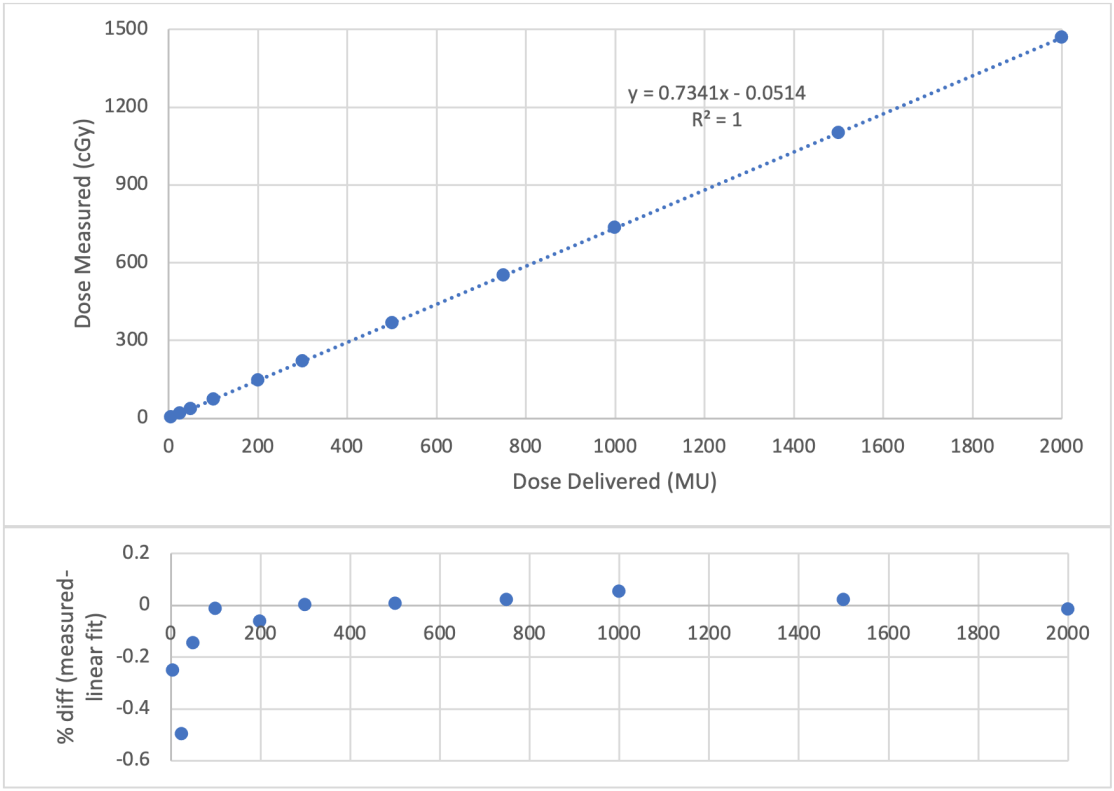

Figure 4.4: Dose response of SRS MapCHECK as a function of delivered dose in monitor units. A linear relationship is seen. Subplot shows the percent deviation of the measured dose from the dose expected based on the linear fit. Error bars are too small to be seen in figure. Uncertainty of 0.05%.

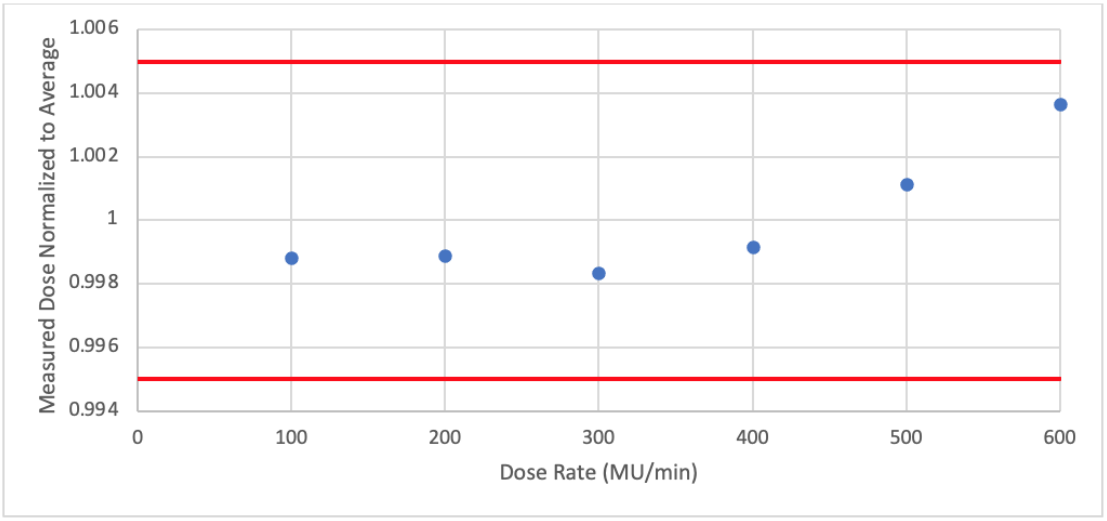

Figure 4.5: Dose rate response of SRS MapCHECK. The response is normalized to the average of all readings. Solid lines indicate ± 0.5%.

4.3.5 Field size dependence (Relative output factors)

Relative output factors for field sizes of 0.5 x 0.5 cm^2 to 5 x 5 cm^2 measured with SMC are shown in Figure 4.6. Also in this figure, relative output factors measured with HYPERSCINT RP-200, output factors calculated with TPS AAA, and output factors for SMC reported by Yasui [114] can be found. For field sizes of 1 x 1 $cm^2$and larger, the percent difference between SMC and HYPERSCINT RP-200 was less than 1%. For the field size of 0.5 x 0.5 cm^2 the percent difference was about 12%. The percent difference between SMC and TPS AAA or Yasui for field size of 2 x 2 cm^2 and larger was less than 1%. For field size of 1 x 1 cm^2 that difference was about 2% and 11%, comparing to AAA and Yasui, respectively. For field size of 0.5 x 0.5 cm^2 that percent difference was about 12% and 42%, comparing to AAA and Yasui, respectively.

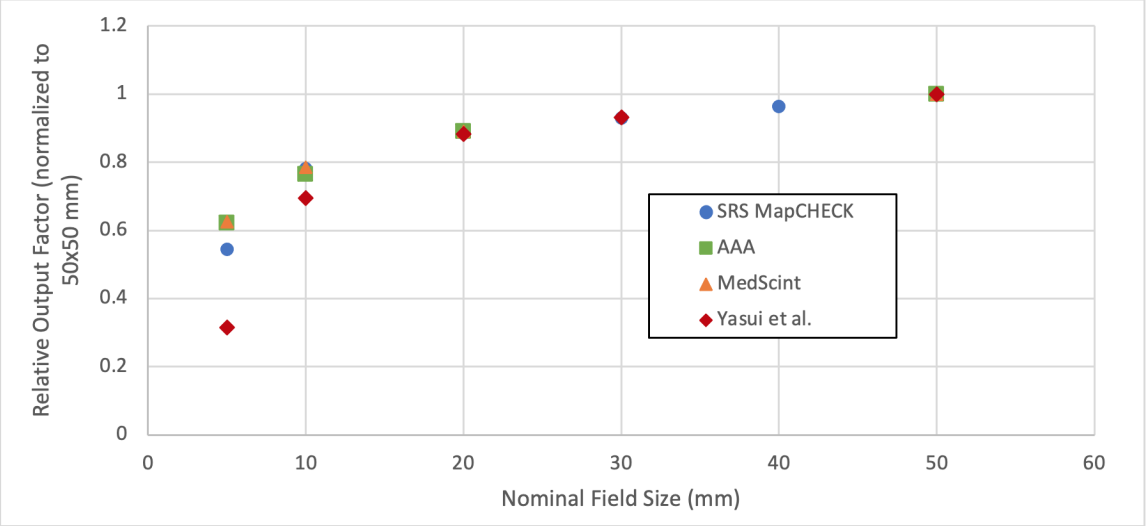

Figure 4.6: Relative output factors, normalized to 5 x 5 cm^2 field size, measured with SRS MapCHECK (blue circles), HYPERSCINT RP-200 (orange triangles), and TPS AAA (green squares) for Varian TrueBeam STx linear accelerator. Field output factors measured by Yasui et al. [114], normalized to 5 x 5 cm^2 field are also displayed (red diamonds).

4.3.6 Angular dependence

The dependence of the central diode of the SMC on gantry angle is shown in Figures 4.7-4.9. In Figure 4.7, the couch angle is 0°and the response is a function of gantry angle from 0 to 340 degrees, effectively describing angular dependence in the trans-

verse plane. The angular dependence was less than 2%, except at gantry angle of 100°where the difference was 2.2%.

In Figure 4.8, the couch angle is 45°and the response is a function of gantry angle from 0 to 180 degrees. The maximum deviation was 2.4% at gantry angle of 100°.

In Figure 4.9, the couch angle is 90°and the response is a function of gantry angle from 0 from 180 degrees, effectively measuring the angular dependence in the sagittal. A difference greater than 2% was seen for gantry angles around 60 and 120 degrees, otherwise differences were below 2%. The maximum angular dependence was seen at 60 degrees of 3.3%.

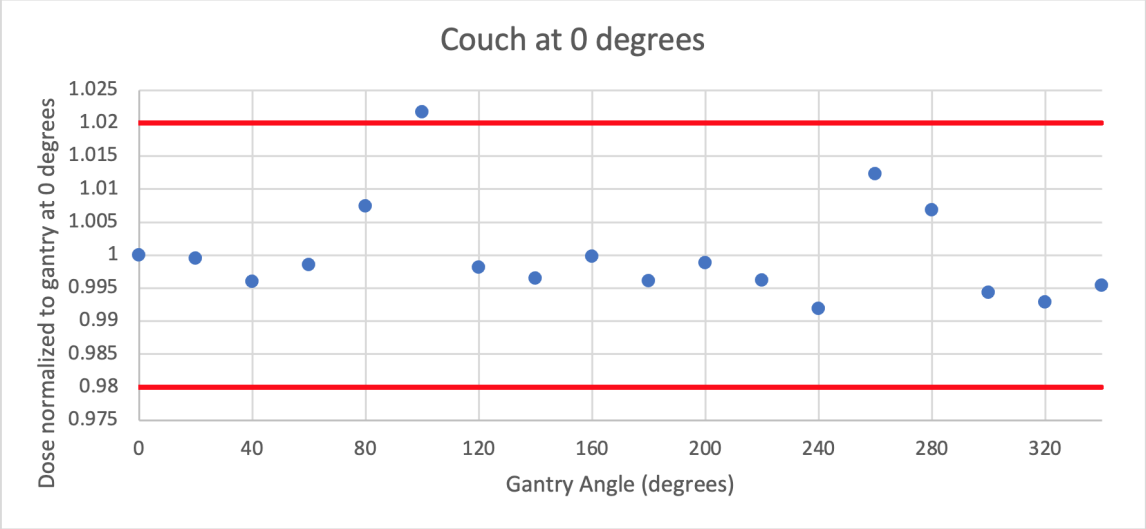

Figure 4.7: Couch at 0 degrees. Angular dependence of central diode in SMC. All measured doses normalized to dose for gantry at 0°. Red lines indicate 2% difference.

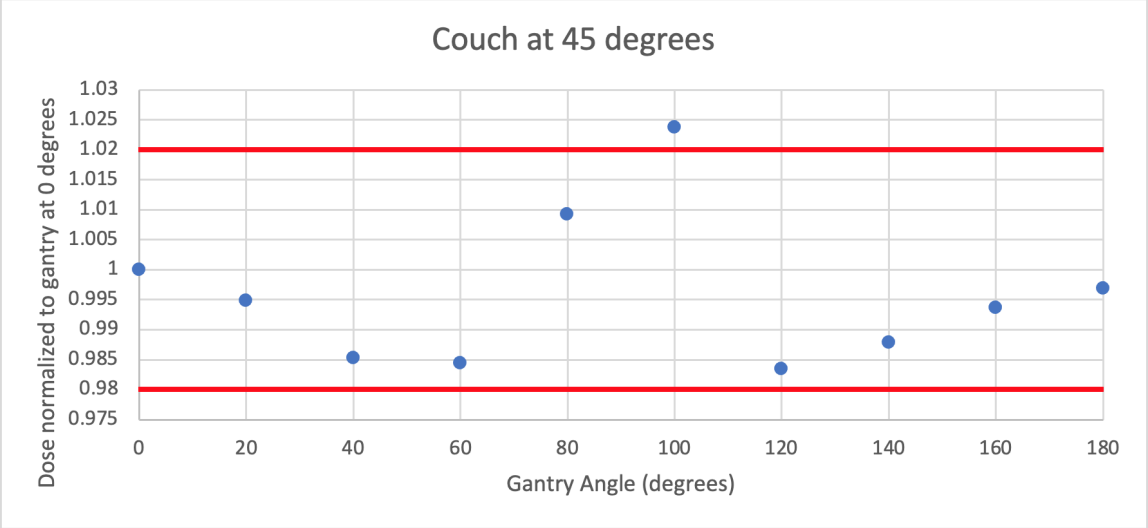

Figure 4.8: Couch at 45 degrees. Angular dependence of central diode in SMC. All measured doses normalized to dose for gantry at 0°. Red lines indicate 2% difference.

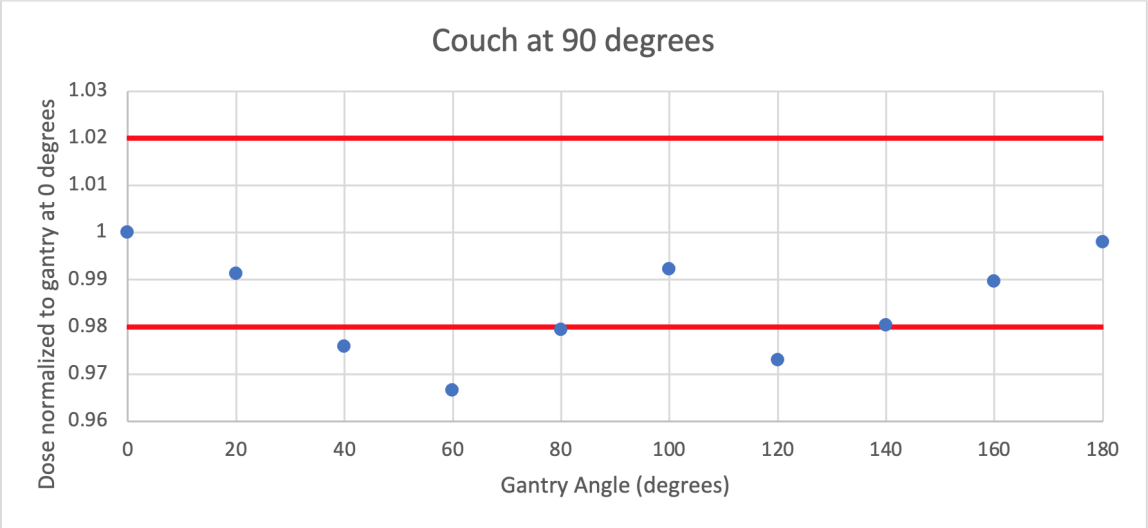

Figure 4.9: Couch at 90 degrees. Angular dependence of central diode in SMC. All measured doses normalized to dose for gantry at 0°. Red lines indicate 2% difference.

4.4 Discussion

Various dosimetric characteristics of SRS MapCHECK were examined. Overall, the basic tests indicated that the device performed within specifications outlined by Sun Nuclear. The dark current test showed that SMC has minimal leakage. The response of the detector for ten consecutive measurements showed that SMC was stable as the relative standard deviation was only 0.05%. Yasui et al. [114], found an average relative standard deviation of 0.06% when considering all diodes in the array while Sadowski et al. [89] found an average difference of 0.3%. Response was found to be linear within 0.5% for doses from 5 to 2000 MU. Both Yasui et al. and Sadowski et al. also demonstrated dose-response linearity from 5 to 1000 MU and 50 to 3500 MU, respectively. The repetition rate correction is sufficient as the response variation with dose rate (MU/min) was less than 0.5% in dose rate ranges relevant for treatment delivered with 6 MV beam. Ahmed et al. [3], evaluated SMC dosimetric characteristics in the same set up as in this study. Their results showed response variation within 1% for dose rates up to 1500 MU/min. Yasui et al. also found deviations of under 1% for dose rates between 50 MU/min and 2400 MU/min, validating the findings in this study. In field size dependence measurements, SMC appeared to under-respond for the smallest field size of 0.5 x 0.5 cm^2. When compared against HYPERSCINT RP-200 or TPS AAA calculated field output factors, the ones measured with SMC were about 12% lower. SMC field output factor for this field size was 42% higher than the one measured by Yasui et al. This is opposite to what Ahmed et al. found in their characterization, where SMC over-responded compared to a scintillator detector by about 3.2% at field size of 0.5 x 0.5 cm^2. For field sizes of 1 x 1 to 4 x 4 cm^2, Ahmed et al. found response differences less than 2.4%, which is supported by the findings in this study. For field sizes larger than 0.5 x 0.5 cm^2, SMC field output factors were within 2% compared HYPERSCINT RP-200 and TPS AAA. Field output factors measured for field sizes 2 x 2 to 5 x 5 cm^2 agree within 1% to those measured by Yusai et al. The agreement is reasonable for fields 1 x 1 cm^2 and larger, however, field size of 0.5 x 0.5 cm^2 should be studied further due to considerable disagreement between groups. The angular response in the transverse plane (couch at 0°) was within 1% except angles near horizontal (around 90 and 270 degrees), where the difference was just over 2%. This is in agreement with Yasui et al. and Ahmed et al. who found angular agreement to within 1% and 2%, respectively, for all angles, except around 90 and 270 degrees which had differences of about 5-7%.

While Sadowski et al. demonstrated angular agreement to within 0.5% for all gantry angles. For couch at 90°, the angular dependence in the sagittal plane was within 2%, except gantry angles around 60 and 120 degrees. Ahmed et al. demonstrated that angular dependence in the sagittal plane did not exceed 1%, excluding gantry angles of 60-120 degrees. For angles between 60 and 120 degrees, the electronic components are directly exposed to the beam, thus could be affecting the measurements and significant exposure could cause damage. At a 45 degree couch angle, the angular dependence was mostly within 2%, except at gantry angle of 100 degrees. For various combinations of couch and gantry angles, Ahmed et al. showed angular dependence within 1%, except at horizontal angles of irradiation (around 90 and 270 degrees) where differences over 3% were seen. The angular dependence findings in this study are in line with what Ahmed et al. is reporting. Overall, the angular dependence is minimal with variations of under 2%, except at angles parallel with the detector plane. This has been demonstrated in several studies and appears to not affect composite measurements [54], [13]. The tests performed indicate appropriate correction factors are being applied under most conditions. Further improvements in correction factor calculations should be considered for small fields and gantry angles nearly parallel with the detector array. The main goal of this process was to become familiar with the dosimetry system, to practice setting up and collecting measurements, to understand the correction factors being applied to the array and to characterize the basic dosimetric performance of the system.

4.5 Conclusions

SRS MapCHECK, in conjunction with StereoPHAN, demonstrated sufficient dosimetric accuracy and excellent dosimetric characteristics shown via comparison to a scintillator detector, a treatment planning system dose calculation algorithm (AAA), and other groups' findings. The simple setup and immediate display of results is a great clinical advantage. There are dose dependencies with field size (smaller than 1 x 1 cm^2) and incident angle of irradiation (irradiation directly parallel with diode array plane), which could serve to limit clinical utility for certain cases.

Chapter 5

Comparison of Dose Algorithms and Physical Dosimeters Under Challenging Conditions

5.1 Introduction

SRS MapCHECK is a patient-specific quality assurance tool. This diode-based detector array has a multitude of correction factors automatically applied through the use of SNC Patient software aimed at mitigating well-known diode dependencies with energy and spectral changes. Photon spectral changes occur at off axis positions and under small field conditions. There may be an increased contribution from head scatter photons off axis leading to hardening or softening of the spectrum depending on flattening filter presence, its material and geometric properties. Under small field conditions, the photon spectrum tends to harden due to decreased linac head scatter and decreased phantom scatter contributions [50]. These changes result in changes in the ratio of mass energy absorption and mass stopping power coefficients between water and detector medium necessitating correction factors for detectors made up of non-water materials.

Previously, the SRS MapCHECK has been verified for basic dosimetric properties such as dose-response linearity, dose rate and angular independence, and repeatability (Chapter 4). It was found that its measurement of output factors for field sizes smaller than 1 x 1 cm^2 deviates from those measured with other detectors or those derived from Monte Carlo simulated dose distributions. As well, it has been

reported that SRS MapCHECK measured dose comparison to treatment planning system shows differences under highly modulated VMAT plan delivery [88]. VMAT plans are typically composed of many small fields, which could be part of the reason for any discrepancies due to spectral changes associated with small fields. Additionally, SRS MapCHECK has been evaluated clinically as a quality assurance tool [8], [84], [76]. In this thesis, we are evaluating SRS MapCHECK from the dosimetric perspective focusing on conditions more challenging than typically encountered in clinical situations.

In this work, we rigorously test multiple methods of dosimetry under challenging conditions including physical measurements with SRS MapCHECK diode array and point scintillator dosimeter HYPERSCINT RP-200, TPS algorithms AAA and AXB, and MC algorithm VMC++ to find areas of disagreement. The main goals were to characterize generic dosimetric performance of SMC under small beam and off axis conditions, to investigate how it performs as a small field dosimeter, and to study its performance under highly modulated VMAT plans via comparison to the above mentioned dosimetric methods.

5.2 Methods

5.2.1 Radiation source

All measurements were performed with Varian TrueBeam STx linear accelerator (Varian Medical Systems, Palo Alto, CA, USA) equipped with high definition multi-leaf collimator—leaves are 2.5 mm wide at isocenter. All static field plans were delivered with beam energy of 6 MV with flattening filter (6 MV) and 10 MV flattening filter free (10 MV-FFF). All VMAT plans were delivered with 10 MV-FFF energy beam.

5.2.2 SRS MapCHECK

The dosimetry system comes as a package provided by Sun Nuclear Corp. and consists of three components—the diode array, the phantom, and the analysis software. A detailed description of each component is provided in Chapter 4 section 2, hence only a brief description is provided here for conciseness.

SRS MapCHECK diode detector array (SMC) comes with 1013 SunPoint 2 diode detectors aligned in two sheets facing each other with a spacing of 3.5 mm in X and Y

directions. Each diode has an active volume of 0.007 mm^3 and active area of 0.48x0.48 mm^2. The total area covered by the array is 77x77 mm^2. Configuration of the diodes is shown in Figure 4.1 (left).

StereoPHAN is a cylindrical phantom with one hemispherical end designed to house SMC for measurements (Figure 4.1 right). It is made up of polymethyl methacrylate (PMMA) and has dimensions of 152 mm and 208 mm for diameter and length, respectively. The entire cylinder can rotate 360^o and comes with fiducial markers for alignment purposes.

SNC Patient is the software accompanying the detector array and phantom. This software is used to calibrate the detector, to perform measurements, and to analyze the data. All calibration and correction factors (refer to Chapter 4 section 2.2.4) are applied automatically within this software outputting an absolute dose value per diode, which can be compared against other dose distributions via gamma analysis.

5.2.3 Coordinate systems

SRS MapCHECK follows the IEC 61217 Table Top coordinate system and Eclipse Integrated (Varian Medical Systems) treatment planning system (TPS) follows the DICOM coordinate system. These coordinate systems and conversions between the two are shown in Figure 5.1.

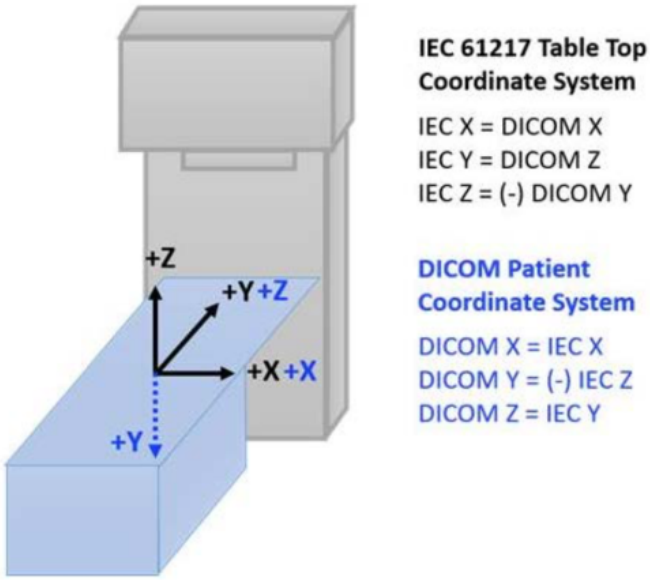

Figure 5.1: Conversion of DICOM to IEC coordinates. (SMC User Manual).

5.2.4 TPS algorithms

Eclipse TPS offers two photon dose calculation algorithms; analytical anisotropic algorithm and Acuros XB Advanced Dose Calculation algorithm, both are described in detail in Chapter 2 section 2.7.1.

All TPS calculations were performed on the phantom computed tomography images dataset provided directly by SunNuclear Corp. Both AAA and AXB dose distributions were calculated with a grid size of 0.1 cm.

5.2.5 Monte Carlo algorithms

A detailed description of Monte Carlo and VMC++ is provided in Chapter 2 section 2.7.2.

Generally speaking MC modelling is considered to be the most accurate modelling available for transport through linac components, beam forming components, and patient. However, there are approximations in the modelling of MLC leaves such as compositional and geometrical approximates (refer to [92], [60], [99] for more details). Modelling of small fields is likely to be more sensitive to these approximations.

All VMC++ calculations were performed with voxel size of 1 mm and uncertainty of 0.5%, except VMAT dose calculations, which had an uncertainty of 1%.

5.2.6 Challenging conditions examined

Static fields

Several sets of static fields were created, each focusing on a different variable in order to push the boundaries of the SMC device.

Field Size

Field size dependence was evaluated for field sizes from 5 x 5 cm^2 down to 0.25 x 0.1 cm^2. Field sizes are reported as equivalent square with nominal length and width as input. For example, the smallest field was formed with a single pair of MLC leaves (0.25 cm width) separated by 0.1 cm. The equivalent square side lengths would be 0.16 cm, so the field is reported as 0.16 cm. Plans were delivered with both 6 MV and 10 MV-FFF energy beams. SMC was irradiated with 100 MU per field and the doses for these fields were also calculated with AAA (1 mm voxel), AXB (1 mm voxel), and VMC++ (1 mm voxel, 0.5% uncertainty). SNC Patient software was used to calculate

gamma pass rates and point dose percent differences for the central detector per field.

Multi-target Static Small Fields

To further challenge SMC with small field sizes, three multi-target plans were created where each field was formed by a single pair of MLC leaves separated by varying distances (inter-leaf distance). One plan consisted of two small fields, each located 3 cm away from the central diode along the x-axis of the detector plane (laterally in DICOM patient coordinate system). The second plan consisted of two small fields, each located 3 cm away from the central diode along the y-axis of the detector plane (superior-inferior in DICOM patient coordinate system). The last plan was a combination of the first two (by rotation collimator by 90^o for one set of fields) forming a four field plan shown in Figure 5.2. Again, these three plans were delivered with both 6 MV and 10 MV-FFF energy beams.

To evaluate the performance of SMC, in plane and cross plane profiles were taken through the targets and compared against AAA, AXB, and VMC++ calculated dose distributions.

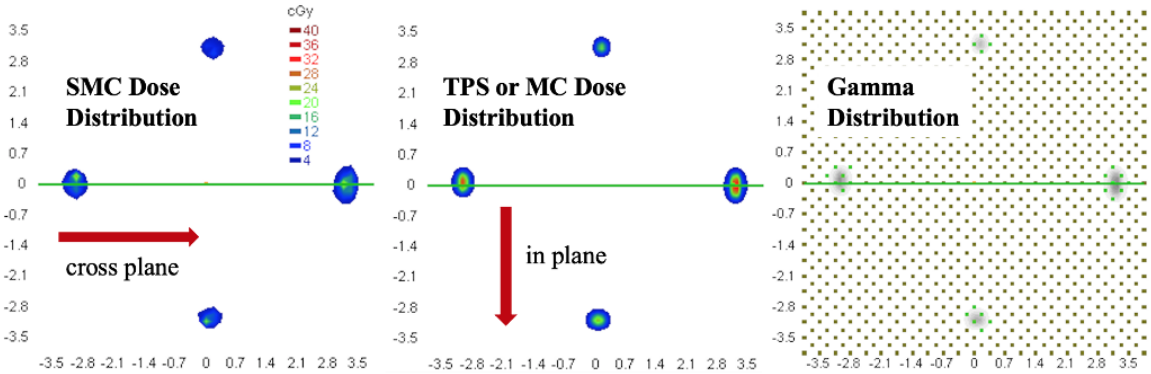

Figure 5.2: Example of a four small target static field—all targets formed with single leaf at widths of 1 mm (top), 2 mm (bottom), 3 mm (left), and 4 mm (right). Screenshot taken from SNC Patient interface.

Isocentric vs. off-axis fields

To better understand how SMC handles off axis measurements, the central diode was shifted away from the CAX by 6 cm in -X and +Z directions (please see DICOM patient coordinate system). Plans were created using 6 MV and 10 MV-FFF energy beams with 0.5 x 0.5 cm^2, 1 x 1 cm^2, and 2 x 2 cm^2 field sizes now targeting the shifted central diode. These plans were delivered to SMC and the dose distribution

was calculated with AAA, AXB, and VMC++. Point dose percent difference was used to evaluate the performance.

VMAT fields

Degree of Modulation

A set of plans was created with varying degrees of modulation. The PTV dimensions were chosen to be around 2 cm in diameter to be representative of a potential SRS treatment and to ensure that the field size was not inherently too small in order to reduce effects of small field conditions. The jaws were set to 4 x 4 cm^2, by keeping the field at this larger size, any effects or trends should be due to modulation alone.

Plans were created in Eclipse system by Varian Medical Systems Inc (Palo Alto, CA., USA). PTV coverage constraints along with constraints on artificial adjacent "organs at risk" (OARs) were applied to force optimization algorithms to produce plans with different degree of modulation. Requirement for the algorithm to use a set number of monitor units (MUs) was also used to achieve required modulation level. Some of the plans were created with the use of Progressive Resolution Optimizer (Version 13.6.23) and some were created with the use of Photon Optimizer (Version 15.6.06). A total of 17 on axis VMAT plans were created with modulation scores ranging from 2.66 to 10.21 MU/cGy. Modulation scores were defined by monitor units divided by the central dose as calculated by TPS AAA (Version 13.6.23).

These plans were delivered to SMC and doses were calculated with AAA (1 mm), AXB (1 mm), and VMC++ (1 mm, 0.5% uncertainty). With the use of SNC Patient software, gamma pass rates were evaluated for SMC compared to the computational dosimetry and plotted against modulation score.

Off Axis Modulation

A similar method was employed to generate VMAT plans off axis. The central diode was shifted +6 cm in Z direction (DICOM patient coordinate system) and the same parameters were set in terms of PTV dimension, monitor units, and no additional optimizers. In total, 11 off axis VMAT plans were created with modulation score ranging from 2.70 to 9.76 MU/cGy. These plans were delivered to SMC and doses were calculated with AAA, AXB, and VMC++. Gamma pass rates were evaluated with the use of SNC Patient software and plotted against modulation score.

Patients

To examine SMC detector diode array performance under more clinically relevant, yet still challenging conditions, several clinical VMAT plans were evaluated. SMC dose measurements were compared to dose calculations performed by the TPS or MC.

Six brain SRS patient cases, where quality assurance results were subpar, have been identified for analysis with SMC. All six cases were treated in a single fraction with 10 MV-FFF energy beam for a PTV size of around 1 cm. Four of the six plans were multi-target with two PTV regions and two were a single target plan. All of the plans consisted of two arcs. The patient quality assurance tests indicated PTV point dose differences of 7.4 to 8.3% between microdiamond measurement and clinical TPS algorithm AAA.

The dose for these plans was recalculated on the StereoPHAN phantom with the central detector located at the center of the PTV for the single target plan and the center of the PTV with the higher dose in case of multi-target plans. Dose was calculated with TPS algorithms AAA and AXB (voxel 1 mm) and with MC algorithm VMC++ (1 mm resolution, 1% uncertainty). These plans were delivered to SMC housed within the StereoPHAN and then to HYPERSCINT scintillator detector housed within StereoPHAN as well. Point dose percent differences were calculated for the central diode between SMC and every other method. Gamma analysis (3%/1mm with 80% threshold) was performed between SMC and computationally derived dose distributions.

5.2.7 Gamma Analysis

The gamma index measures coincidence between measured and calculated dose distributions using percent dose difference and distance-to-agreement (DTA) criteria (refer to Chapter 2 section 2.8 for more details). Global γ with 80% threshold and 10% threshold were evaluated. Focusing on SRS/SRT applications, the DTA tolerance was chosen at 1 mm following clinical protocol, and the percent dose difference was chosen at 3%.

In addition to gamma analysis, point percent difference was used to evaluate single diode/point doses between various dosimetry methods. Percent difference was calculated for the central diode as (absolute dose of SMC – absolute dose of another dose distribution)/absolute dose of another dose distribution * 100%.

5.3 Results

5.3.1 Static fields

Field size

Gamma pass rates for SMC and other dose calculation methods (AAA, AXB, or VMC++) were calculated for field sizes, defined by equivalent square method (see Chapter 3 section 2.2.5), of 0.16 cm to 5 cm. The gamma pass rates (3%,1mm) were calculated for threshold levels of 10% and 80% and for measurements with both the 6 MV energy beam and 10 MV-FFF energy beam. These values can be seen in Figure 5.3. Gamma pass rates were above 97% for all field sizes except 1 cm for both energies and all dose calculation methods. For 6 MV energy and 1 cm field size lowest gamma pass rates were 90%, 83%, and 91% for SMC comparison to AAA, AXB, and VMC++, respectively. For 10 MV-FFF energy and 1 cm field size lowest gamma pass rates were 70%, 70%, and 67% for SMC comparison to AAA, AXB, and VMC++, respectively.

Since gamma pass rates were calculated for only one diode for field sizes up to 0.5 cm, percent difference was used to better visualize differences. These dose differences for 6 MV energy beam are found in Figure 5.4 and for 10 MV-FFF the percent differences are found in Figure 5.5. For 6 MV energy, percent difference was under 4% for field sizes of 1 cm and larger when comparing to AAA, VMC++, and AXB. For smaller field sizes, the percent difference increased with decreasing field size up to 24% for the smallest field size of 0.16 cm. For the most part, SMC was measuring higher doses than other methods for 6 MV energy beam. For 10 MV-FFF energy, the percent difference was less than 3% for field sizes of 2 cm and larger. For smaller fields the percent difference increased with decreasing field size up to 18% for the smallest field size of 0.16 cm. SMC was mostly measuring lower doses compared to other methods.

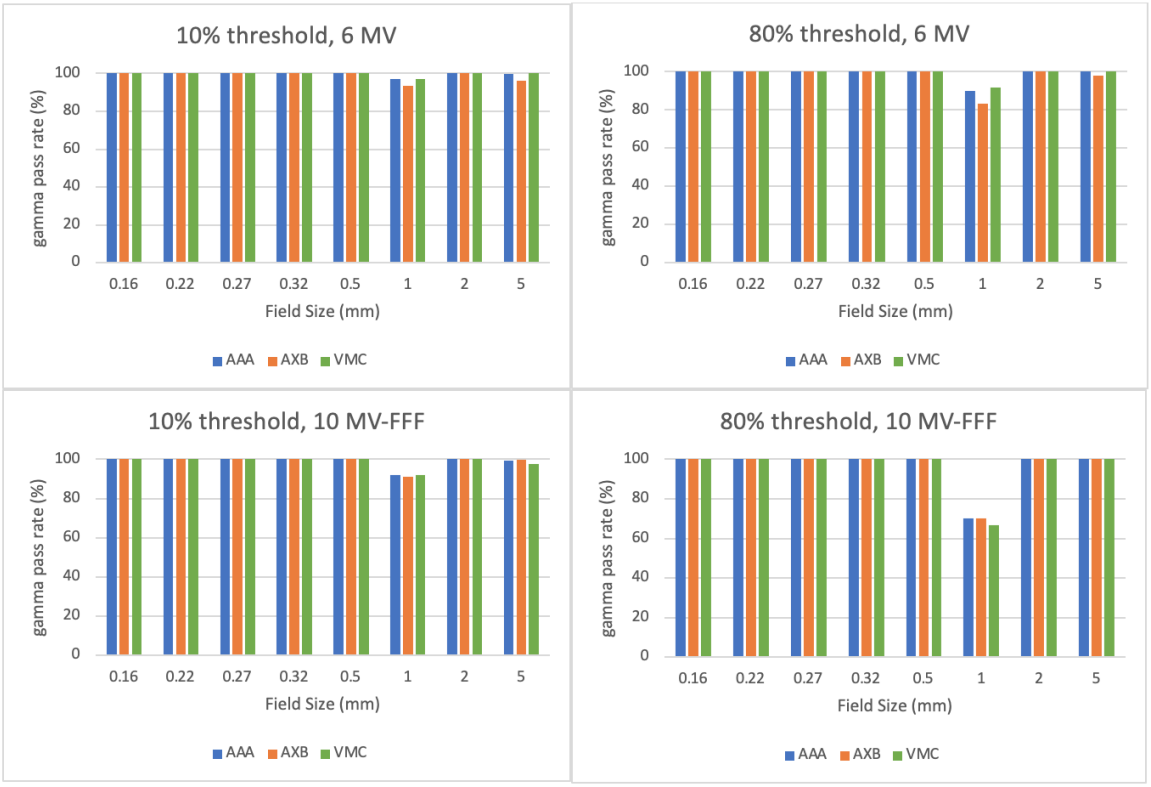

Figure 5.3: Gamma pass rates (with 10% and 80% thresholds) for beam energy of 6 MV and 10 MV-FFF, for equivalent square field sizes 0.16 cm to 5 cm. Gamma pass rates of SMC compared to another method (SMC-AAA—blue, SMC-AXB—orange, SMC-VMC++ —green).

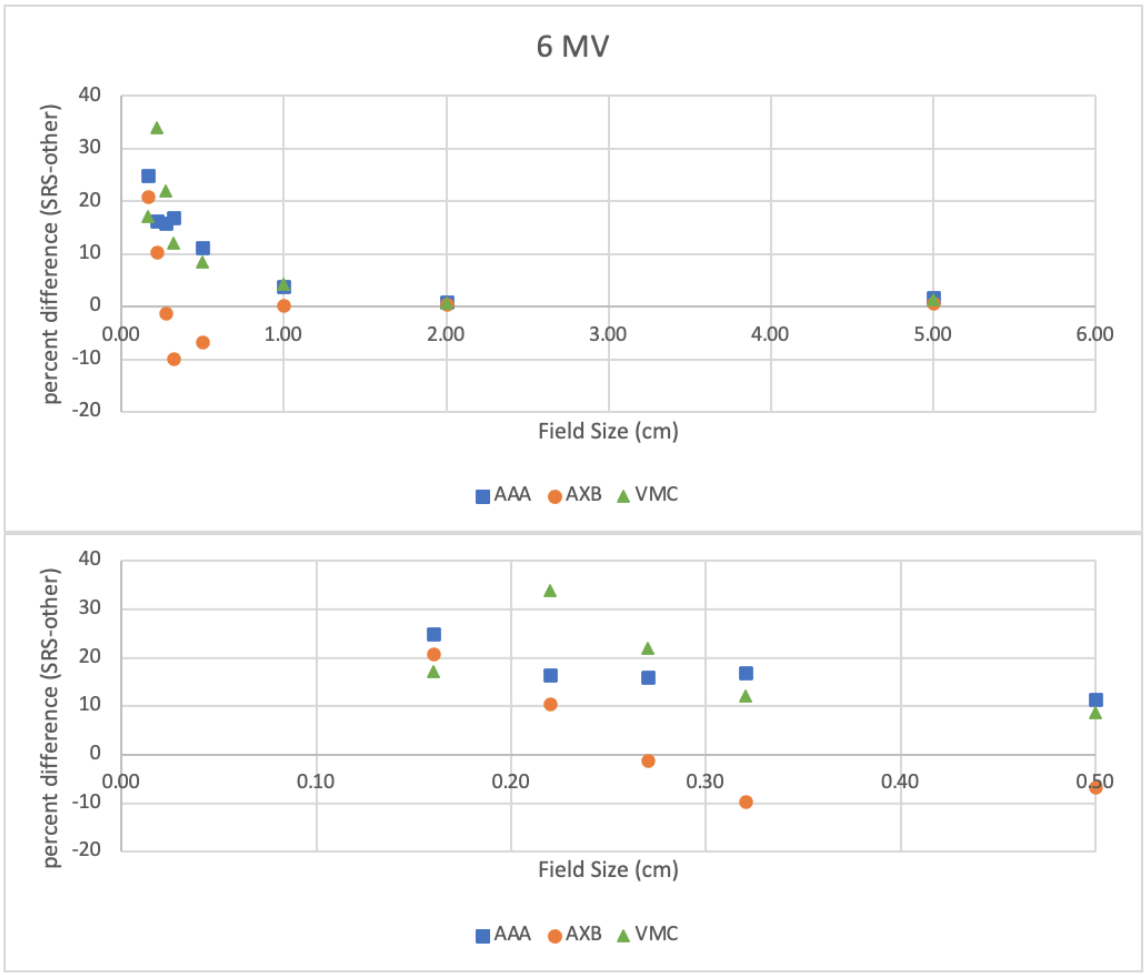

Figure 5.4: Top: For beam energy of 6 MV, the percent difference between SMC and another dose calculation method for the central detector for equivalent square field sizes of 0.16 to 5 cm. Bottom: zoom in of field sizes 0.16 to 0.5 cm. SMC-AAA—blue square. SMC-AXB—orange circle. SMC-VMC++ —green triangle.

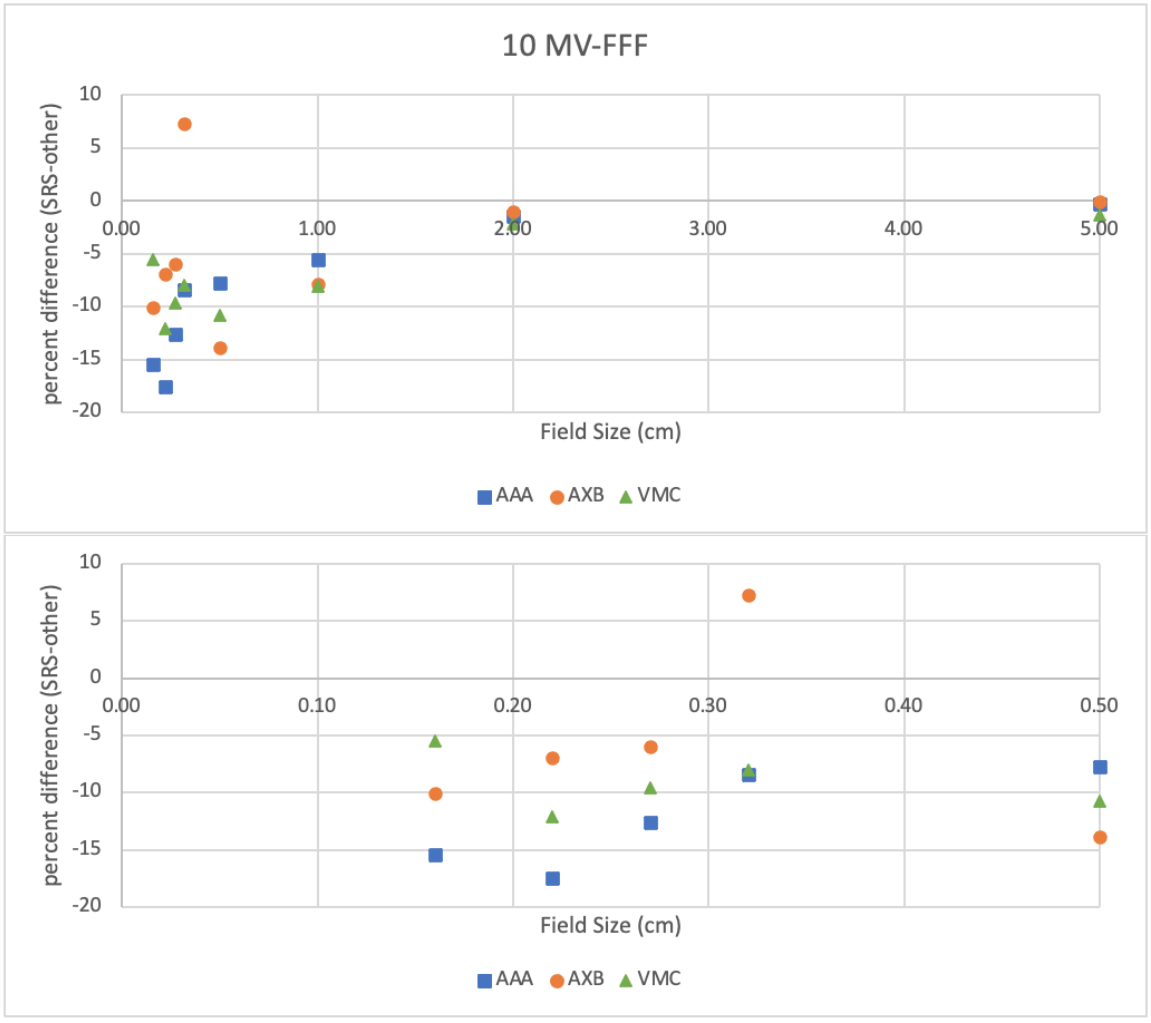

Figure 5.5: Top: For beam energy of 10 MV-FFF, the percent difference between SMC and another dose calculation method for the central detector for equivalent square field sizes of 0.16 to 5 cm. Bottom: zoom in of field sizes 0.16 to 0.5 cm. SMC-AAA—blue square. SMC-AXB—orange circle. SMC-VMC++ —green triangle.

Multi-target small static fields

The cross plane dose profiles for a plan with two lateral small targets are shown on the left half of Figures 5.7 and 5.8 for 6 MV and 10 MV-FFF beam energy, respectively. On the right side of those figures, the in plane dose profiles for a plan with two small sup-inf targets are shown. Refer to Figure 5.6 for MLC shaping of these plans. There is a good match between profiles obtained with SMC diodes and computational dose methods in terms of profile shape as can be seen by the spatial distribution of peaks and profile width. The absolute dose values match as well, except when computed with AXB, which appears to over-estimate the dose compared to other methods. All gamma pass rates (3%/1mm with 10% threshold) were over 90% for all multi-target plans for both 6 MV and 10 MV-FFF energies. 10% threshold was chosen for gamma analysis to ensure that all targets were used for the evaluation. Overall, higher gamma passing rates were seen for 6 MV energy beam than 10 MV-FFF.

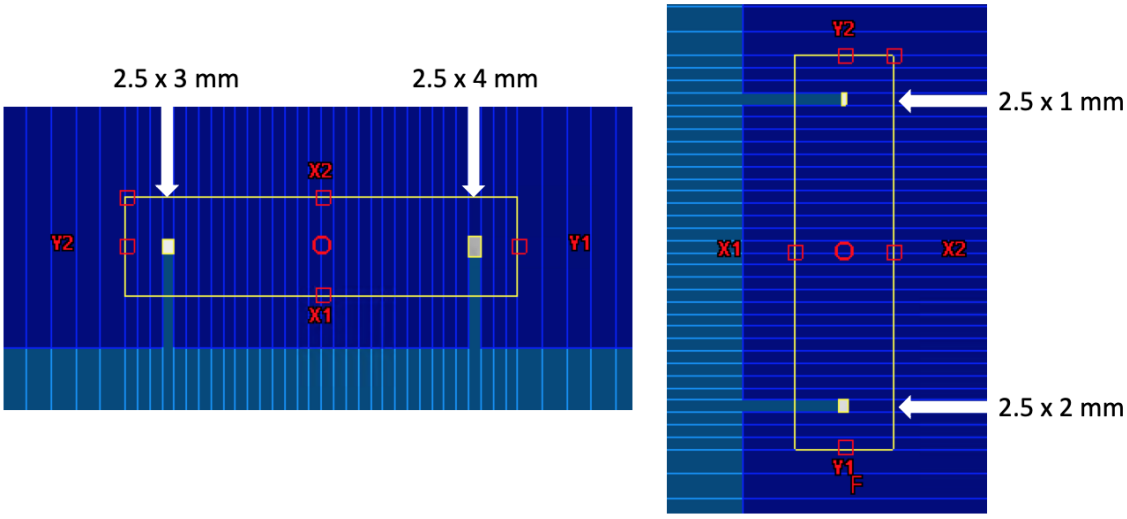

Figure 5.6: Left: Two small field plan. Fields located laterally (left field is 2.5 x 3 mm^2, single leaf pair open to 3 mm width, right field is 2.5 x 4 mm^2, single leaf pair open to 4 mm width). Right: Two small field plan. Fields located superior-inferior (superior field is 2.5 x 1 mm^2, single leaf pair open to 1 mm width, inferior field is 2.5 x 2 mm^2, single leaf pair open to 2 mm width).

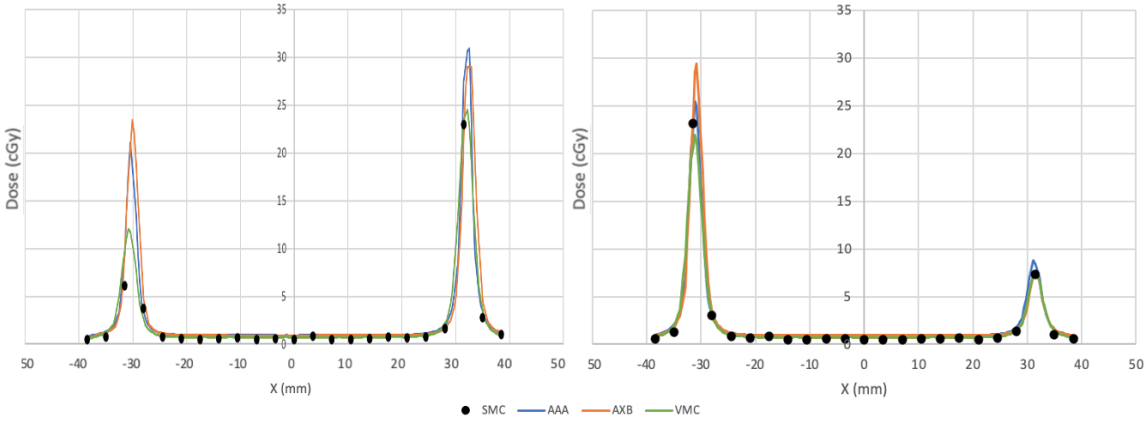

Figure 5.7: 6 MV energy beam. Left: Cross plane profiles through central diode obtained with SNC Patient software for two small field plan, fields located laterally (left field is 2.5 x 3 mm^2, single leaf pair open to 3 mm width, right field is 2.5 x 4 mm^2, single leaf pair open to 4 mm width). Right: In plane profiles through central diode obtained with SNC Patient software for two small field plan, fields located superior-inferior (superior field is 2.5 x 1 mm^2, single leaf pair open to 1 mm width, inferior field is 2.5 x 2 mm^2, single leaf pair open to 2 mm width). Profiles included for SMC diode array, AAA, AXB, and VMC++.

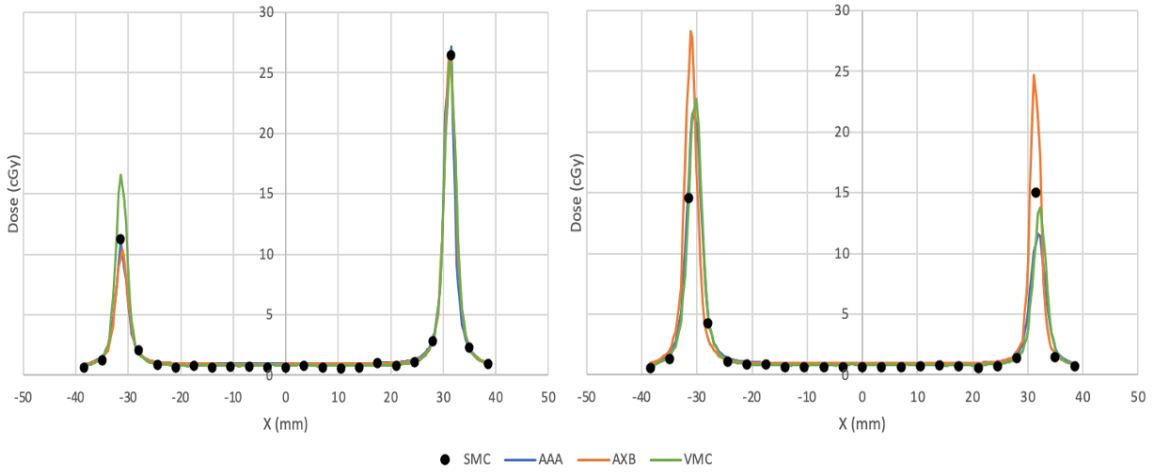

Figure 5.8: 10 MV-FFF energy beam. Left: Cross plane profiles through central diode obtained with SNC Patient software for two small field plan, fields located laterally (left field is 2.5 x 3 mm^2, single leaf pair open to 3 mm width, right field is 2.5 x 4 mm^2, single leaf pair open to 4 mm width). Right: In plane profiles through central diode obtained with SNC Patient software for two small field plan, fields located superior-inferior (superior field is 2.5 x 1 mm^2, single leaf pair open to 1 mm width, inferior field is 2.5 x 2 mm^2, single leaf pair open to 2 mm width). Profiles included for SMC diode array, AAA, AXB, and VMC++.

Isocentric vs. off axis fields

Percent difference between SMC and another dose distribution for the central diode for field sizes of 0.5 to 2 cm measured both on axis and off axis are shown in Figure 5.10 and 5.11. The fields were measured at isocenter, -6 cm off axis in X (left DICOM coords) direction and +6 cm off axis in Z (superior DICOM coords) direction. In the figures, the grey sections indicate collimator rotation of 90 degrees, otherwise collimator rotation is 0 degrees. For 6 MV energy at 0.5 cm field size, the percent differences per method span about 11%, for 1 cm field size the spread drops to 4%, and for 2 cm field size the spread is about 1%. The percent differences at isocenter were closer together indicating better agreement between all methods compared to off axis measurements. There is a clear relationship with field size expressed by smaller percent differences at larger fields. No clear relationship between with collimator angle was established.

Figure 5.9 displays the cross plane profiles of 6 MV energy beam for field sizes 0.5 x 0.5 to 2 x 2 cm^2 for phantom shifted 6 cm along the +Z direction.

For 10 MV-FFF energy at 0.5 cm field size the total percent difference spans over about 8%, 1 cm field size the span is about 6%, while for the 2 cm field size the total span is just under 4%. Again these measurements indicate no dependence on collimator angle, but a clear indication to a relationship with field size was observed with smaller percent difference at larger field sizes. For systematic difference of the dose measured by SMC relative to alternative dosimetry methods is seen, with SMC measuring on average about 5% to 10% higher for fields of 1 x 1 and 0.5 x 0.5 cm^2, respectively.

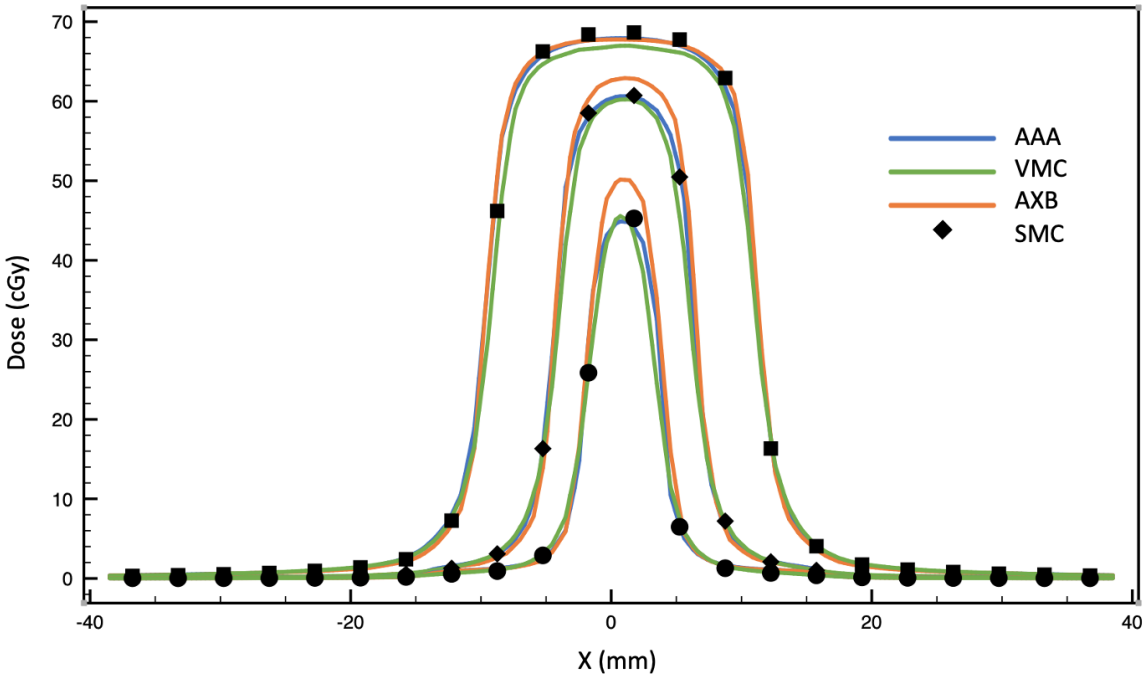

Figure 5.9: For 6 MV energy beam, cross plane profiles of field sizes of 0.5 x 0.5 to 2 x 2 cm^2 at +6 cm along the Z axis (superior).

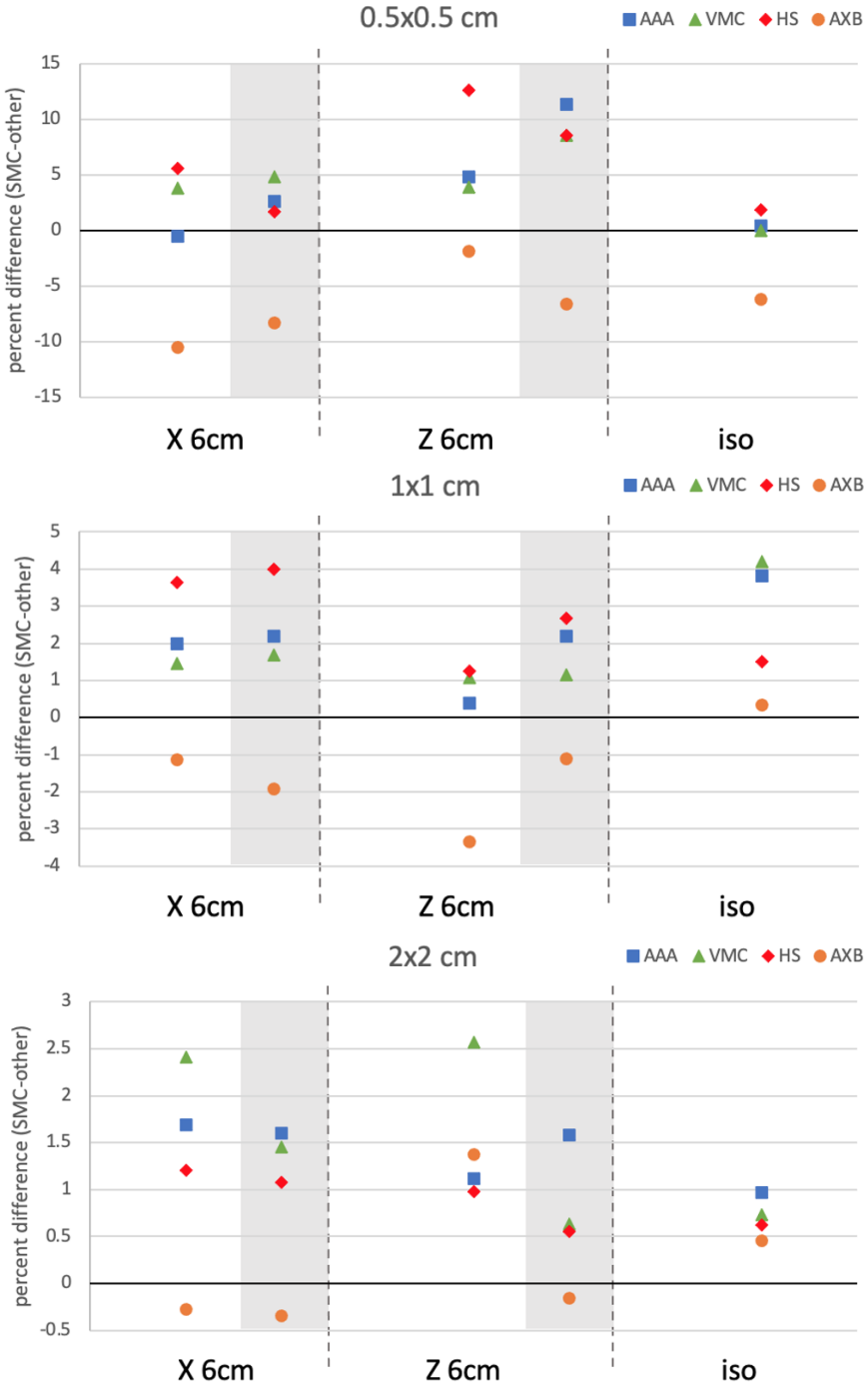

Figure 5.10: Percent difference of SMC central diode on and off axis for field sizes of 0.5 cm (top), 1 cm (middle) and 2 cm (bottom) under 6 MV energy beam. Grey sections indicate collimator angle of 90 degrees, otherwise collimator rotation is 0 degrees. Blue squares show SMC-AAA. Green triangles show SMC-VMC++. Red diamonds show SMC-HYPERSCINT. Orange circles show SMC-AXB.

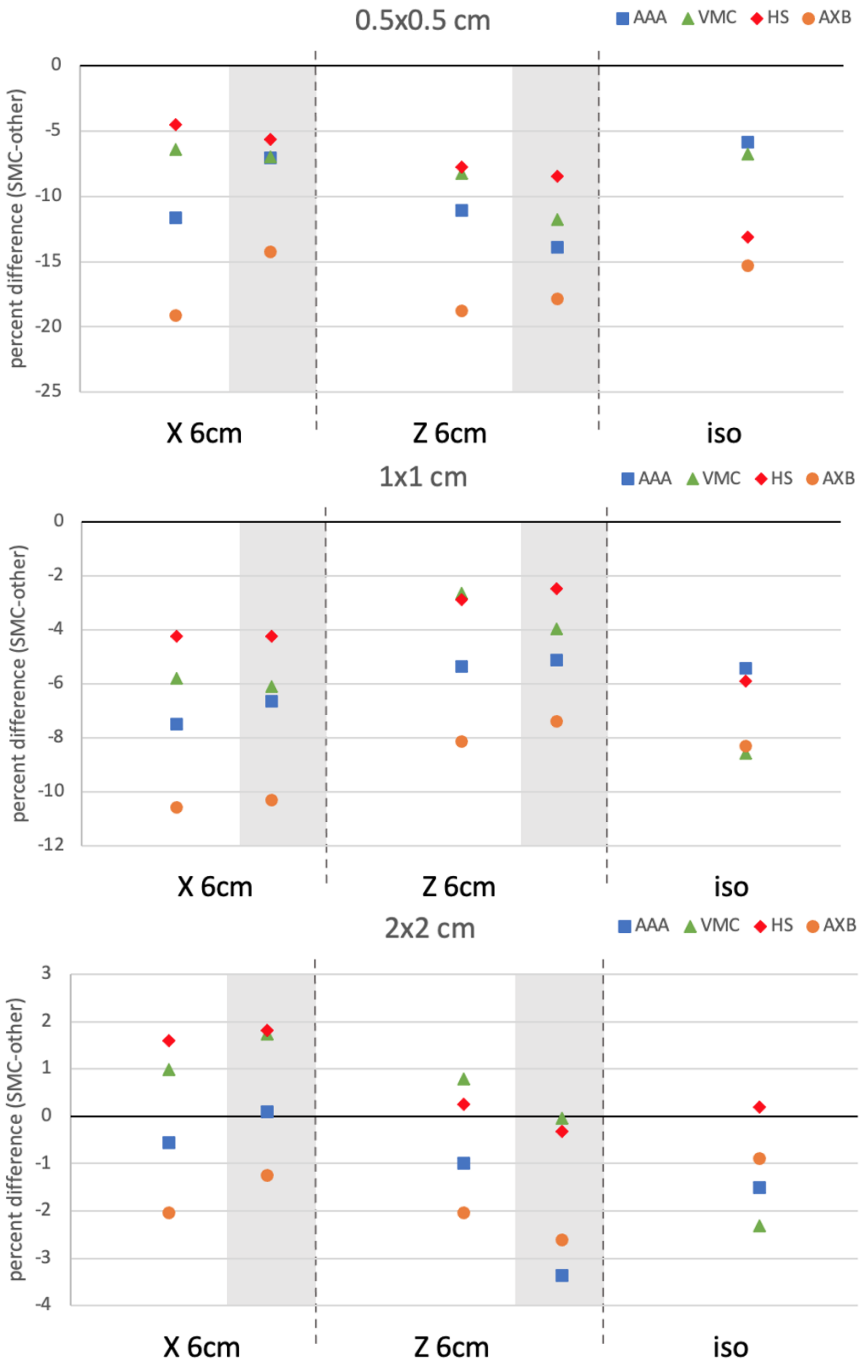

Figure 5.11: Percent difference of SMC central diode on and off axis for field sizes of 0.5 cm (top), 1 cm (middle) and 2 cm (bottom) under 10 MV-FFF energy beam. Grey sections indicate collimator angle of 90 degrees, otherwise collimator rotation is 0 degrees. Blue squares show SMC-AAA. Green triangles show SMC-VMC++. Red diamonds show SMC-HYPERSCINT. Orange circles show SMC-AXB.

5.3.2 Comparison of dosimetry for VMAT plans

Isocentric VMAT dose distributions

The gamma pass rates (3%/1mm) for VMAT plans delivered on axis as a function of modulation score are found in Figures 5.12 and 5.13. Modulation score for each plan was defined as MU divided by the AAA calculated CAX dose and ranged from 2.65 to 10.21 MU/cGy. For 10% threshold, gamma pass rates showed a negative correlation with modulation score defined by Pearson's correlation coefficients of 0.54, 0.67, and 0.60 when comparing SMC to AAA, AXB, and VMC++, respectively. All had $p < 0.05$, thus are statistically significant. For 80% threshold, gamma pass rates showed a negative correlation with modulation score defined by Pearson's correlation coefficients of 0.67, 0.75, and 0.56 when comparing SMC to AAA, AXB, and VMC++, respectively. All have $p < 0.05$.

There was a plateau region evident up to around 6 MU/cGy where gamma pass rates are consistent. For 80% threshold, Pearson's correlation coefficient for this low modulation region was 0.85 when comparing SMC to AAA. However, when comparing to AAA or VMC, Pearson's correlation coefficients were 0.06, and 0.05, respectively, indicating no correlation. Gamma pass rates for SMC-AAA were all above 97%, with an average pass rate of 98%. For SMC-VMC++ the average pass rate in this region was 86%. For SMC-AXB, the average pass rate is 97% with all, but one plan scoring above 90% gamma pass rate.

Over the entire range of modulation scores, SMC agreement with AAA was the best with 59% of all plans scoring gamma pass rates above 90%. Comparison to AXB resulted in 35% of plans obtaining gamma pass rates above 90%. Comparison to VMC++ resulted in about 12% of VMAT plans with gamma pass rates over 90%. For isocentric VMAT plans, SMC comparison to AAA offered the most consistent results.

Cross plane and in plane profiles for the lowest and highest gamma pass rates for VMAT plans are found in Figures 5.14-5.17.

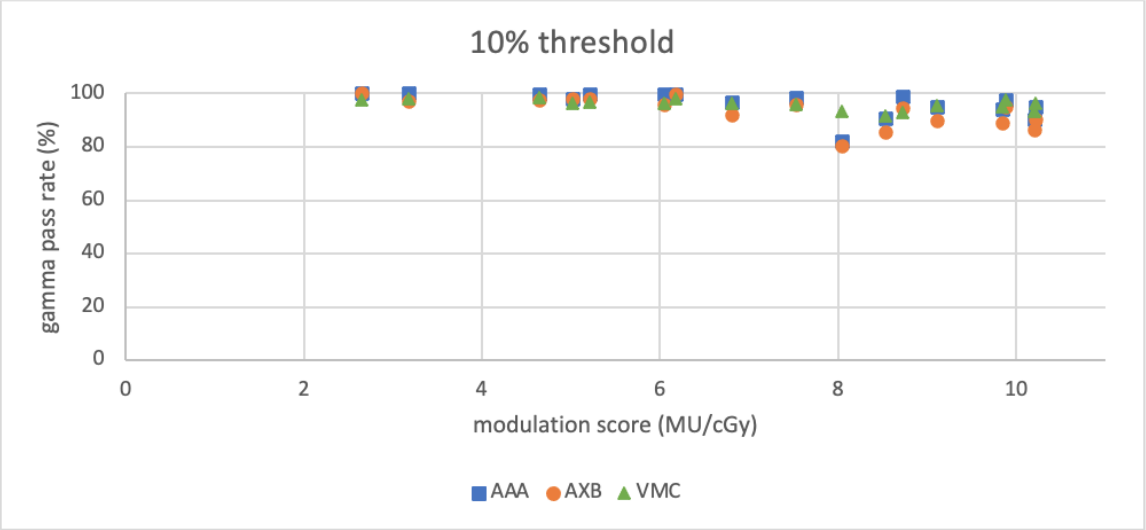

Figure 5.12: 10% threshold, on axis VMAT delivery gamma pass rates as a function of modulation score for 10 MV-FFF beam energy. SMC-AAA—blue square. SMC-AXB—orange circle. SMC-VMC++ —green triangle.

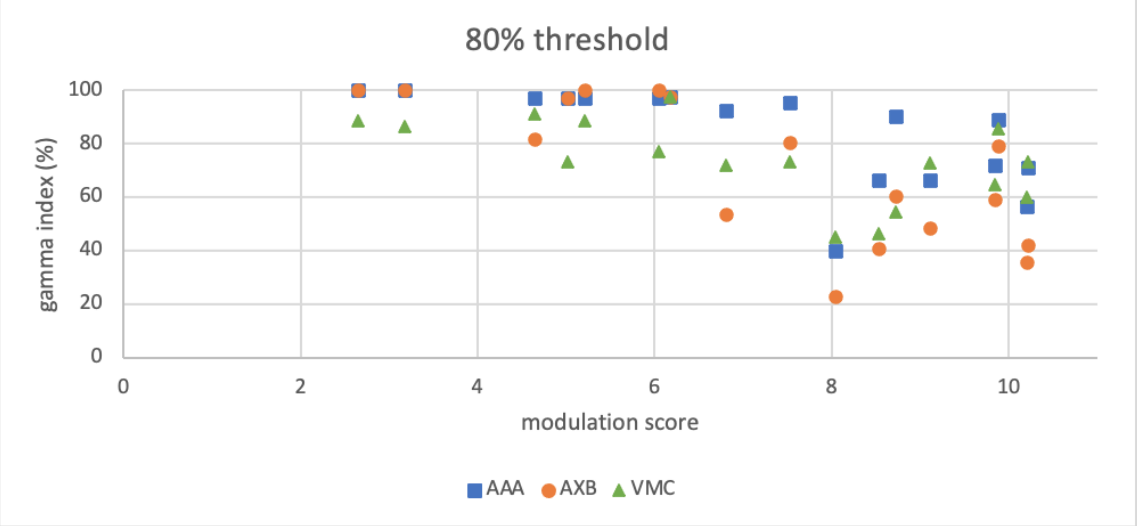

Figure 5.13: 80% threshold, on axis VMAT delivery gamma pass rates as a function of modulation score for 10 MV-FFF beam energy. SMC-AAA—blue square. SMC-AXB—orange circle. SMC-VMC++ —green triangle.

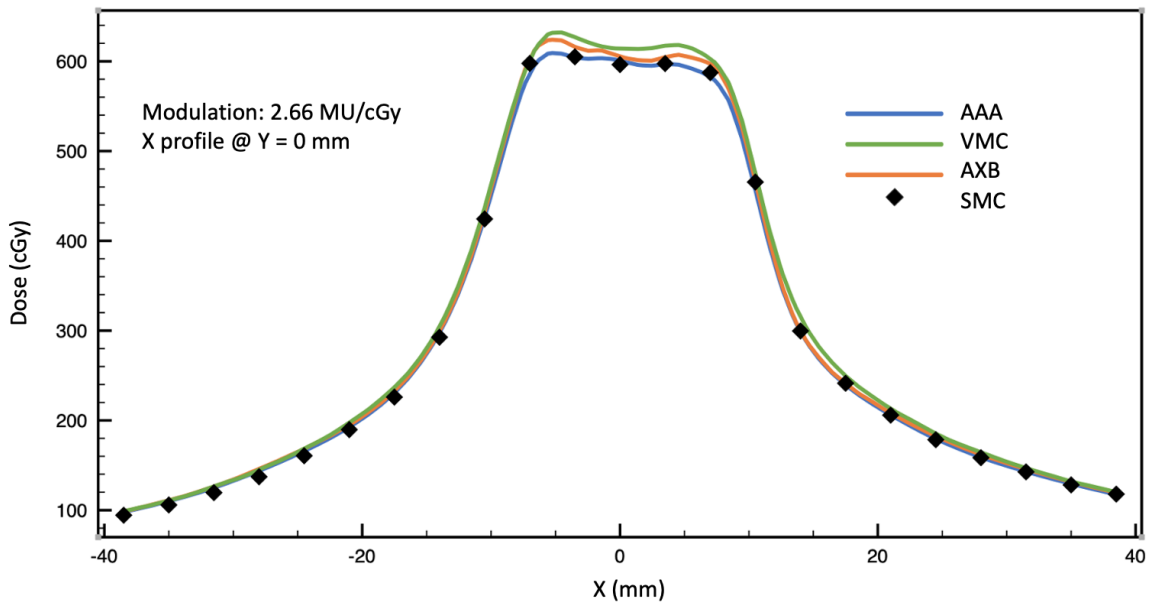

Figure 5.14: Cross plane profiles through the central diode for plan with modulation score of 2.66 MU/cGy (highest gamma pass rates).

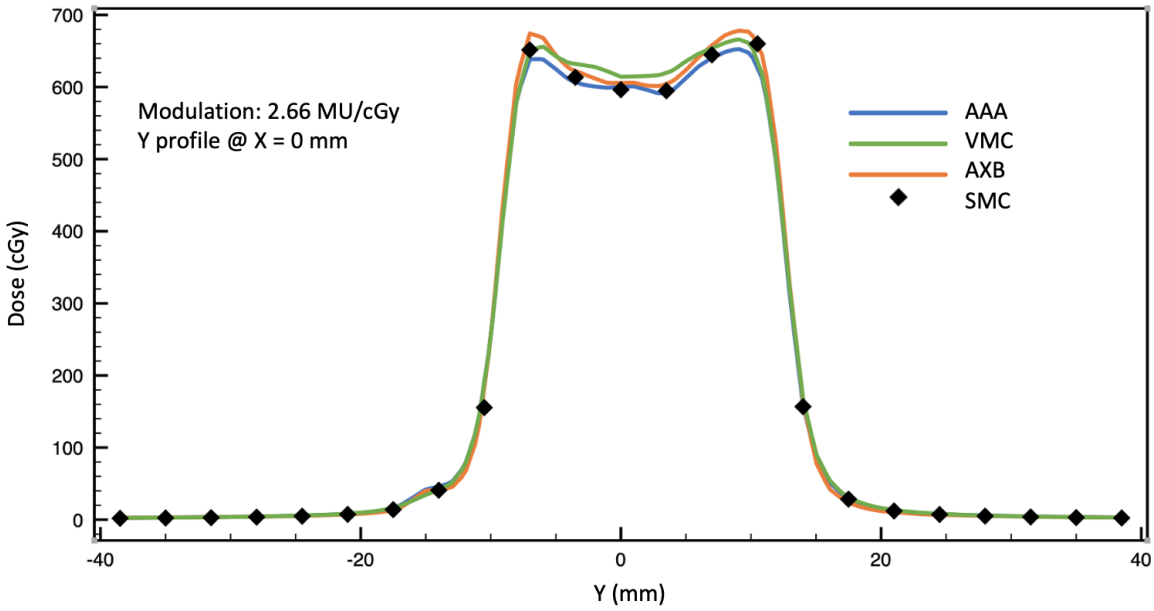

Figure 5.15: In plane profiles through the central diode for plan with modulation score of 2.66 MU/cGy (highest gamma pass rates).

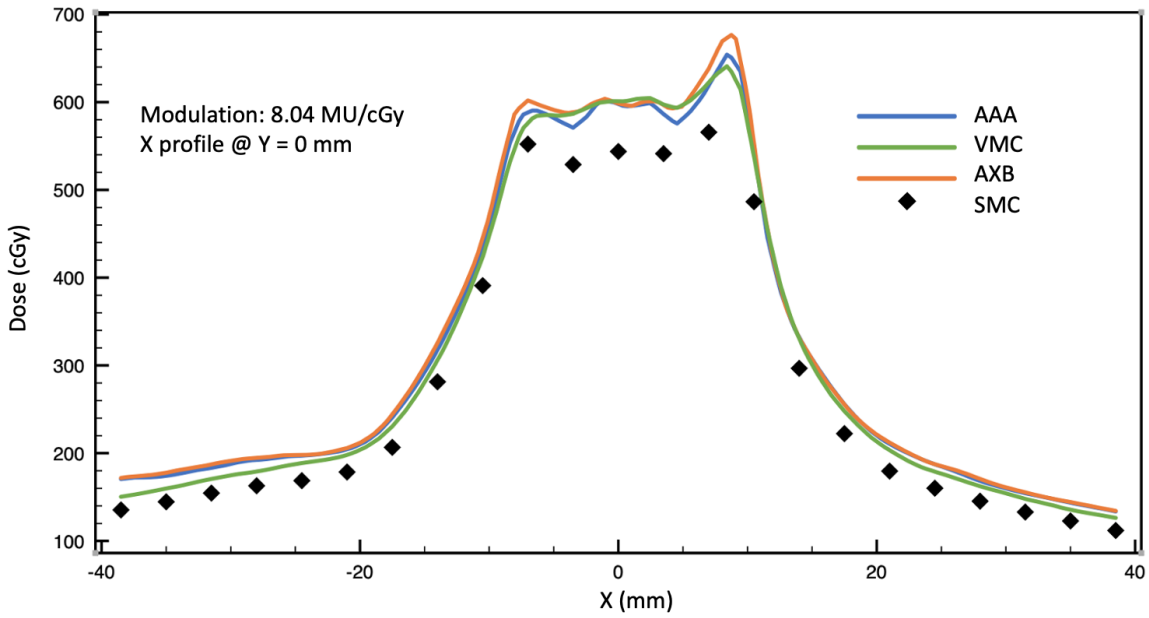

Figure 5.16: Cross plane profiles through the central diode for plan with modulation score of 8.04 MU/cGy (lowest gamma pass rates).

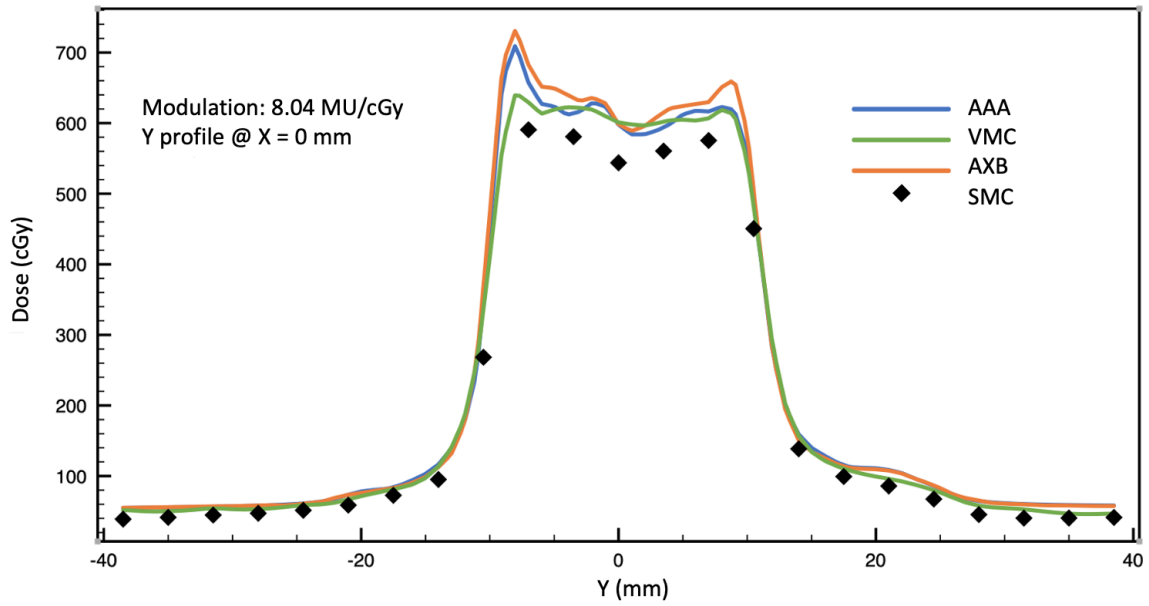

Figure 5.17: In plane profiles through the central diode for plan with modulation score of 8.04 MU/cGy (lowest gamma pass rates).

Off axis VMAT dose distributions

For off axis VMAT delivery, gamma pass rates (3%/1mm) as a function of modulation score are plotted in Figures 5.18 and 5.19. Modulation score ranged from 2.70 to 9.76 MU/cGy. For 10% threshold, gamma pass rates showed a negative correlation with modulation score defined by Pearson's correlation coefficients of 0.55, 0.65, and 0.59 when comparing SMC to AAA, AXB, and VMC++, respectively. All had $p < 0.05$. For 80% threshold, gamma pass rates showed a negative correlation with modulation score defined by Pearson's correlation coefficients of 0.73, 0.81, and 0.55 when comparing SMC to AAA, AXB, and VMC++, respectively. All had $p < 0.05$.

There was no plateau region evident with the off-axis VMAT plans, simply a negative correlation for all modulation scores. Over the entire range, SMC comparison against VMC++ was the best with 45% of all plans passing above 90%. Comparison to AXB showed one plan with gamma pass rate above 90%, which was for the lowest modulation score of 2.70 MU/cGy. Comparison to AAA resulted in two gamma pass rates above 90%, which were for modulation scores of 5.00 MU/cGy and higher. SMC and VMC++ were most consistent for off axis VMAT plans.

Cross plane and in plane profiles for the lowest and highest gamma pass rates associated with off axis VAMT plans can be found in Figures 5.20-5.23. Figure 5.23 shows considerable disagreement in profiles at around -15 mm and +15 mm. In the plan, these regions contain very small MLC openings contributing uncertainty associated with small field dose calculations. A dose measurement with radiochromic film could help determine which dose calculation algorithm is more correct.

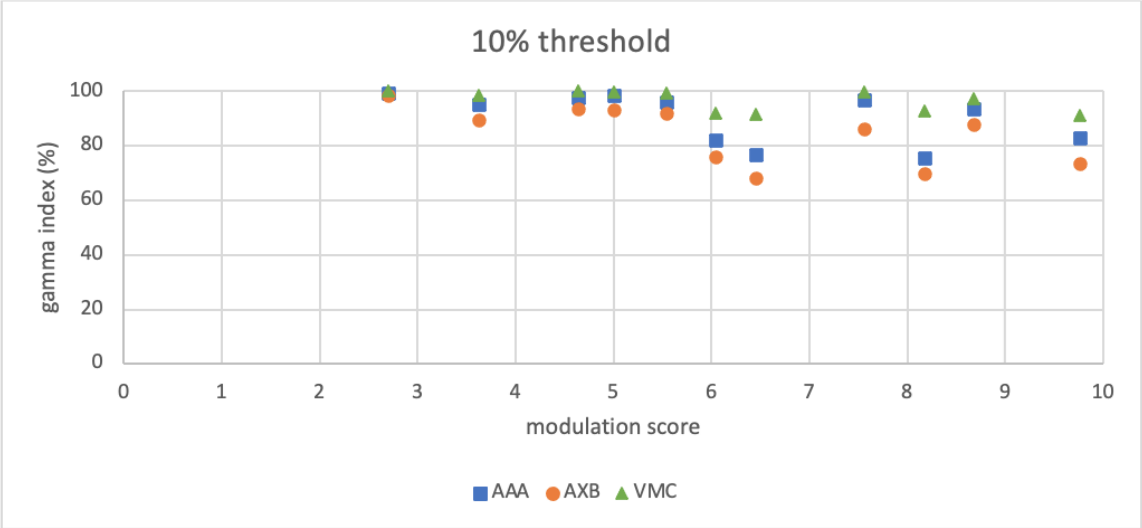

Figure 5.18: 10% threshold, off axis VMAT delivery gamma pass rates as a function of modulation score for 10 MV-FFF beam energy. SMC-AAA—blue square. SMC-AXB—orange circle. SMC-VMC++ —green triangle.

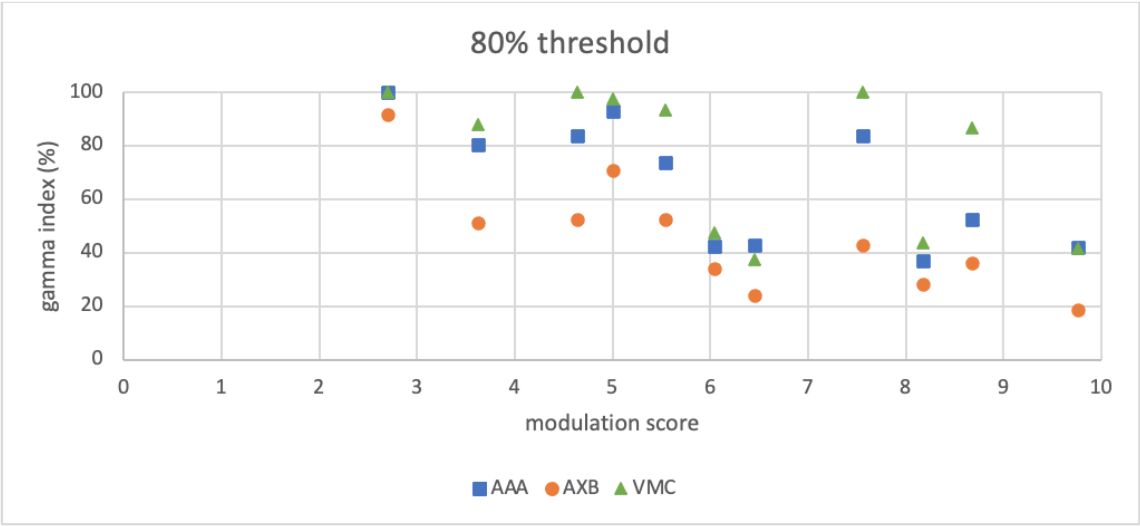

Figure 5.19: 80% threshold, off axis VMAT delivery gamma pass rates as a function of modulation score for 10 MV-FFF beam energy. SMC-AAA—blue square. SMC-AXB—orange circle. SMC-VMC++ —green triangle.

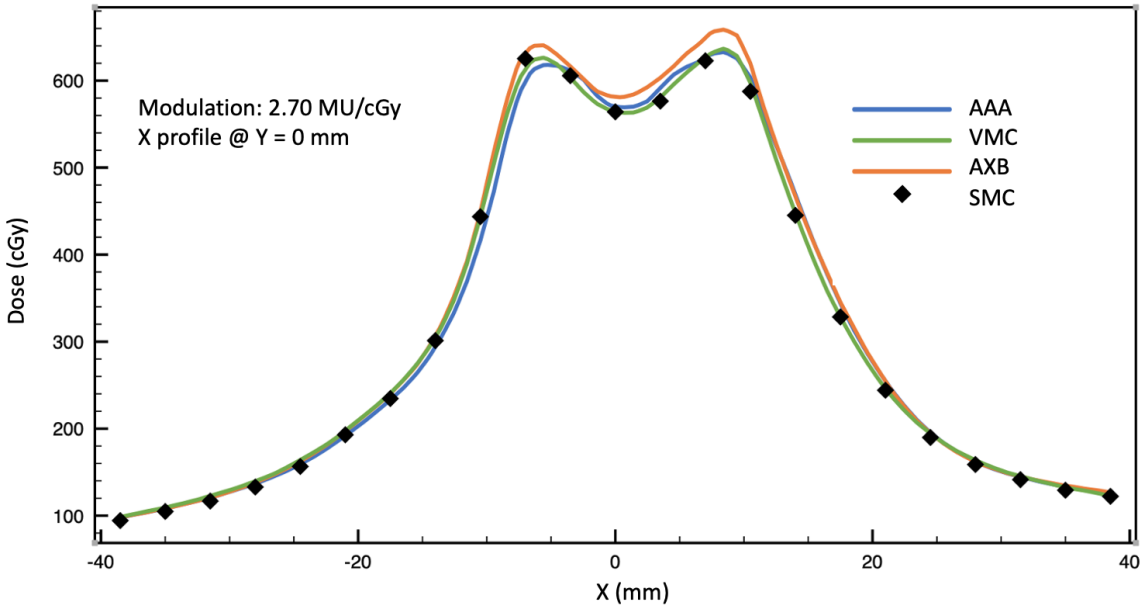

Figure 5.20: Cross plane profiles through the central diode for off axis VMAT plan with modulation score of 2.70 MU/cGy (highest gamma pass rates).

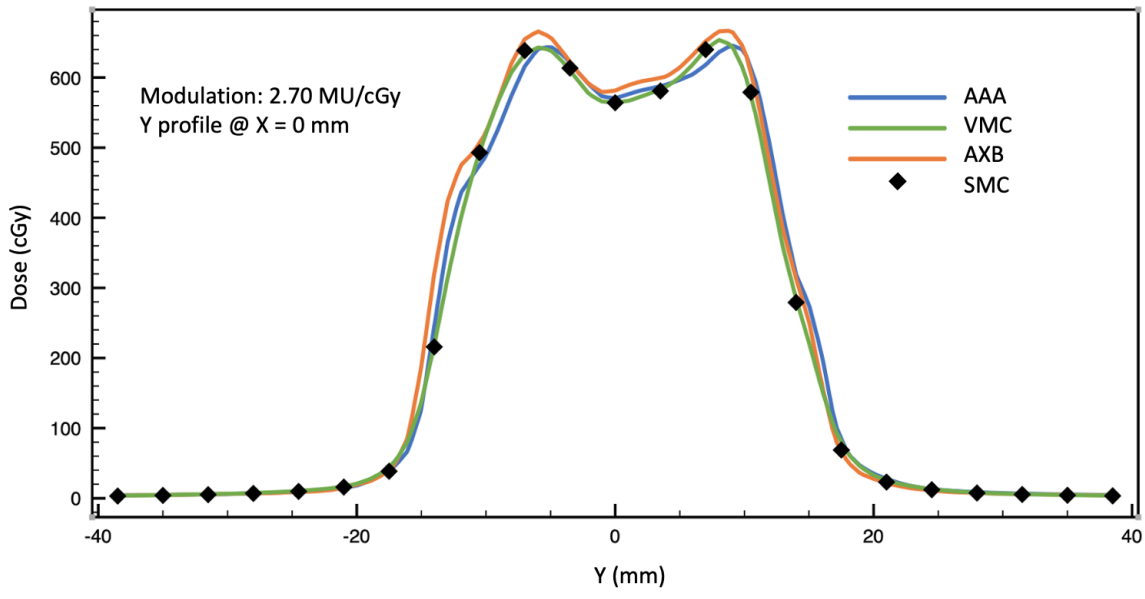

Figure 5.21: In plane profiles through the central diode for off axis VMAT plan with modulation score of 2.70 MU/cGy (highest gamma pass rates).

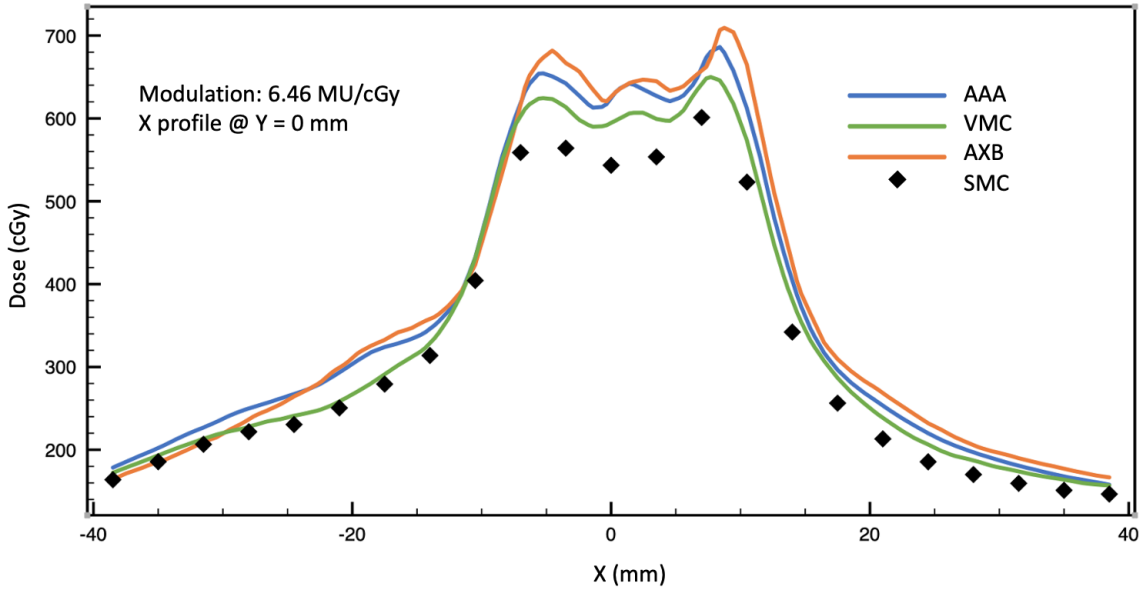

Figure 5.22: Cross plane profiles through the central diode for off axis VMAT plan with modulation score of 6.46 MU/cGy (lowest gamma pass rates).

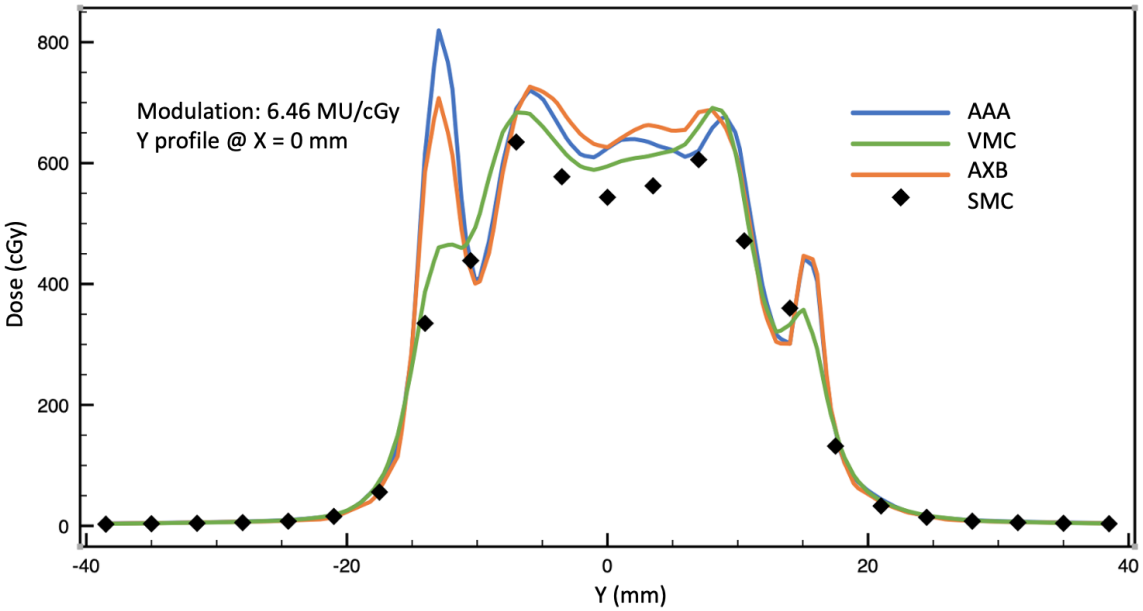

Figure 5.23: In plane profiles through the central diode for off axis VMAT plan with modulation score of 6.46 MU/cGy (lowest gamma pass rates).

Dosimetry comparison for clinical SRS plans

Several clinical SRS plans were chosen based on patient quality assurance tests that showed larger than usual differences between point measurement with microDiamond detector and AAA calculation. SRS plans with point dose percent differences for these plans were in the range of 7.4 - 8.3%, when comparing AAA calculated dose to microdiamond detector measurements, were selected. These differences are on the high end compared to majority of QA results for SRT plans at BC Cancer Victoria center. Despite being high, these differences are deemed acceptable in clinical practice for the PTVs of such small size [75]. These plans have a PTV of about 1 cm and are composed of two VMAT arcs with 10 MV-FFF beam energy. The patient-specific clinical quality assurance measurements are listed in rows 3-6 of Table 1.

A total of six brain SRS patient plans were used to create verification plans on StereoPHAN, which were subsequently delivered to SMC and HYPERSCINT RP-200 (Refer to Chaper 3). Their dose distributions were calculated with AAA, AXB, and VMC++. Point percent differences are listed in Table 5.1. The gamma pass rates (3%/1mm with 80% threshold) are listed in the bottom three rows of Table 5.1. Overall, point dose percent differences were noticeably smaller when comparing SMC to TPS and MC calculated doses (on average less than half) as opposed to clinical quality assurance tests with microdiamond comparison to TPS and MC calculated doses. Of the six selected patient plans, three exhibit passing gamma rates. Normally, IAEA recommends that measured dose, as part of quality assurance, be within 5% of the prescribed dose to the PTV. Based on this criteria, all six patient plans passed when comparing SMC dose to AAA or VMC++ dose, four passed when comparing SMC dose to HYPERSCINT measurements, and three passed when comparing SMC to AXB.

Cross plane and in plane profiles are plotted for patients B (high gammas pass rates) in Figures 5.24 and 5.25 and for patient E (failing gamma pass rates) in Figures 5.26 and 5.27.

Table 5.1: Summary of brain SRS patient dose comparisons between various dosimetry methods, includes point dose percent differences and gamma pass rates (3%/1mm, 80% threshold).

Patient	A	B	C	D	E	F
PTV Size	1.0	0.7	1.2	0.8	0.6	1.0
Modulation Score (MU/cGy)	2.1	2.1	2.0	2.2	2.1	2.0
point dose % diff (AAA-mDD)	-7.4	-7.5	-8.3	-7.4	-8.1	-7.4
point dose % diff (MC-AAA)	3.4	–	2.0	2.5	2.9	3.1
point dose % diff (MC-mDD)	-4.3	–	-6.5	-5.1	-5.5	-4.6
point dose % diff (MC-AXB)	3.4	–	2.8	3.1	1.7	0.8
point dose % diff (SMC-AAA)	1.2	-1.0	-2.90	-3.4	-3.6	-3.1
point dose % diff (SMC-AXB)	0.4	-4.3	-2.7	-8.2	-7.2	-7.1
point dose % diff (SMC-VMC)	4.3	-2.4	-1.5	-4.5	-3.6	-2.5
point dose % diff (SMC-HS)	4.4	-5.3	–	-3.2	-1.2	-3.2
γ (SMC-AAA)	94.1	90.0	100.0	90.0	75.0	81.8
γ (SMC-AXB)	94.1	80.0	100.0	60.0	57.1	70.0
γ (SMC-VMC)	94.1	90.0	100.0	77.8	75	100.0

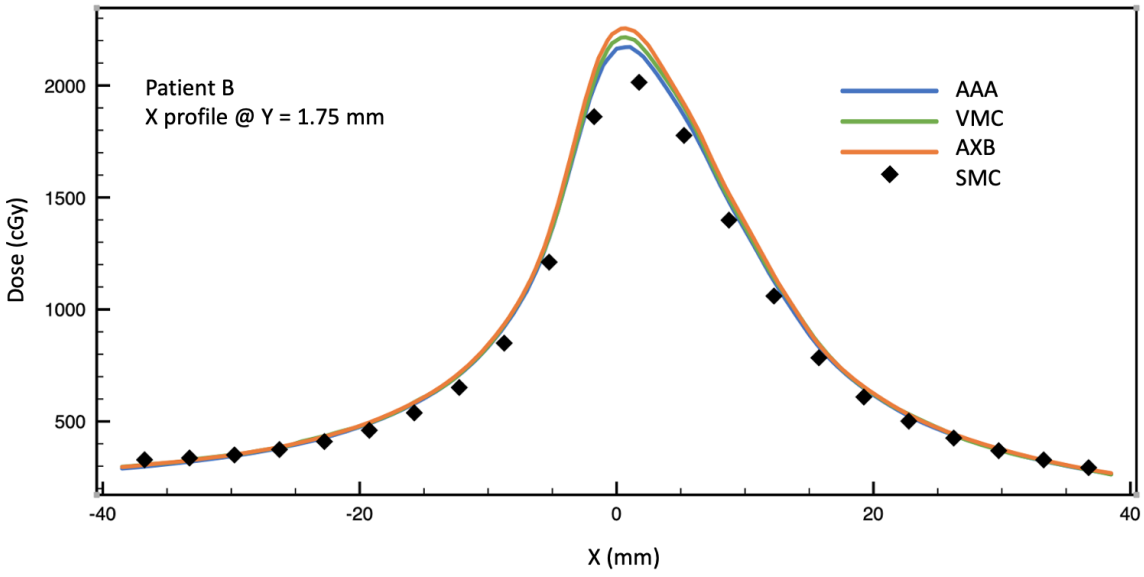

Figure 5.24: Cross plane (taken at Y = 1.75 mm) profiles through patient B.

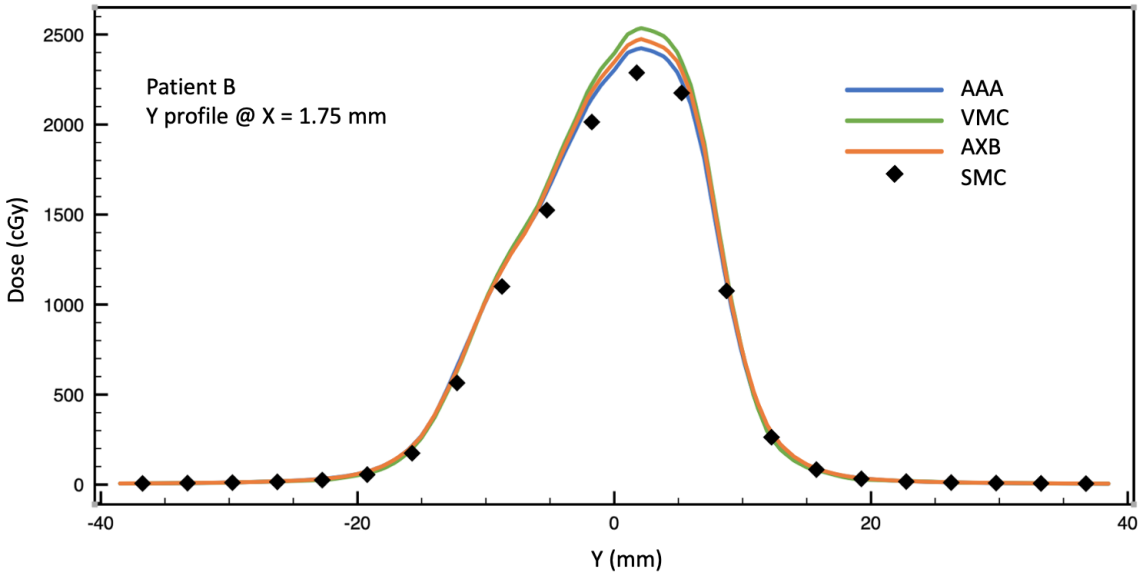

Figure 5.25: In plane (taken at X = 1.75 mm) profiles through patient B.

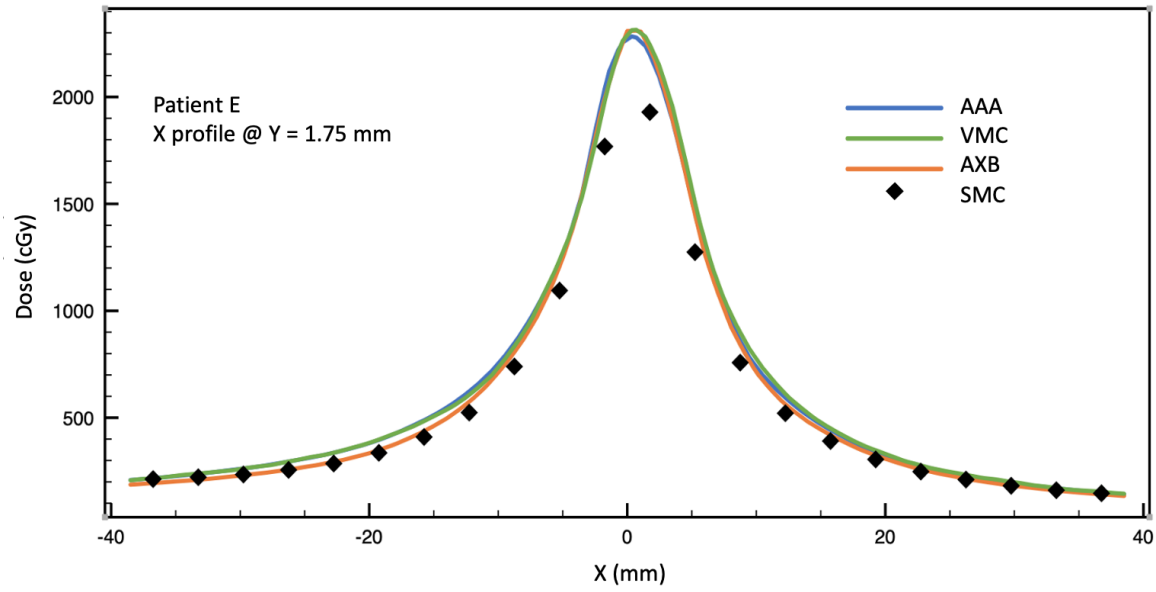

Figure 5.26: Cross plane (taken at Y = 1.75 mm) profiles through patient E.

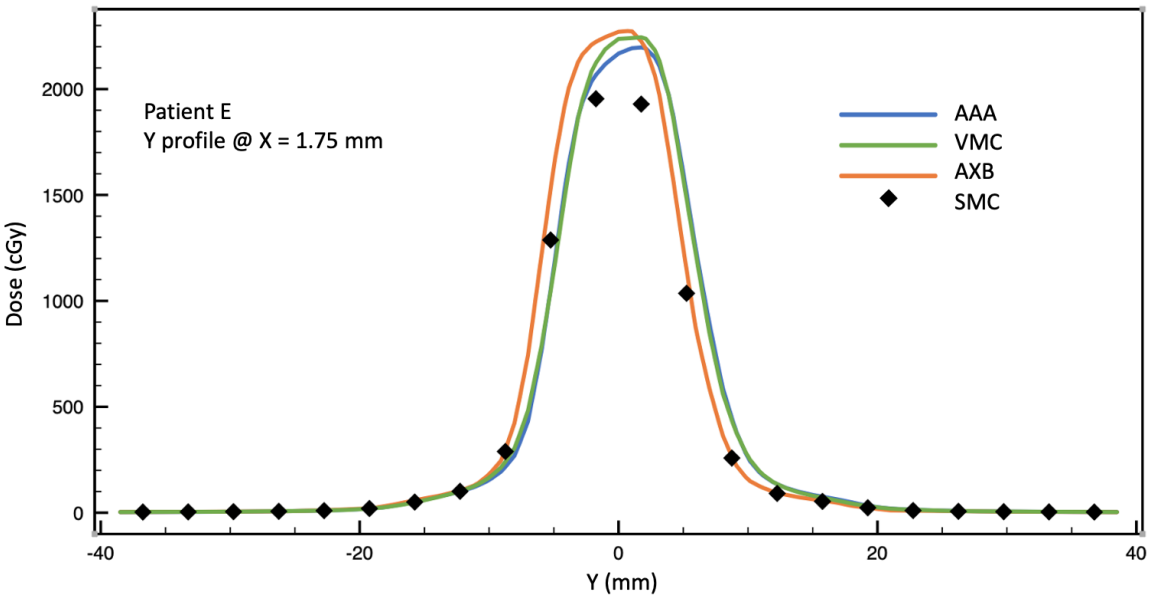

Figure 5.27: In plane (taken at X = 1.75 mm) profiles through patient E.

5.4 Discussion

SRS MapCHECK (SMC), a patient-specific quality assurance tool, has been evaluated under clinically challenging conditions. This detector array is diode-based with applied correction factors to account for diode response dependence on spectral changes. The dosimetric characterization of SMC in this work evaluated how well these correction factors performed under dosimetrically challenging conditions such as small fields and off axis measurements, both of which alter the energy spectrum of incident photons. SMC was compared against treatment planning system algorithms AAA and AXB, against Monte Carlo code VMC++, and against experimental measurements with HYPERSCINT RP-200 scintillation dosimetry system highlighting deviations in dose as field conditions become more challenging.

5.4.1 Static fields

Point dose measurements at the center of the field for varying field sizes indicate good agreement between all methods from 5 x 5 cm^2 down to 1 x 1 cm^2 field size where all point dose differences fall within about 4% of each other for 6 MV energy. For 10 MV-FFF energy beam, differences are within 8% of each other down to 1 x 1 cm^2. For smaller fields, larger dosimetric deviations begin to emerge with about 10-15% differences at 0.5 x 0.5 cm^2 to about 20% at 0.16 x 0.16 cm^2. This trend is applicable to both 6 MV and 10 MV-FFF energy beams. These results are consistent with those obtained in Chapter 4. Recall, the output factors measured with SMC agreed within 1% to those measured or calculated by other methods for field sizes down to 1 x 1 cm^2, about 12% difference at 0.5 x 0.5 cm^2. Thus, SMC small field correction factors are valid at 1 x 1 cm^2 and 2 x 2 cm^2 field sizes for 6 MV and 10 MV-FFF energy beams, respectively. Measurements can be trusted at these field sizes or larger. For smaller fields, dose differences are significant and applied correction factors should be investigated further by the manufacturer. A possible explanation for the large differences seen at very small fields, less than 0.5 x 0.5 cm^2, could be positional difficulties. The central diode needs to be placed directly in the center of the field, which is quite difficult to accomplish with sub-millimetric accuracy. Additionally, small field correction factors for SMC are applied based on the number of diodes irradiated, thus if a single diode is irradiated, the same small field correction factor will be applied regardless of the actual field size, further explaining the differences seen at very small fields.

Profile results (Figures 5.7 and 5.8) for multi-target small fields (single leaf pair separated by 10, 20, 30, or 40 mm) indicate that SMC performs well for static fields in terms of dose registration and alignment. However, it should be noted that due to diode spacing of 3.5 mm in X and Y directions (and 2.5 mm at 45 degree angles), a single diode could easily miss such a small field entirely or catch just the penumbra of that field. This could result in reporting of underestimated absolute dose if not verified by other means. In those profiles, a diode is positioned at the peak of the dose profile in roughly half of the fields. Thus, a secondary measurement is recommended if user would intend to report absolute dose values for small fields.

Measurements appear to be independent of collimator angle when considering 0 or 90 degree rotation. The point dose percent differences between central diode of SMC and other methods were tighter at isocenter compared to those of central diode shifted 6 cm laterally or in the superior-inferior direction. Ahmed et al. [3] investigated central diode and off axis diode (up to 3 cm) measurements for an 8 x 8 cm^2 field size with 6 MV energy beam. They evaluated percent difference between SMC central diode and Exradin W1 scintillator detector (Standard Imaging Inc., Middleton, WI, USA), and found a spread of about 4% for isocentric fields and about 3% for off axis fields. Results in the present study confirm these findings as percent differences were about 1-4% for field sizes of 1 x 1 cm^2 and 2 x 2 cm^2 for 6 MV energy beam. However, the smaller field size of 0.5 x 0.5 cm^2 had a spread of point dose percent differences over 10%. This is larger than found at isocenter, therefore a combination of small field effects and off axis effects must be contributing to uncertainties.

5.4.2 VMAT fields

While high modulation plans are able to generate sharper dose gradients and better dose conformity than standard cone collimators, they are associated with lower gamma pass rates [17], [74], [108]. Higher degrees of modulation are typically accompanied by larger numbers of small fields contained in the target volume causing concerns with modeling and measurement.

Gamma pass rates (3%/1mm) showed negative correlation with modulation score. For 10% threshold, Pearson's correlation coefficients (R) were 0.54, 0.67, and 0.60 when comparing SMC to AAA, AXB, and VMC++, respectively. For 80% threshold, Pearson's correlation coefficients were 0.67, 0.75, and 0.56 when comparing SMC to AAA, AXB, and VMC++, respectively. These R values indicate a moderate strength

correlation. More data points could be useful in establishing a concrete relationship between gamma pass rate and modulation score. The 80% threshold dataset has a strong correlation between pass rate and modulation. For 10% threshold, the correlation was lower and pass rates are consistently high, which may provide a false sense of security. This is because utilizing 10% threshold masks differences in high dose regions as it averages the pass rates over the high and low dose regions. Low dose regions, on most occasions, are far less important than the dose to the tumour. Therefore, 80% is a much better threshold to consider as this dose region is where dose distribution is closest to the prescribed dose.

While comparing SMC to film and TPS, Rose et al. found that gamma pass rates (3%/1mm with 10% threshold) begin to fail at modulation scores just over 5 MU/cGy. In this study, considering 10% threshold, gamma pass rates begin to fail (score less than 90%) at modulation scores of 8.0 MU/cGy when comparing SMC to AAA and AXB, while for VMC++ gamma pass rates did not fail for modulation scores up to 10.1 MU/cGy. For 80% threshold, gamma pass rates begin to fail at 8.0 MU/cGy comparing SMC to AAA, at 6.0 MU/cGy for SMC to AXB, and at 2.6 MU/cGy for SMC to VMC++ comparision.

Part of the reasoning for lack of a strong correlation between gamma pass rates and modulation score could be related to the simplistic form of defining modulation score. This crude definition of MU/cGy mostly likely picks up the main trend, but misses the intricacies of specific dose delivery. For example, a plan can have many small fields and a few large fields, which are well understood and deliver more MUs, artificially lowering the modulation score for the plan. This plan will have a lower gamma pass rate due to presence of many small fields, and yet a low modulation score, thus skewing the correlation. More advanced methodology related to evaluating the interleaf spacing throughout VMAT delivery to estimate distribution of apertures could shed more light on this relationship. A more advanced definition of modulation would involve analyzing MLC files to build a probability distribution of field sizes, which is outside the scope of this thesis, but could be considered in future investigations.

Off axis VMAT delivery showed even stronger negative correlations between 80% threshold gamma pass rates (3%/1mm) and modulation scores, and much lower pass rates overall. Average gamma pass rates dropped from 86-98% to 46-76%. Considering the wide spread of point dose differences for 0.5 x 0.5 cm^2 off axis fields, as reported in this study, such a trend makes sense.

5.4.3 Clinical SRS plans

Four, out of the six challenging patient plans, have over 90% pass rate when considering gamma criteria of 3%/1mm and 80% threshold between SMC and AAA. The same result was seen for comparison of SMC and VMC++. Results for AXB were inferior, and this is commented in Conclusions below. In our opinion, SMC has a limitation on the size of the dose distribution that it can examine accurately via gamma index and provide pass statistics. Due to detector spacing of 2.5 mm the limit is likely to be just under 1 cm diameter. For the fields of less than 1 cm diameter we would recommend using SMC as a point dose detector, and it performs as such reasonably well, similar to other available small field detectors.

Percent point dose differences of SMC – AAA result in 50% of plans passing 3% criteria, and all are within 4%. Agreement of SMC with MC calculations is similar, though point dose difference is somewhat higher. Point dose for all plans is within 5%, which is acceptable for such small SRT deliveries. Agreement of SMC with AXB is not as good, this is likely due to inferior source model in AXB algorithm, as further on commented below in Conclusions section. Agreement with HYPERSCINT measurements is within 5% for all but one plan, which is reasonable, though not as good as we expected. This result is rather surprising considering the excelling dosimetric properties of HYPERSCINT and SRS MapCHECK as evaluated in Chapters 3 and 4. Some of this difference could be attributed to non-linearity of HYPERSCINT dose response at the low dose end, reported in Chapter 3. Medscint notified us that this issue will be addressed in the next update of the system.

5.5 Conclusions

SRS MapCHECK has been evaluated under dosimetrically challenging conditions with a particular focus on small and off axis fields, or a combination of the two. It was also evaluated for highly modulated isocentric and off axis VMAT plans. The limitations of this device were determined to be very small fields and highly modulated plans—especially off axis. This is likely due to uncertainties of measurements in fields smaller than 1 x 1 cm^2 combined with the coarse diode spacing of the array. In such situations, the diode array could potentially be missing high dose regions of small fields. SMC can be used, with confidence, for patient specific quality assurance of stereotactic VMAT plans with modulation scores less than 5 MU/cGy. Despite

these limitations, overall, SRS MapCHECK demonstrated excellent results when used within scenarios as applicable to current clinical practice. In most clinical situations it is an efficient end-to-end patient specific quality assurance tool, as long as appropriate dose threshold of around 80% is used.

BC Cancer Victoria clinical SRT group consensus, based on previous experience, is to avoid treatments with modulation scores greater than five, and this study confirms that this is a reasonable practice.

Results of this chapter showed that AXB algorithm demonstrated inferior performance compared to other algorithms included in this study, despite the general consensus that conceptually this algorithm should be as good as Monte Carlo for particle transport in the phantom. The reason for this poorer performance of AXB is commissioning of the source model for this algorithm. This model was commissioned clinically without specific attention to modeling of small fields. Therefore, this study highlights, again, the importance of small field modeling for clinical algorithms used in SRT planning.

Chapter 6

Conclusions

The work in this thesis was driven by the difficulties associated with experimental and computational dosimetry under small field conditions. Accurate dose assessment under these conditions is imperative to ensuring positive patient outcomes during radiotherapy treatments. To advance knowledge in this field, this thesis investigated the performance of two novel small field dosimeters. The characterization for a scintillation-based point dosimeter, HYPERSCINT RP-200, showed that this dosimeter performs well in small fields and can potentially be used for dose validation purposes. Dose non-linearity was observed for low doses of about 2.5 cGy, potentially limiting the use of HYPERSCINT RP-200 for VMAT plan verification. Additionally, dosimetry for fields smaller than 1 x 1 cm^2 should be performed with at least two different dosimeters to ensure accuracy as small field correction factors may be required for HYPERSCINT under these fields. SRS MapCHECK, a diode-based detector array, was also dosimetrically characterized showing to be a sufficient dosimeter for field sizes of 1 x 1 cm^2 and larger under normal clinical conditions. This thesis also provided dose comparisons between SRS MapCHECK, treatment planning system algorithms AAA and AXB, Monte Carlo algorithm VMC++, and HYPERSCINT RP-200 for small fields and off axis fields, as well as highly modulated VMAT plans and clinical SRT plans, with the intention of finding areas of divergence. Good agreement was seen between SRS MapCHECK, AAA, and VMC++ for isocentric clinical SRT dose delivery with targets around 2 cm in diameter and modulation scores of around 5 MU/cGy. Noticeable disagreements in dose distributions begin to emerge with fields smaller than 1 x 1 cm^2, modulation scores above 5 MU/cGy, and/or VMAT delivery off axis. These are important limitations to keep in mind for clinical radiotherapy treatment plan verification and patient specific quality assurance.

Bibliography

[1] *Dosimetry of Small Static Fields Used in External Beam Radiotherapy*. Number 483 in Technical Reports Series. INTERNATIONAL ATOMIC ENERGY AGENCY, Vienna, 2017.

[2] F Abolaban, S Zaman, J Cashmore, A Nisbet, and CH Clark. Changes in patterns of intensity-modulated radiotherapy verification and quality assurance in the uk. *Clinical Oncology*, 28(8):e28–e34, 2016.

[3] S Ahmed, G Zhang, EG Moros, and V Feygelman. Comprehensive evaluation of the high-resolution diode array for SRS dosimetry. *J. Appl. Clin. Med. Phys.*, 20(10):13–23, October 2019.

[4] A Ahnesjö, P Andreo, and A Brahme. Calculation and application of point spread functions for treatment planning with high energy photon beams. *Acta Oncol.*, 26(1):49–56, January 1987.

[5] R Alfonso, P Andreo, R Capote, M Saiful Huq, W Kilby, P Kjäll, T R Mackie, H Palmans, K Rosser, J Seuntjens, W Ullrich, and S Vatnitsky. A new formalism for reference dosimetry of small and nonstandard fields. *Med. Phys.*, 35(11):5179–5186, November 2008.

[6] E Alhakeem and S Zavgorodni. Output and $(k^{f_{\mathrm{clin}},f_{\mathrm{msr}}}_{Q_{\mathrm{clin}},Q_{\mathrm{msr}}})$ correction factors measured and calculated in very small circular fields for microdiamond and EFD-3G detectors. *Phys. Med. Biol.*, 63(15):155002, July 2018.

[7] T Aoyama, S Koyama, M Tsuzaka, and H Maekoshi. A depth-dose measuring device using a multichannel scintillating fiber array for electron beam therapy. *Med. Phys.*, 24(8):1235–1239, August 1997.

[8] M Ashburner and K Mugabe. Clinical experience using the srs mapcheck for patient specific plan verification of flattening filter free, non-coplanar stereotactic brain plans using hyperarc. 2021.

[9] M M Aspradakis, J P Byrne, H Palmans, J Conway, K Rosser, J A P Warrington, and S Duane. *Small field MV photon dosimetry. IPEM.* 2010.

[10] C Audet, B A Poffenbarger, P Chang, P S Jackson, R E Lundahl, S I Ryu, and Gordon R Ray. Evaluation of volumetric modulated arc therapy for cranial radiosurgery using multiple noncoplanar arcs. *Med. Phys.*, 38(11):5863–5872, November 2011.

[11] H Bagheri, A Soleimani, N Gharehaghaji, A Mesbahi, F Manouchehri, B Shekarchi, B Dormanesh, and H A Dadgar. An overview on small-field dosimetry in photon beam radiotherapy: Developments and challenges. *J. Cancer Res. Ther.*, 13(2):175–185, April 2017.

[12] C Bassinet, C Huet, S Derreumaux, G Brunet, M Chéa, M Baumann, T Lacornerie, S Gaudaire-Josset, F Trompier, P Roch, G Boisserie, and I Clairand. Small fields output factors measurements and correction factors determination for several detectors for a CyberKnife® and linear accelerators equipped with microMLC and circular cones. *Med. Phys.*, 40(7):071725, July 2013.

[13] A S Beddar, T Mackie, R, and F H Attix. Water-equivalent plastic scintillation detectors for highenergy beam dosimetry: I. physical characteristics and theoretical consideration. *Phys. Med. Biol*, 37:1883–1900, 1992.

[14] A S Beddar, T R Mackie, and F H Attix. Water-equivalent plastic scintillation detectors for high-energy beam dosimetry: Ii. properties and measurements. *Physics in Medicine & Biology*, 37(10):1901, 1992.

[15] J L Bedford. Calculation of absorbed dose in radiotherapy by solution of the linear boltzmann transport equations. *Phys. Med. Biol.*, 64(2):02TR01, January 2019.

[16] H Bekerat, S Devic, F DeBlois, K Singh, A Sarfehnia, J Seuntjens, S Shih, X Yu, and D Lewis. Improving the energy response of external beam therapy (ebt) gafchromictm dosimetry films at low energies ($\leq$ 100 kev). *Medical physics*, 41(2):022101, 2014.

[17] E T Bender. Increasing dose gradient and uniformity in small fields using modulation: theory and prototypes for cone-based stereotactic radiosurgery. *Med. Phys.*, 41(5):051706, May 2014.

[18] M.J. Berger, J.S. Coursey, M.A. Zucker, and J. Chang. Estar, pstar, and astar: Computer programs for calculating stopping-power and range tables for electrons, protons, and helium ions (version 1.2.3). http://physics.nist.gov/Star, 2005.

[19] J B Birks. *The theory and practice of scintillation counting: International series of monographs in electronics and instrumentation*, volume 27. Elsevier, 2013.

[20] T Bortfeld, W Schlegel, and B Rhein. Decomposition of pencil beam kernels for fast dose calculations in three-dimensional treatment planning. *Med. Phys.*, 20(2 Pt 1):311–318, March 1993.

[21] H Bouchard, Y Kamio, H Palmans, J Seuntjens, and S Duane. Detector dose response in megavoltage small photon beams. II. pencil beam perturbation effects. *Med. Phys.*, 42(10):6048–6061, October 2015.

[22] L Brualla, M Rodriguez, and A M Lallena. Monte carlo systems used for treatment planning and dose verification. *Strahlenther. Onkol.*, 193(4):243–259, April 2017.

[23] S Buranurak, C E Andersen, A R Beierholm, and L R Lindvold. Temperature variations as a source of uncertainty in medical fiber-coupled organic plastic scintillator dosimetry. *Radiation Measurements*, 56:307–311, 2013.

[24] K Bush, R Townson, and S Zavgorodni. Monte carlo simulation of rapidarc radiotherapy delivery. *Physics in Medicine & Biology*, 53(19):N359, 2008.

[25] P Carrasco, N Jornet, O Jordi, M Lizondo, A Latorre-Musoll, T Eudaldo, A Ruiz, and M Ribas. Characterization of the exradin W1 scintillator for use in radiotherapy. *Med. Phys.*, 42(1):297–304, January 2015.

[26] I J Chetty, B Curran, J E Cygler, J J DeMarco, G Ezzell, B A Faddegon, I Kawrakow, P J Keall, H Liu, C M C Ma, D W O Rogers, J Seuntjens, D Sheikh-Bagheri, and J V Siebers. Report of the AAPM task group no. 105: Issues associated with clinical implementation of monte carlo-based photon

and electron external beam treatment planning. *Med. Phys.*, 34(12):4818–4853, December 2007.

[27] G M Clark, R A Popple, P E Young, and J B Fiveash. Feasibility of single-isocenter volumetric modulated arc radiosurgery for treatment of multiple brain metastases. *Int J Radiat Oncol Biol Phys*, 76(1):296–302, 2010.

[28] R F W Coates, G J Janacek, and K V Lever. Monte carlo simulation and random number generation. *IEEE j. sel. areas commun.*, 6(1):58–66, 1988.

[29] G Cranmer-Sargison, P H Charles, J V Trapp, and D I Thwaites. A methodological approach to reporting corrected small field relative outputs, radiother. *Radiother. Oncol*, 109:350–355, 2013.

[30] G Cranmer-Sargison, S Weston, Nr P Sidhu, and D I Thwaites. Experimental small field 6 MV output ratio analysis for various diode detector and accelerator combinations. *Radiother. Oncol.*, 100(3):429–435, September 2011.

[31] M Dalaryd, T Knöös, and C Ceberg. Combining tissue-phantom ratios to provide a beam-quality specifier for flattening filter free photon beams. *Med. Phys.*, 41(11):111716, November 2014.

[32] I J Das, M B Downes, A Kassaee, and Z Tochner. Choice of radiation detector in dosimetry of stereotactic radiosurgery-radiotherapy. *J Radiosurg*, 3:177–185, 2000.

[33] I J Das, J Morales, and P Francescon. Small field dosimetry: What have we learnt? 2016.

[34] C De Angelis, S Onori, M Pacilio, G A P Cirrone, G Cuttone, L Raffaele, M Bucciolini, and S Mazzocchi. An investigation of the operating characteristics of two PTW diamond detectors in photon and electron beams. *Med. Phys.*, 29(2):248–254, February 2002.

[35] S B C Debnath, D Tonneau, C Fauquet, A Tallet, A Goncalves, and J Darreon. Dosimetric characterization of a small-scale (Zn,Cd)S:Ag inorganic scintillating detector to be used in radiotherapy. *Phys. Med.*, 84:15–23, April 2021.

[36] S Devic. Radiochromic film dosimetry: past, present, and future. *Phys. Med.*, 27(3):122–134, July 2011.

[37] S Devic, N Tomic, and D Lewis. Reference radiochromic film dosimetry: review of technical aspects. *Physica Medica*, 32(4):541–556, 2016.

[38] C Fiandra, U Ricardi, R Ragona, S Anglesio, F Romana Giglioli, E Calamia, and F Lucio. Clinical use of ebt model gafchromic™ film in radiotherapy. *Medical physics*, 33(11):4314–4319, 2006.

[39] B D Flury. Acceptance–rejection sampling made easy. *SIAM Rev. Soc. Ind. Appl. Math.*, 32(3):474–476, September 1990.

[40] J M Fontbonne, G Iltis, G Ban, A Battala, J C Vernhes, J Tillier, N Bellaize, C Le Brun, B Tamain, K Mercier, and J C Motin. Scintillating fiber dosimeter for radiation therapy accelerator. *IEEE Trans. Nucl. Sci.*, 49(5):2223–2227, October 2002.

[41] I M Gagné and S Zavgorodni. Evaluation of the analytical anisotropic algorithm in an extreme water–lung interface phantom using monte carlo dose calculations. *Journal of Applied Clinical Medical Physics*, 8(1):33–46, 2007.

[42] P E Galavis, L Hu, S Holmes, and I J Das. Characterization of the plastic scintillation detector exradin W2 for small field dosimetry. *Med. Phys.*, 46(5):2468–2476, May 2019.

[43] J Gardner, J Siebers, and I Kawrakow. Dose calculation validation of vmc++ for photon beams. *Med. Phys.*, 34(5):1809–1818, May 2007.

[44] M Guillot, L Gingras, L Archambault, S Beddar, and L Beaulieu. Spectral method for the correction of the cerenkov light effect in plastic scintillation detectors: a comparison study of calibration procedures and validation in cerenkov light-dominated situations. *Med. Phys.*, 38(4):2140–2150, April 2011.

[45] P H Halvorsen, E Cirino, I J Das, J A Garrett, J Yang, F Yin, and L A Fairobent. AAPM-RSS medical physics practice guideline 9.a. for SRS-SBRT. *J. Appl. Clin. Med. Phys.*, 18(5):10–21, September 2017.

[46] G Heilemann, B Poppe, and W Laub. On the sensitivity of common gamma-index evaluation methods to MLC misalignments in rapidarc quality assurance. *Med. Phys.*, 40(3):031702, March 2013.

[47] J H Hubbell. Photon cross sections, attenuation coefficients and energy absorption coefficients. *National Bureau of Standards Report NSRDS-NBS29*, 1969.

[48] J H Hubbell. Experimentally measured total x-ray attenuation coefficients extracted from previously unprocessed documents held by the nist photon and charged particle data center. 9 1996.

[49] M Hussein, C H Clark, and A Nisbet. Challenges in calculation of the gamma index in radiotherapy-towards good practice. *Physica Medica*, 36:1–11, 2017.

[50] IAEA. Dosimetry of small static fields used in external beam radiotherapy. `https://www.iaea.org/publications/11075/dosimetry-of-small-static-fields-used-in-external-beam-radiotherapy`, August 2016. Accessed: 2022-11-23.

[51] TR IEC. 60788: 2004 medical electrical equipment-glossary of defined terms. *International Electro-technical Commission, Switzerland Geneva*, 2004.

[52] E Jean, F Therriault-Proulx, and L Beaulieu. Comparative optic and dosimetric characterization of the HYPERSCINT scintillation dosimetry research platform for multipoint applications. *Phys. Med. Biol.*, 66(8):085009, April 2021.

[53] H E Johns and J R Cunningham. The physics of radiology. 1983.

[54] P A Jursinic, R Sharma, and J Reuter. MapCHECK used for rotational IMRT measurements: step-and-shoot, tomotherapy. RapidArc. *Med Phys*, 37(6):2837–2846, 2010.

[55] I Kawrakow. VMC++, electron and photon monte carlo calculations optimized for radiation treatment planning. In *Advanced Monte Carlo for Radiation Physics, Particle Transport Simulation and Applications*, pages 229–236. Springer Berlin Heidelberg, Berlin, Heidelberg, 2001.

[56] I Kawrakow and A F Bielajew. On the condensed history technique for electron transport. *Nucl. Instrum. Methods Phys. Res. B*, 142(3):253–280, July 1998.

[57] I Kawrakow and M Fippel. Investigation of variance reduction techniques for monte carlo photon dose calculation using XVMC. *Phys. Med. Biol.*, 45(8):2163–2183, August 2000.

[58] I Kawrakow and M Fippel. Proceedings of the 22nd annual international conference of the IEEE. pages 1490–1493, 2000.

[59] I Kawrakow, M Fippel, and K Friedrich. 3D electron dose calculation using a voxel based monte carlo algorithm (VMC). *Med. Phys.*, 23(4):445–457, April 1996.

[60] P J Keall, J V Siebers, M Arnfield, J O Kim, and R Mohan. Monte carlo dose calculations for dynamic IMRT treatments. *Phys. Med. Biol.*, 46(4):929–941, April 2001.

[61] D W Kim, K Park, H Kim, and J Kim. History of the photon beam dose calculation algorithm in radiation treatment planning system. *Prog. Med. Phys.*, 31(3):54–62, September 2020.

[62] G F Knoll. *Radiation detection and measurement*. John Wiley & Sons, 2010.

[63] A D Koulouklidis, S Cohen, and J Kalef-Ezra. Thermochromic phase-transitions of GafChromic films studied by z-scan and temperature-dependent absorbance measurements. *Med. Phys.*, 40(11):112701, November 2013.

[64] W Lechner, R Alfonso, M Arib, M S Huq, A Ismail, R Kinhikar, J M Lárraga-Gutiérrez, K R Mani, N Maphumulo, O A Sauer, S Shoeir, S Suriyapee, and K Christaki. A multi-institutional evaluation of small field output factor determination following the recommendations of IAEA/AAPM TRS-483. *Med. Phys.*, 49(8):5537–5550, August 2022.

[65] E E Lewis and W F Miller. Computational methods of neutron transport. 1984.

[66] D A Low, W B Harms, S Mutic, and J A Purdy. A technique for the quantitative evaluation of dose distributions. *Med. Phys.*, 25(5):656–661, May 1998.

[67] C Ma, M Chen, T Long, D Parsons, X Gu, S Jiang, Q Hou, and W Lu. Flattening filter free in intensity-modulated radiotherapy (imrt)–theoretical modeling with delivery efficiency analysis. *Medical physics*, 46(1):34–44, 2019.

[68] A Mack, G Mack, D Weltz, S G Scheib, H D Böttcher, and V Seifert. High precision film dosimetry with GAFCHROMIC films for quality assurance especially when using small fields. *Med. Phys.*, 30(9):2399–2409, September 2003.

[69] T R Mackie, A F Bielajew, D W Rogers, and J J Battista. Generation of photon energy deposition kernels using the EGS monte carlo code. *Phys. Med. Biol.*, 33(1):1–20, January 1988.

[70] G Mamballikalam, S Senthilkumar, B P M Ahamed, R Inipully, P M Jayadevan, C O Clinto, and B R C Jaon. Point dose verification of cranial stereotactic radiosurgery using micro ionization chamber and EBT3 film for 6MV FF and FFF beams in varian TrueBeam LINAC. *Pol. J. Med. Phys. Eng.*, 26(3):135–142, September 2020.

[71] G Marsaglia, B Narasimhan, and A Zaman. A random number generator for pc's. *Computer Physics Communications*, 60(3):345–349, 1990.

[72] G Marsaglia, A Zaman, and W W Tsang. Toward a universal random number generator. *Statistics & Probability Letters*, 9(1):35–39, 1990.

[73] De Martino, F Clemente, S Graeff, C Palma, and G Cella. Dose calculation algorithms for external radiation therapy: An overview for practitioners. *Applied Sciences*, 11(15), 2021.

[74] L Masi, R Doro, V Favuzza, S Cipressi, and L Livi. Impact of plan parameters on the dosimetric accuracy of volumetric modulated arc therapy. *Med. Phys.*, 40(7):071718, July 2013.

[75] S L Meeks, C E Mercado, R A Popple, N Agazaryan, T Kaprealian, J B Fiveash, and S Tenn. Practical considerations for single isocenter linac radiosurgery of multiple brain metastases. *Practical Radiation Oncology*, 12(3):195–199, 2022.

[76] Y Miao, A Ifthaker, R Fullarton, E Almond, G Kidane, L Crees, D Withers, and H Barking. Evaluation of srs mapcheck™ for sabr patient-specific qa. 2020.

[77] R Mohan, C Chui, and L Lidofsky. Differential pencil beam dose computation model for photons. *Med. Phys.*, 13(1):64–73, January 1986.

[78] W R Nelson, H Hirayama, and D W Rogers. *EGS4 code system (No. SLAC-265). Stanford Linear Accelerator Center.* Menlo Park, CA (USA), 1985.

[79] C Nieder, A L Grosu, and L E Gaspar. Stereotactic radiosurgery (SRS) for brain metastases: a systematic review. *Radiat. Oncol.*, 9(1):155, July 2014.

[80] A Niroomand-Rad, S T Chiu-Tsao, M P Grams, D F Lewis, C G Soares, L J Van Battum, and Chan. Report of AAPM task group 235 radiochromic film dosimetry: an update to TG-55. medical physics. 47:5986–6025, 2020.

[81] U Oelkfe and C Scholz. Dose calculation algorithms. In *New Technologies in Radiation Oncology*, pages 187–196. Springer-Verlag, Berlin/Heidelberg, 2006.

[82] S Olver and A Townsend. Fast inverse transform sampling in one and two dimensions. July 2013.

[83] H Palmans, P Andreo, M S Huq, J Seuntjens, K E Christaki, and A Meghzifene. Dosimetry of small static fields used in external photon beam radiotherapy: Summary of TRS-483, the IAEA-AAPM international code of practice for reference and relative dose determination. *Med. Phys.*, 45(11):e1123–e1145, November 2018.

[84] D Parsons, C Ding, B Zhao, T Chiu, L Tirpak, R Reynolds, and Gu. Characterization and validation of SRS MapCheck for patient specific QA on CyberKnife M6. In *Presentation Presented at AAPM 61st Annual Meeting*, pages 14–18. San Antonio, TX, 2019.

[85] E B Podgorsak. *Radiation oncology physics: a handbook for teachers and students*. IAE Agency, Vienna, Austria, 2005.

[86] E B Podgoršak. Radioactivity. *Radiation Physics for Medical Physicists*, pages 262–358, 2006.

[87] E Poon, B Reniers, S Devic, T Vuong, and F Verhaegen. Dosimetric characterization of a novel intracavitary mold applicator for high dose rate endorectal brachytherapy treatment. *Medical physics*, 33(12):4515–4526, 2006.

[88] M S Rose, L Tirpak, K Van Casteren, J Zack, T Simon, A Schoenfeld, and W Simon. Multi-institution validation of a new high spatial resolution diode array for srs and sbrt plan pretreatment quality assurance. *Medical Physics*, 47(7):3153–3164, 2020.

[89] B M Sadowski, M Fillmann, D Szałkowski, and P Kukołowicz. Evaluation of SRS MapCHECK with StereoPHAN phantom as a new pre-treatment system verification for SBRT plans. *Pol. J. Med. Phys. Eng.*, 28(2):84–89, June 2022.

[90] I Schoepper, S Dieterich, E A Trestrail, and M S Kent. Pre-clinical and clinical evaluation of the HYPERSCINT plastic scintillation dosimetry research platform for in vivo dosimetry during radiotherapy. *J. Appl. Clin. Med. Phys.*, 23(4):e13551, April 2022.

[91] A J D Scott, S Kumar, A E Nahum, and J D Fenwick. Characterizing the influence of detector density on dosimeter response in non-equilibrium small photon fields. *Phys. Med. Biol.*, 57(14):4461–4476, July 2012.

[92] J V Siebers, P J Keall, J O Kim, and R Mohan. A method for photon beam monte carlo multileaf collimator particle transport. *Phys. Med. Biol.*, 47(17):3225–3249, September 2002.

[93] Canadian Cancer Society. Cancer statistics at a glance. `https://cancer.ca/en/research/cancer-statistics/cancer-statistics-at-a-glance`.

[94] T D Solberg, J M Balter, S H Benedict, B A Fraass, B Kavanagh, C Miyamoto, T Pawlicki, L Potters, and Y Yamada. Quality and safety considerations in stereotactic radiosurgery and stereotactic body radiation therapy: Executive summary. *Pract. Radiat. Oncol.*, 2(1):2–9, January 2012.

[95] James A Tanyi, Paige A Summers, Charles L McCracken, Yiyi Chen, Li-Chung Ku, and Martin Fuss. Implications of a high-definition multileaf collimator (hd-mlc) on treatment planning techniques for stereotactic body radiation therapy (sbrt): a planning study. *Radiation Oncology*, 4(1):1–7, 2009.

[96] M L Taylor, T Kron, and R D Franich. A contemporary review of stereotactic radiotherapy: inherent dosimetric complexities and the potential for detriment. *Acta Oncol.*, 50(4):483–508, May 2011.

[97] F Therriault-Proulx, L Archambault, L Beaulieu, and S Beddar. Development of a novel multi-point plastic scintillation detector with a single optical transmission line for radiation dose measurement. *Phys. Med. Biol.*, 57(21):7147–7159, November 2012.

[98] L Tillikainen, H Helminen, T Torsti, S Siljamäki, J Alakuijala, J Pyyry, and W Ulmer. A 3D pencil-beam-based superposition algorithm for photon dose calculation in heterogeneous media. *Phys. Med. Biol.*, 53(14):3821–3839, July 2008.

[99] R Townson, H Egglestone, and S Zavgorodni. A fast jaw-tracking model for VMAT and IMRT monte carlo simulations. *J. Appl. Clin. Med. Phys.*, 19(4):26–34, July 2018.

[100] James E Turner. *Atoms, radiation, and radiation protection.* John Wiley & Sons, 2008.

[101] W Ulmer, J Pyyry, and W Kaissl. A 3D photon superposition/convolution algorithm and its foundation on results of monte carlo calculations. *Phys. Med. Biol.*, 50(8):1767–1790, April 2005.

[102] J Van Dyk, R B Barnett, J E Cygler, and P C Shragge. 'commissioning and quality assurance of treatment planning computers,". *Int. J. Radiat. Oncol., Biol., Phys*, 26:261–273.

[103] A Van Esch, L Tillikainen, J Pyykkonen, M Tenhunen, H Helminen, S Siljamäki, J Alakuijala, M Paiusco, M Iori, and D P Huyskens. Testing of the analytical anisotropic algorithm for photon dose calculation. *Medical physics*, 33(11):4130–4148, 2006.

[104] O N Vassiliev, T A Wareing, J McGhee, G Failla, M R Salehpour, and F Mourtada. Validation of a new grid-based boltzmann equation solver for dose calculation in radiotherapy with photon beams. *Phys. Med. Biol.*, 55(3):581–598, February 2010.

[105] F Verhaegen and J Seuntjens. Monte carlo modelling of external radiotherapy photon beams. *Physics in medicine & biology*, 48(21):R107, 2003.

[106] P Wang, J B Li, L Zhou, and D Y Liu. Acceptance-rejection sampling based monte carlo ray tracing in anisotropic porous media. *Energy (Oxf.)*, 199(117455):117455, May 2020.

[107] T A Wareing, J M McGhee, J E Morel, and S D Pautz. Discontinuous finite element sn methods on three-dimensional unstructured grids. *Nuclear science and engineering*, 138(3):256–268, 2001.

[108] S Webb. Use of a quantitative index of beam modulation to characterize dose conformity: illustration by a comparison of full beamlet IMRT, few-segment IMRT (fsIMRT) and conformal unmodulated radiotherapy. *Phys Med Biol*, 48:2051–2062, 2003.

[109] S Weinzierl. Introduction to monte carlo methods. June 2000.

[110] N Wen, S Lu, J Kim, Y Qin, Y Huang, B Zhao, C Liu, and I J Chetty. Precise film dosimetry for stereotactic radiosurgery and stereotactic body radiotherapy quality assurance using gafchromic™ EBT3 films. *Radiat. Oncol.*, 11(1):132, October 2016.

[111] M Westermark, J Arndt, B Nilsson, and A Brahme. Comparative dosimetry in narrow high-energy photon beams. *Phys. Med. Biol.*, 45(3):685–702, March 2000.

[112] L Wootton and S Beddar. Temperature dependence of bcf plastic scintillation detectors. *Physics in Medicine & Biology*, 58(9):2955, 2013.

[113] J U Würfel. Dose measurements in small fields. *Med Phys*, 1(1):81–90, 2013.

[114] K Yasui, Y Saito, S Ogawa, and N and Hayashi. Dosimetric characterization of a new two-dimensional diode detector array used for stereotactic radiosurgery quality assurance. *Int. J. Radiat. Res.*, 19(2):281–289, April 2021.